الجمهورية الجزائرية الديمقراطية الشعبية

وزارة التعليم العالي والبحث العلمي

University SAAD DAHLEB Blida
Institute of Aeronautics and
Space Studies

جامعة سعد دحلب البليدة
معهد الطيران والدراسات الفضائية

In partial fulfilment of the requirements for the master degree in aeronautics.
Specialty: Aircraft propulsion

optimization of the clearance between the impeller and the shroud of a centrifugal compressor to achieve better performance

Submitted by:

KHETTAL Kada

SAIDANI Ali

Under the supervision of:

Mr. LAAZAB Sebaa

BLIDA 2023-2024

Acknowledgement

We would like to thank ALLAH, the Almighty, for giving us the courage and willpower to accomplish this modest work.

We would like to express our sincere thanks to our promoter "LAAZAB Sebaa" for their patience, their comments and advice, their availability and kindness.

We would also like to thank the members of the jury who kindly agreed to be present today.

Our thanks also go to all our teachers of the Aircraft Propulsion specialty in our training.

And to all those who have participated in any way in the completion of this work.

Many thanks to all of you

Dedication

We dedicate this modest work to our very dear parents for their encouragement and support and for their patience.

To our brothers and sisters.

To our families: KHETTAL, SAIDANI.

To all our university friends for all the unforgettable moments spent together and for their.

Table of contents

LIST OF FIGURES

LIST OF TABLES

ABSTRACT:

In this thesis, the performance of a centrifugal compressor was analyzed using ANSYS CFX simulation software. The optimization process focused on the distance between the blades and the shroud of the compressor, utilizing ANSYS Design Optimization. The study aimed to investigate how this distance affects compressor performance.

The analysis employed ANSYS CFX 23, based on finite volume techniques, and the optimization followed the Design of Experiment (DOE) methodology. Key parameters studied included the meridional geometry and blade tip clearance; particularly in relation to changes in the aerodynamic characteristics, such as the airflow rate within the compressor.

The analysis using numerical modeling to simulate a three-dimensional, compressible, viscous, and turbulent steady-state flow in the impeller of the centrifugal compressor using the k-ω SST model.

The results indicated that multi-objective optimization of the blade tip properties significantly impacted compressor performance. The application of ANSYS CFX and ANSYS Design Optimization facilitated a more efficient and precise analysis, allowing for the determination of the optimal blade tip clearance. This optimization improved the overall compressor performance specifying pressor ratio and efficiency, as confirmed by studying the performance at the optimized blade tip distance.

Keywords: Optimization, compressor, Tip clearance, ANSYS, CFX, blade.

ملخص:

في هذه الأطروحة، تم تحليل أداء ضاغط الطرد المركزي باستخدام برنامج المحاكاة ANSYS CFX. وركزت عملية التحسين على المسافة بين الشفرات وغطاء الضاغط، باستخدام برنامج ANSYS لتحسين التصميم. هدفت الدراسة إلى التحقق من كيفية تأثير هذه المسافة على أداء الضاغط.

استخدم التحليل برنامج ANSYS CFX 23، استنادًا إلى تقنيات الحجم المحدود، واتبعت عملية التحسين منهجية تصميم التجربة. وشملت المعلمات الرئيسية التي تمت دراستها هندسة الزوال وخلوص طرف الشفرة؛ خاصةً فيما يتعلق بالتغيرات في الخصائص الديناميكية الهوائية، مثل معدل تدفق الهواء داخل الضاغط.

التحليل باستخدام النمذجة العددية لمحاكاة تدفق ثلاثي الأبعاد، ثلاثي الأبعاد، قابل للانضغاط، لزج ومضطرب في حالة مستقرة في المكره لضاغط الطرد المركزي باستخدام نموذج SST k-ω.

أشارت النتائج إلى أن التحسين متعدد الأهداف لخصائص طرف الشفرة أثر بشكل كبير على أداء الضاغط. سهّل تطبيق ANSYS CFX وAnSYS Design Optimization تحليلًا أكثر كفاءة ودقة، مما سمح بتحديد الخلوص الأمثل لطرف الشفرة. وقد أدى هذا التحسين إلى تحسين الأداء الكلي للضاغط الذي يحدد نسبة الضاغط وكفاءته، كما تم تأكيد ذلك من خلال دراسة الأداء عند المسافة المثلى لطرف الشفرة.

الكلمات المفتاحية: التحسين الأمثل، الضاغط، البعد الطرفي، ANSYS، CFX، الشفرة.

Résumé :

Dans cette thèse, les performances d'un compresseur centrifuge ont été analysées à l'aide du logiciel de simulation ANSYS CFX. Le processus d'optimisation s'est concentré sur la distance entre les aubes et l'enveloppe du compresseur, en utilisant ANSYS Design Optimisation. L'étude visait à déterminer comment cette distance affecte les performances du compresseur.

L'analyse a utilisé ANSYS CFX 23, basée sur des techniques de volumes finis, et l'optimisation a suivi la méthodologie des plans d'expérience (DOE). Les paramètres clés étudiés comprenaient la géométrie méridienne et le jeu en bout d'aube, en particulier en relation avec les changements dans les caractéristiques aérodynamiques, telles que le débit d'air à l'intérieur du compresseur.

L'analyse utilise la modélisation numérique pour simuler un écoulement tridimensionnel, compressible, visqueux et turbulent en régime permanent dans la roue du compresseur centrifuge en utilisant le modèle k-ω SST.

Les résultats ont montré que l'optimisation multi-objective des propriétés de l'extrémité des aubes avait un impact significatif sur les performances du compresseur. L'application d'ANSYS CFX et d'ANSYS Design Optimisation a facilité une analyse plus efficace et plus précise, permettant de déterminer le jeu optimal de l'extrémité des aubes. Cette optimisation a permis d'améliorer les performances globales du compresseur en spécifiant le rapport de pression et l'efficacité, comme le confirme l'étude des performances à la distance optimisée de l'extrémité de l'aube.

Mots-clés: Optimisation, compresseur, jeu, ANSYS, CFX, aube.

INTRODUCTION

The optimization of centrifugal compressor end clearance using ANSYS CFX, TurboGrid, and Design Optimization is a significant focus due to the widespread industrial use of centrifugal compressors, which are valued for their simple design, robustness, and efficiency. Minimizing the clearance between the impeller blades and the shroud is essential for optimizing compressor performance, as excessive end clearance can result in reduced efficiency, increased vibration, and operational instabilities. This thesis aims to optimize the end clearance of a centrifugal compressor impeller through numerical simulation tools. ANSYS CFX was utilized as the Computational Fluid Dynamics (CFD) solver to model the compressor, while TurboGrid was employed to generate the computational mesh, and Design Optimization served as the optimization framework. The workflow began with generating the impeller geometry using TurboGrid, followed by meshing the geometry to produce a computational mesh. ANSYS CFX then simulated the compressor's performance at various blade tip clearances, and the results were passed to Design Optimization. This framework iteratively ran CFX simulations to maximize the pressure ratio by optimizing the tip clearance. The optimization results revealed that adjusting the tip clearance from an initial value of 0 mm to 0.7 mm for leading edge and trailing edge variable significantly increased the compressor's pressure ratio. Further analysis of the flow field indicated that reducing the end clearance minimized leakage rates and improved impeller performance.

BIBLIOGRAPHIC ANALYSIS

The flow within a centrifugal compressor is generally viscous, turbulent, three-dimensional, unsteady, and compressible. To study and analyze this flow, two methods can be employed: numerical and experimental.

The numerical method involves discretizing the fundamental fluid mechanics equations to solve the problem computationally. On the other hand, the experimental method requires various measurement systems (for pressure, velocity, temperature, etc.) and visualization techniques to analyze different flow structures.

Numerous researchers have already conducted studies on optimizing and analyzing the flow within a centrifugal compressor.

Carsten WeiB et al., 2003 [1]

Studied the impact of no uniform tip clearance profiles on the performance and flow field of a centrifugal compressor with a vaneless diffuser. Six impellers with varying tip clearance profiles were analyzed through numerical simulations. The study focused on assessing the magnitude and location of the wake. Results showed that while overall performance improved with reduced tip clearances, the most significant enhancement occurred when the tip clearance was minimized at the trailing edge rather than the leading edge. This configuration led to a more uniform velocity distribution at the impeller exit, aiding diffusion processes within the vaneless diffuser. The accuracy of the numerical simulations was validated by comparing computational results with experimental data from systems featuring original tip clearances.

Yohan Jung et al., 2012 [2]

This paper investigates the impact of non uniform tip clearance profiles on a centrifugal compressor's performance and flow field, with a focus on wake characteristics. Six impellers with varying tip clearance profiles undergo flow simulations, and the accuracy of the numerical simulations is validated with experimental data. Results indicate that while performance generally improves with lower tip clearances, particularly at the trailing edge, this improvement is more significant than at the leading edge. Impellers with reduced tip clearance at the trailing edge produce a more uniform velocity distribution at the impeller exit, enhancing potential diffusion processes inside the vaneless diffuser.

Matteo Bardelli et al., 2019 [3]

This study uses Computational Fluid Dynamics (CFD) to investigate how the impeller and vaned diffuser interact in a centrifugal compressor. By using experimental data, the research validates the simulation method and discusses its findings. Various CFD models, from simple to complex, are developed to study different aspects of this interaction. Initial steady-state analysis gives an overview of flow behavior and the strengths and weaknesses of the models. An additional unsteady analysis explores the interaction further, examining two operating points. The results align well with experimental data, providing valuable insights into the flow dynamics.

Xinzi Tang et al., 2021 [4]

Optimization the aerodynamic robustness of centrifugal compressor impellers amidst multiple uncertainties. It introduces an efficient optimization procedure and delves into the underlying mechanisms, proposing a novel method for multi-objective optimization and design exploration. Through a neural-network-based Kriging model and self-organizing mapping, correlations between design variables and performance parameters are revealed and visualized. Results demonstrate significant improvements in impeller performance metrics, with notable increases in pressure ratio and efficiency, reduced standard deviations, and decreased acoustic power levels. The approach offers enhanced accuracy in uncertain approximation modeling and facilitates efficient design optimizations, supporting exploration across various turbomachinery applications.

Xiaojian Li et al., 2022 [5]

This study implements coupling optimization to redesign a transonic centrifugal compressor with Self-recirculation casing treatment (SRCT). Firstly, the design space is expanded to include SRCT and impeller/diffuser parameters. Data-mining techniques refine this space, identifying seven critical design parameters with non-linear correlations. Global optimization yields significant aerodynamic performance improvements, eliminating SRCT's efficiency penalty while maintaining stability. Flow mechanisms include increased recirculation flow rate in SRCT, reduced incidence angle and blade loading in impeller, and delayed interaction between tip leakage vortex and inducer shock wave. Additionally, inlet mixing loss and radial distortion decrease, friction loss reduces, and flow separation in the vaned diffuser is suppressed.

Lianchao Xu et el., 2023 [6]

This study employs unsteady full annular simulations to investigate flow instability in a centrifugal compressor, focusing on instabilities occurring primarily in the impeller. Perturbations in the impeller are classified into impeller-diffuser interactions, self-excited perturbations, and vortex-induced perturbations. Modes induced by impeller-diffuser interactions and self-excited perturbations reflect inherent flow unsteadiness in the impeller. Vortex-induced perturbations couple with self-excited ones, affecting spatial structures of modes induced by self-excited perturbations, especially during reduced mass flow rates where resonance effects may occur. During rotating stall process (RSP), characteristic modes such as the 4 RF (rotor frequency) mode grow, typical of rotating stall in the impeller. Additionally, vortex-induced perturbations exhibit variant characteristics with mass flow rate, and the growth of low-frequency characteristic modes is another typical feature of rotating stall in the impeller during RSP.

CHAPTER 1: GENERAL INFORMATION ON CENTRIFUGAL COMPRESSORS

1.1. Generality of turbomachinery

1.1.1. INTRODUCTION

The transfer of fluid energy to a rotating wheel on which blades are mounted, and vice versa, has given rise to a special class of machines known as 'turbomachinery'.

Turbomachines play a pivotal role in various industries, ranging from aerospace and automotive to energy production and manufacturing. These mechanical devices harness the power of fluid flow to perform tasks such as generating propulsion, compressing gases, or producing electricity. The efficiency and performance of turbomachines are crucial for achieving desired outcomes in these applications, making their design and optimization a subject of continuous research and development.

1.1.2. Turbomachine

A turbomachine is a mechanical device that transfers energy between a rotor and a fluid, typically air or a gas. It opérâtes on the principle of converting the kinetic energy of the fluid into mechanical work or vice versa. Turbomachines are commonly used in various engineering applications, including power generation, propulsion systems (such as aircraft engines and gas turbines), pumps, compressors, and fans. They are essential for fluid flow control and energy conversion in numerous industrial and transportation processes.

1.1.3. General Classification of Turbomachines

There is an enormous variety of turbomachinery, and they are classified according to diverse criteria [7]:

1.1.3.1. By their functions:

- Work-absorbing turbomachines: such as compressors and fans
- Work-producing turbomachines: generally known as turbines

1.1.3.2. By the nature of the working medium:

- Compressible-flow turbomachines: where the incoming fluid is totally air, as in fans and compressors, or the products of combustion, as in gas turbines. In The latter category, and in the absence of an afterburner, the working medium will still be treated as predominantly air.

- Incompressible-flow turbomachines: where the working medium may be water (hydraulic pumps) or any single-phase substance in the liquid form.

1.1.3.3. By the type of meridional flow path:

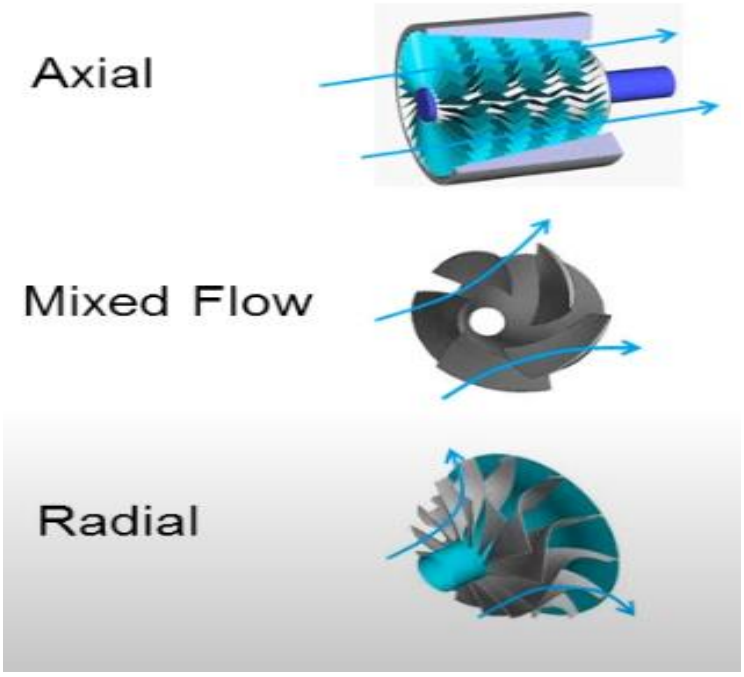

Figure 1.1: Types of meridional flow path

- Radial (centrifugal) machines:

The meridional flow path is perpendicular to the rotation axis. The flow enters the turbomachine radially, that is, perpendicular to the rotation axis, and exits axially, that is, parallel to the rotation axis.

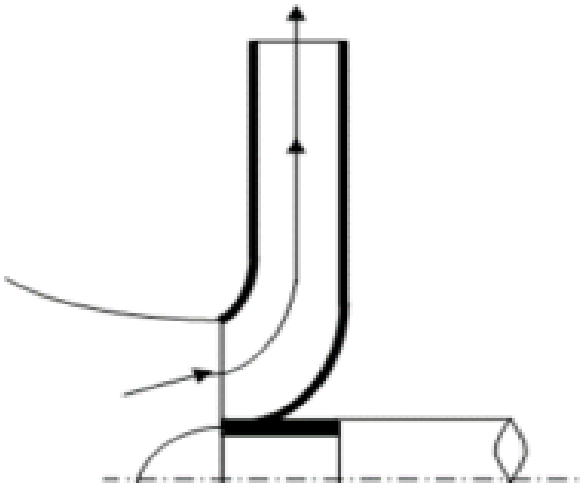

Figure 1.2: Radial drive Wheel

- Axial machines:

The meridional flow path is parallel to the rotation axis. The flow enters and exits the turbomachine in the same direction, parallel to the rotation axis.

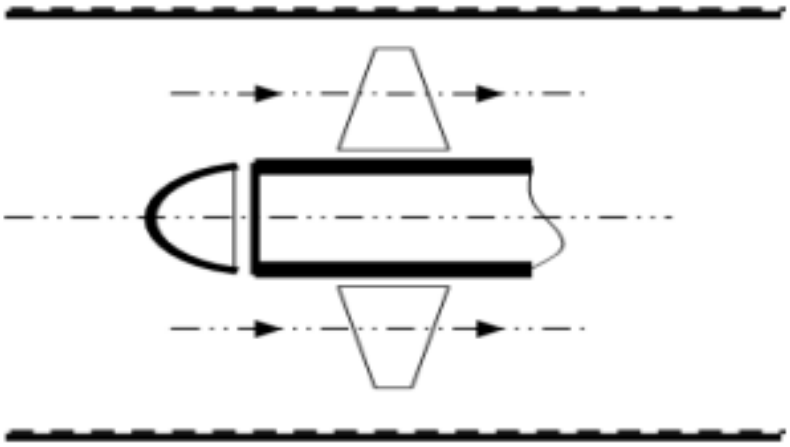

Figure 1.3: axial drive wheel

- Centrifugal or helical machines:

The meridional flow path is a combination of radial and axial flow.The flow enters the turbomachine at an angle to the rotation axis, and exits at a different angle.

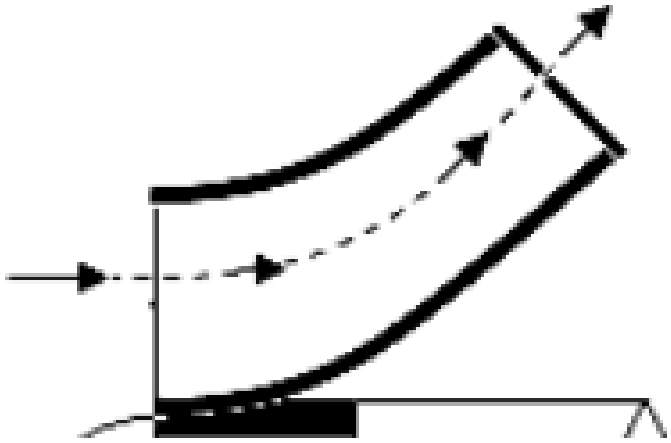

Figure 1.4: helical drive wheel

1.1.4. Constitution of Turbomachinery:

A turbomachine is essentially constituted of: the rotor, stator, and shaft.

- The rotor is the rotating element that carries rotor blades or vanes, responsible for transferring energy between the flowing fluid and the rotating element.
- The stator is a stationary element that carries guide vanes or stator blades, controlling the direction of fluid flow during the energy conversion process.

- ❖ The shaft transmits power into or out of the machine, depending on whether it is a power-generating or power-absorbing machine.

These components work together to facilitate the dynamic transfer of energy between a flowing fluid and a rotating element, resulting in changes in pressure and momentum within the fluid.

1.1.5. Advantages and inconvenient:

Although turbomachines offer significant advantages and find application in various sophisticated industries, they are not immune to challenges. The current energy market liberalization context necessitates their operation under partial load conditions, which were not initially considered during their design. In addition to corrosion issues, internal factors related to fluid behavior through the blades emerge. These factors result in pressure and velocity fluctuations, cavitation, and subsequent high mechanical stresses, leading to premature material fatigue, crack formation, and reduced operational lifespan of the machine.

1.2. Centrifugal compressor

Centrifugal compressors, known for their efficiency and capacity to produce large volumes of air in compact units, utilize a rotating element to convert kinetic energy into potential energy in the form of pressure within an airstream. The principle of centrifugal compression involves the air being directed towards the center of the impeller, then propelled outward by centrifugal force, before gradually diffusing to reduce velocity and increase pressure.

These compressors excel in applications requiring over 200 total horsepower, particularly suited for high capacities due to their continuous flow through multiple stages. Unlike reciprocating compressors, they boast fewer moving parts, resulting in reduced maintenance and downtime. Their straightforward design and sturdy construction further contribute to their extended service life.

1.2.1. The objective of Compression:

Compression typically arises from the necessity to transfer a specific volume of gas from one system operating at a particular pressure to another system requiring a higher pressure level. The primary aim of this process is to:

- Establish a continuous gas flow within an enclosed loop.
- Transport gas through a pipeline from the production site to the end user.
- Generate compressed air essential for facilitating gas combustion recovery.

1.2.2. Basic components of the centrifugal compressor

1.2.2.1. Inlet:

- The component that takes in the gas or air to be compressed.
- Can be a simple opening or a more complex system involving filters, screens, and anti-icing measures.
- The inlet design affects the pressure, temperature, and flow rate of the gas or air entering the compressor.

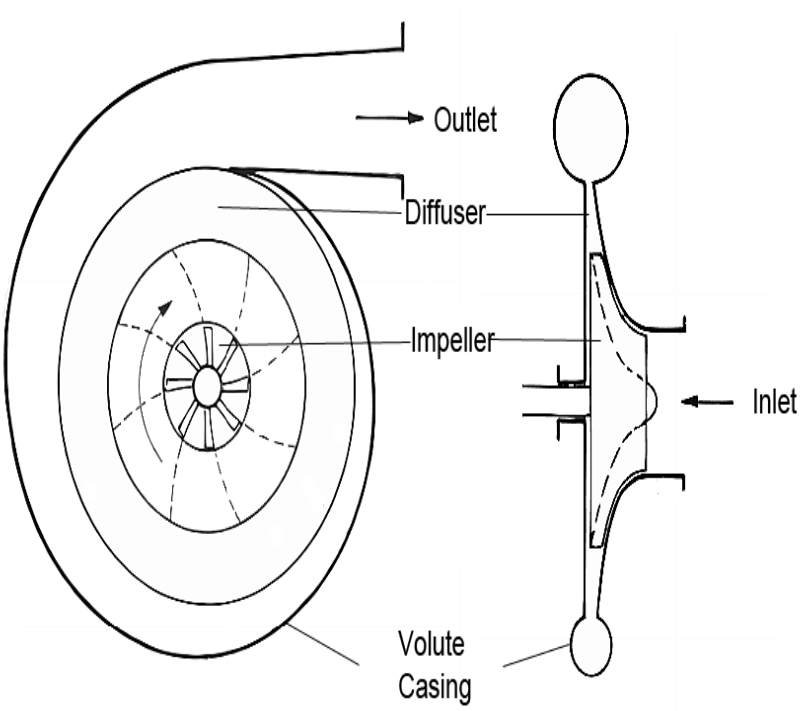

Figure 1.5: components of the centrifugal compressor [8]

1.2.2.2. Impeller:

The rotating component that uses centrifugal force to increase the velocity of the gas or air.

It is typically made of high-strength materials like titanium or stainless steel.

The impeller's shape and size can vary depending on the compressor's intended use and design.

1.2.2.3. Diffuser:

- Responsible for converting the high-velocity gas or air from the impeller into high-pressure gas or air.
- Achieves this by converting the kinetic energy of the gas or air into pressure energy through a series of vanes, channels, and other components.
- The diffuser's design is critical to the compressors overall efficiency and performance.

1.2.2.4. Volute:

The main role of the volute is to collect the radial flow at the diffuser outlet and return it to the system via a tubular duct, by changing the cross-sectional area. The flow in the volute is often modelled (assumption of incompressible fluid) by logarithmic spirals, but part of the fluid performs a complete gyration and is juxtaposed to the main flow at the nozzle (start zone of the spiral).

If the impeller starts to rotate, it gives a flow at the outlet, and the air is then collected by the volute or by a system that changes direction along the axis of rotation in the case of turbojets.

1.2.3. Functioning principle of a centrifugal compressor:

Centrifugal compressors find extensive use across various industrial sectors due to their reliable performance, ability to withstand significant process fluctuations, and overall efficiency compared to alternative compressor types. The gas intake process begins as the compressor draws gas through the suction flange, guiding it into an annular aspiration volute where it uniformly converges towards the center in all radial directions. To prevent gas vortex formation, a fin is positioned within the annular chamber opposite the suction flange.

Subsequently, the gas enters the aspiration diaphragm and is drawn in by the first impeller. This impeller accelerates the gas outward, increasing its velocity and pressure. The gas then proceeds in a spiral motion through a circular diffuser chamber, where its velocity decreases while pressure rises. Following this, the gas passes through the return channel, a circular chamber bounded by two rings forming the intermediate diaphragm with blades that direct the gas towards the next impeller's suction.

The vanes' arrangement straightens the gas's spiral movement, enabling a radial outlet and an axial inlet for the subsequent impeller. This process repeats for each impeller. Labyrinth seals, composed of two or more ring segments, are incorporated into the diaphragm to minimize internal gas leakage. The final impeller directs the gas into a diffuser, leading to a discharge volute, which collects the gas from the diffusers' periphery and guides it to the discharge flange. A vane near the discharge flange prevents gas from returning to the volute, directing it towards the discharge flange.

1.2.4. Characteristic Curves of a Centrifugal Compressor:

The characteristic curves of a centrifugal compressor are typically plotted with the mass flow rate $\dot{m}$ on the x-axis and the compression ratio ($\tau = \frac{P_{ts}}{P_{te}}$) on the y-axis for a specific speed.

1.2.4.1. Performance Presentation:

- The performance is depicted in a flow-pressure field where the compressor's iso-velocity curves, iso-efficiency curves, and operational limits are displayed see figure 1.6.

1.2.4.2. Invariance to Inlet Conditions:

- Using reduced values allows the compressor map to remain unchanged regardless of the fluid inlet conditions, as shown in figure 1.6

Thus, the reduced flow rate value is often reported at standard conditions specific to each manufacturer. Pressure values are presented as compression ratios, with absolute values considered, and the pressures are total pressures. Rotational speeds are also expressed in reduced values.

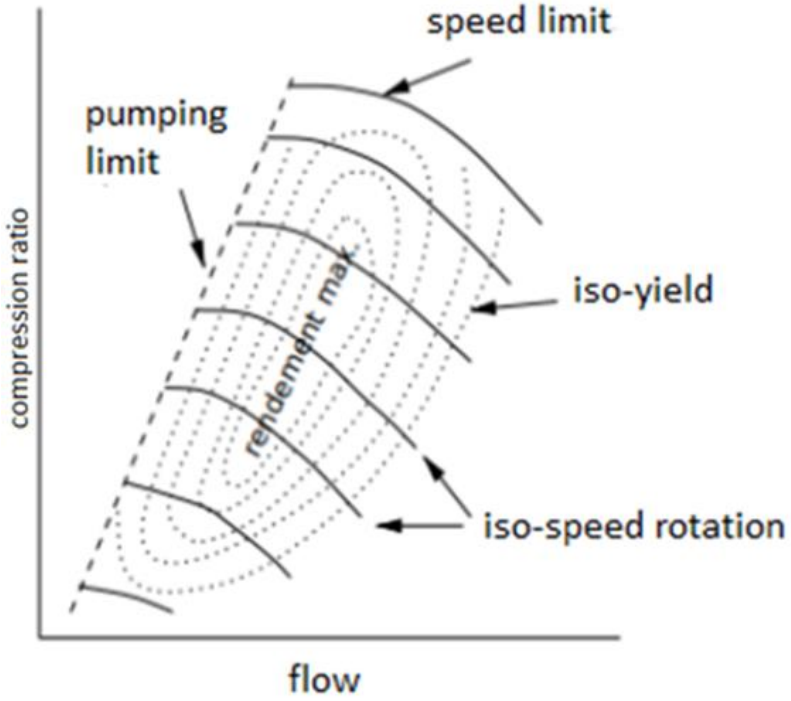

Figure 1.6: Functional characteristics of a centrifugal compressor.

1.2.5. Limit of use for a centrifugal compressor

The compressor links to two networks with distinct pressures: the aspiration (low pressure) and the discharge (high pressure). Pumping in the compressor occurs when the high-pressure discharge network feeds into the low-pressure networks through counter-current flow. This phenomenon, often due to various factors, leads to momentary instability in the air networks, especially when dealing with gas like air.

As the discharge network empties into the aspiration, the compressor temporarily faces operating instability until the flow direction stabilizes again. Such large flow fluctuations cause

pumping, characterized by violent oscillatory flow reversals. Each flow direction change represents a shock to the compressor's mechanical components and the main motor's electrical supply. [9]

Manufacturers incorporate fatigue-resistant elements to mitigate repeated shock-induced damage. Consequences of pumping include compressor blade breakage, intense radial vibrations, motor wear, and burst pipes in the air network. To prevent damage, manufacturers install pumping or flow return sensors, which deactivate the main motor's power supply. However, these sensors react to the problem rather than anticipate it.

At low air flows, the iso-speed curve initially exhibits a negative slope, which transitions to zero and then becomes positive, resulting in acceptable pressure variations during transient operation. However, excessive pressure fluctuations, leading to instability and noisy clacking, indicate pumping and should be avoided. The surge limit, depicted as a surge line on the characteristic curve of a centrifugal compressor, marks the threshold beyond which sonic flow blockage occurs due to high air flow rates.

1.2.6. The advantages and disadvantages of the centrifugal compressor:

The advantages:

- Low weight and easy to design and manufacture.
- High compression ratio for comparison with an axial compressor stage.
- Reliability and low maintenance.
- High-flow rate and higher pressure ratio per stage compared to axial flow compressors.

The disadvantages

- Larger frontal area for a given air flow rate compared to axial flow compressors.
- Unsuitable for very high compression and limited pressure.
- There is a maximum operational speed beyond which the rotor experiences vibrations that exceed acceptable mechanical limits, referred to as "asymmetrical impulses."

1.2.7. The industrial exploitation of centrifugal compressors:

- Power Generation: Centrifugal compressors are used in gas turbine power plants to boost the pressure of natural gas, hydrogen, and nitrogen for efficient power generation.
- At air separation sites (to manufacture gas products).
- Refrigeration or air conditioning equipment.
- Equipment providing compressed air.
- Aircraft pressurization systems (to maintain a safe and comfortable pressure for people).

1.2.8. Flow between the Casing and the Blade (Clearance)

The clearance refers to the very small gap between the tip of a rotating blade and the casing. The flow within this gap is highly unsteady and is influenced by several factors, including blade shape, load distribution, the pressure differential between the pressure side and the suction side of each blade, and the roughness of the walls (surface condition). In this region, the following phenomena may occur:

- Leakage flow at the casing, driven by the pressure difference, generates a vortex.
- Additionally, a layer of vorticity is formed in the direction of the leakage flow. This vorticity encounters a discontinuity, leading to the formation of a clearance vortex when it interacts with the main flow.

1.2.9. Reference planes in a centrifugal compressor

In a centrifugal compressor, several key reference planes are commonly used to analyze the flow and design the components:

1.2.9.1. Meridional Plane

The meridional plane is a cross-sectional plane that passes through the axis of rotation of the compressor. It is perpendicular to the impeller blades and shows the flow path from the inlet to the outlet of the impeller. The meridional contour, including the hub and shroud profiles, is a key design parameter that significantly influences the aerodynamic performance of the compressor.

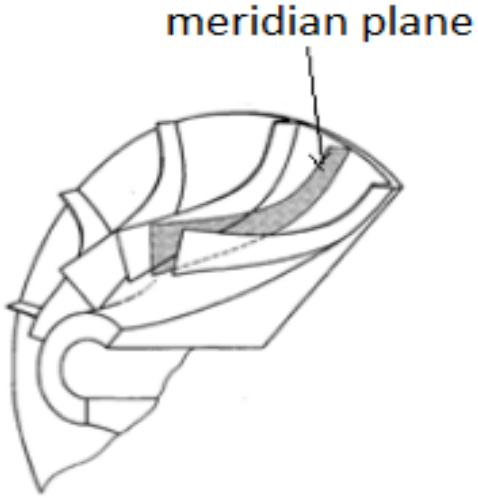

Figure 1.7: Meridional Plane

1.2.9.2. Blade-to-Blade plane

The blade-to-blade plane is a surface that is perpendicular to both the meridional plane and the impeller blades. It shows the flow path between adjacent blades and is used to analyze the blade loading and flow characteristics on the blade surfaces.

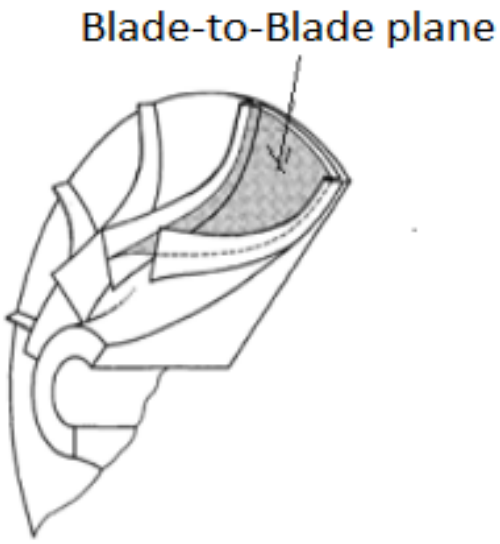

Figure 1.8: Blade-to-Blade plane

1.2.9.3. Orthogonal plane

Orthogonal plane are arbitrary straight lines from hub to shroud in the meridional plane that are used to solve the velocity gradient equations. They remain fixed regardless of streamline changes. This allows the flow distribution in the meridional plane to be calculated using numerical techniques.

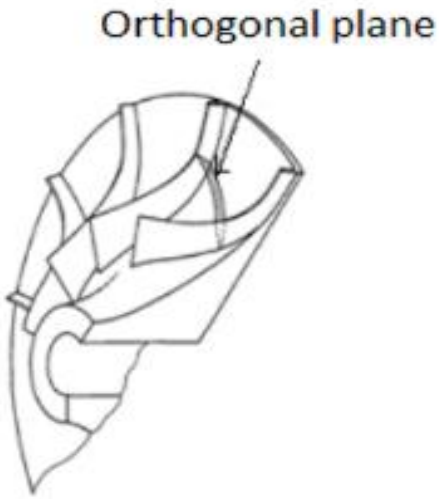

Figure 1.9: Orthogonal plane

1.2.10. Jet and Wake Flow

Centrifugal compressors were initially designed assuming no flow separations and axisymmetric impeller discharge flow. However, Dean and Senoo's 1960 study disproved this by identifying "jet-wake flow," characterized by high velocity on the impeller blade's pressure

side and low velocity on the suction side. This simplified model improved loss prediction over previous uniform exit flow assumptions.

Advancements in measurement technologies have since refined the understanding of impeller flow fields. Eckardt's 1970s research detailed the jet-wake structure, noting non-axisymmetric flow and steep velocity gradients. Subsequent studies, such as Krain's in 1981, confirmed the jet-wake pattern across different geometries with minimal variations.

The jet-wake structure's specifics, like size and location, depend on factors such as shroud curvature and blade exit angle, consistently resulting in large velocity gradients. Additional phenomena like vortices, shocks, and tip leakage flow add to the complexity, complicating accurate performance predictions for centrifugal compressors.

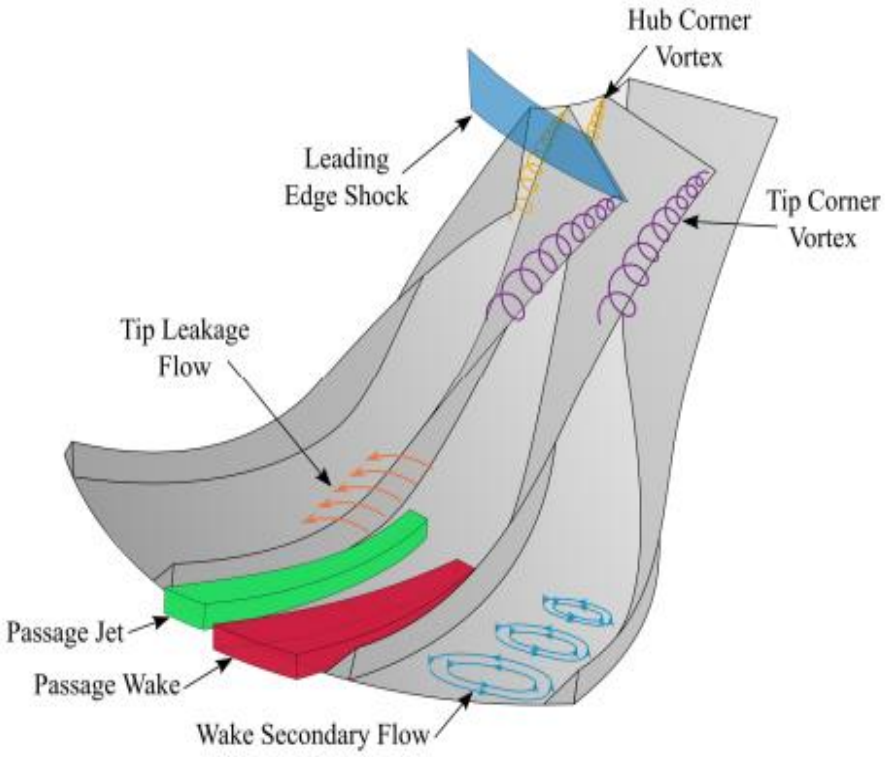

Figure 1.10: Various flow processes commonly developed within centrifugal compressor impellers.[10]

CHAPTER 2: MATHEMATICAL MODEL

2.1. Introduction

Fluid mechanics problems are governed by three-dimensional differential equations, namely the Navier-Stokes equations, which are central to the aerodynamic approach. These equations are essential for accurately describing the motion of fluids. However, solving these equations typically demands substantial computational resources. In some cases, these equations can be simplified to a one-dimensional form using an analytical approach, which involves numerous assumptions and simplifications, such as ignoring turbulence and other complex processes. This chapter will cover one-dimensional analytical equations first, then explore three-dimensional differential equations, and finally delve into turbulence modeling.

2.2. The basic equations

The starting system of equations is based on the principles of conservation of mass, momentum, and energy, forming the Navier-Stokes equations. Generally, for an unsteady, compressible Newtonian fluid, the conservation equations are written as follows:

The continuity equation: this equation expresses the conservation of mass:

$$\frac{\partial \rho}{\partial t} + \frac{\partial (\rho . u_i)}{\partial} = 0 \tag{2.1}$$

The equation for conservation of momentum:

$$\frac{\partial (\rho . u_i)}{\partial t} \frac{\partial (\rho . u_i . u_j)}{\partial t} = -\frac{\partial \rho}{\partial x_i} + \frac{\partial t_{ij}}{\partial x_j} + s_i \tag{2.2}$$

S_i : Source term for all the forces of volume (gravity, centrifugal forces, Coriolis force).

$$S_i = S_{i,cor} + S_{i,cent} = -2.\varepsilon_{ijk}.\rho.\omega_j.u_k - \varepsilon_{klm}.\rho.\omega_j.\omega_l.r_m \tag{2.3}$$

t_{ij} : The viscous stress tensor is expressed by the following equation:

$$t_{ij=}\delta_{ij}.\lambda.\frac{\partial u_k}{\partial x_k}+u.\left(\frac{\partial u_i}{\partial x_j}+\frac{\partial u_j}{\partial x_i}\right)=\delta_{ij}.\lambda.\frac{\partial u_k}{\partial x_k}+2.\mu.\delta_{ij} \quad (2.4)$$

δ_{ij} : is the Kronecker symbol.

The energy equation:

$$\frac{\partial(\rho.h_t)}{\partial t}\frac{\partial(\rho.h_t.u_j)}{\partial x_j}=\frac{\partial\rho}{\partial t}+\frac{\partial}{\partial x_j}.\left(K.\frac{\partial T}{\partial x_J}\right)+\frac{\partial}{\partial x_J}\left(t_{ij}.u_j\right)+S_E \quad (2.5)$$

h_t : Total energy

S_E : Energy source term.

μ : Molecular viscosity depends on temperature.

2.3. Modelling turbulent flows

Turbulence is a property of the flow and is independent of the nature of the fluid. In turbulent flow, macroscopic physical quantities such as temperature, velocity, and pressure fluctuate rapidly and randomly in space and time. Turbulence is characterized by high diffusivity of temperature and momentum.

To solve the equations for flows with high Reynolds numbers, there are three main methods for simulating turbulent flows:

- DNS: Direct Numerical Simulation.
- LES: Large Eddy Simulation.
- RANS: Reynolds-Averaged Navier-Stokes.

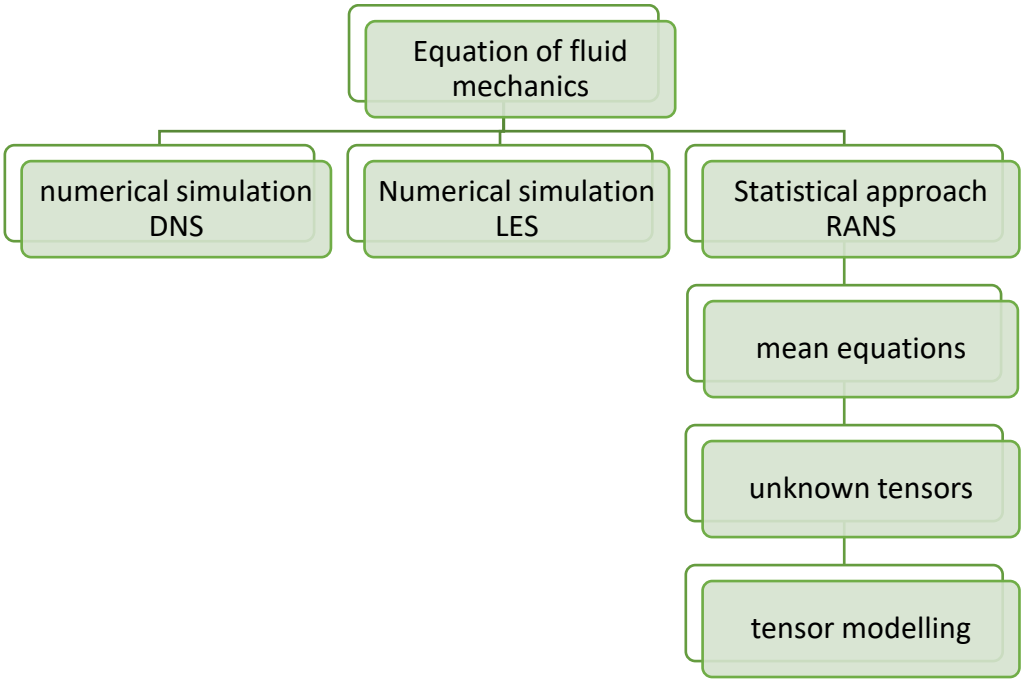

Figure 2.1: Diagram of different numerical methods in ANSYS CFX.

D.N.S (Direct Numerical Simulation):

Direct Numerical Simulation (DNS) is a method where the Navier-Stokes equations are solved directly without any turbulence modeling. This involves capturing all scales of turbulence from the largest to the smallest, requiring:

- Equations: Solves the full, unsteady, three-dimensional Navier-Stokes equations.
- Mesh Resolution: Extremely fine mesh is needed to resolve the smallest turbulent eddies, according to the Kolmogorov scale.
- Computational Demand: Very high computational cost due to the need for fine spatial and temporal resolution.
- Accuracy: Most accurate method as it does not rely on any modeling approximations.
- Applications: Mostly used for fundamental turbulence research and in small-scale problems where computational resources are available.

LES (Large Eddy Simulation)

Large Eddy Simulation (LES) is a technique where the largest turbulent scales are resolved directly, and only the smaller scales are modeled. It balances between the high accuracy of DNS and the reduced computational cost by:

- Equations: Solves the filtered Navier-Stokes equations, where the filter size is typically on the order of the grid size.

- Mesh Resolution: Requires a fine mesh, but not as fine as DNS, especially in regions with high turbulence.
- Subgrid-Scale Model: Uses a subgrid-scale model to account for the effects of the smaller, unresolved scales of turbulence.
- Computational Demand: Lower than DNS but still significantly higher than RANS.
- Accuracy: More accurate than RANS for capturing large-scale turbulent structures.
- Applications: Engineering applications like aerospace, automotive, and meteorology, where capturing large-scale flow features is crucial.

RANS (Reynolds-Averaged Navier-Stokes)

Reynolds-Averaged Navier-Stokes (RANS) methods solve the time-averaged Navier-Stokes equations, which involves modeling all turbulent scales. This approach is characterized by:

- Equations: Solves the time-averaged Navier-Stokes equations with additional turbulence models to represent the effects of turbulence.
- Turbulence Models: Includes models like k-ε, k-ω, and others to approximate the effects of turbulence.
- Mesh Resolution: Requires a coarser mesh compared to DNS and LES, as it does not need to resolve individual turbulent eddies.
- Computational Demand: Much lower computational cost compared to DNS and LES.
- Accuracy: Less accurate in capturing detailed turbulent structures but provides good predictions for mean flow properties.
- Applications: Widely used in industrial applications, including aerodynamics, hydrodynamics, and heat transfer, where computational efficiency is critical.

2.4. Statistic law of Reynold and faver

(Reynolds-Averaged Navier-Stokes): This method involves a statistical treatment of the Navier-Stokes equations through the Reynolds decomposition. In turbulent flow, any vector or scalar quantity can be separated into an average part and a fluctuating part.

Here are some examples of Reynolds decomposition:

$$U(x,t) = \overline{u(x,t)} + u'(x,t) \tag{2.6}$$

$$\phi(x,t) = \overline{\phi(x,t)} + \phi'(x,t) \tag{2.7}$$

By applying Reynolds decomposition to the variables in the continuity and Navier-Stokes equations, and then averaging these terms over time, we derive the Reynolds-Averaged Navier-Stokes (RANS) equations. Using mathematical tools:

- The ensemble mean of a quantity, also known as the Reynolds mean, is given by:

$$\overline{f(x,t)} = \underline{lim}\left(\frac{1}{N}\sum_{n=1}^{n} f(x,t)\right) \tag{2.8}$$

If the statistical quantity $\overline{f}$ is independent of time, i.e. $\overline{f(x,t)} = f(x)$ then the ensemble mean is equivalent to a time average:

$$\overline{f}(x) = \underline{lim}\frac{1}{T}\int_0^T f(x,t)\,dt \tag{2.9}$$

The average operator has the following properties:

$$\overline{c \cdot f} = c \cdot \overline{f} \tag{2.10}$$

$$\overline{f+g} = \overline{f} + \overline{g} \tag{2.11}$$

$$\overline{\overline{f}} = \overline{f} \tag{2.12}$$

$$\overline{f'} = 0 \tag{2.13}$$

$$\overline{f \cdot g} = \overline{f} \cdot \overline{g} \tag{2.14}$$

$$\overline{\frac{\partial f}{\partial \xi}} = \frac{\partial \overline{f}}{\partial \xi} \tag{2.15}$$

This composition is injected into the Navier-Stokes equations, which are averaged over density and velocity:

$$\rho = \overline{\rho} + \rho' \tag{2.16}$$

$$u = \overline{u} + u' \tag{2.17}$$

$$\rho \cdot u = \overline{\rho} \cdot \overline{u} + \overline{\rho} u' + \rho' \cdot \overline{u} + \rho' \cdot u' \tag{2.18}$$

$$\overline{\rho \cdot u} = \overline{\rho} \cdot \overline{u} + \overline{\rho' \cdot u'} \tag{2.19}$$

The application of Reynolds decomposition to the compressible Navier-Stokes equations does not therefore lead to a system of equations for the mean field which is formally identical to the original equations. To avoid this problem adopt the FAVRE decomposition which is based on weighted averages with respect to density.

The FAVRE average :

$$\tilde{\varphi} = \frac{\overline{\rho \cdot \varphi}}{\overline{\rho}} \tag{2.20}$$

The decomposition is written :

$$\varphi = \tilde{\varphi} + \varphi'' \tag{2.21}$$

$$\overline{\rho \cdot \varphi} = \overline{\rho} \cdot \tilde{\varphi} \tag{2.22}$$

$$\overline{\rho \cdot \varphi''} = 0 \tag{2.23}$$

$$\overline{\varphi''} \neq 0 \tag{2.24}$$

2.5. Turbulence models

Turbulent flow, characterized by unsteady three-dimensional motion with a broad spectrum of turbulent scales, presents a complex modeling challenge. CFD simulations cannot feasibly resolve the entire range of turbulent length scales, especially in turbomachinery applications where high-energy small-scale fluctuations are prevalent.

An alternative approach widely employed involves time-averaging the Navier-Stokes equations to derive the Reynolds-Averaged Navier-Stokes (RANS) equations. This idealized time-averaging introduces additional terms accounting for stress gradients and heat flux associated with turbulent motion. These terms are expressed in relation to mean flow variables through turbulent models.

Various turbulence models are used within the Reynolds formulation of the momentum equation, with the "k – $epsilon$", The "K ω "and The "S.S.T. "models being particularly common.

The k - $epsilon$ model

This model is based on the two transport equations that of turbulent kinetic energy k and that of turbulent dissipation ε , with these two variables (k, ε) the turbulent Viscosity μ_t is calculated so that the Reynolds tensor is defined.

The two equations are expressed as follows:

The turbulent kinetic energy equation:

$$\frac{\partial\left(\overline{\rho}.k\right)}{\partial t}\frac{\partial}{\partial x_j}(\overline{\rho}.u_j.k) = \frac{\partial}{\partial x_j}\left[(\mu + \frac{\mu_T}{\sigma_k})\frac{\partial k}{\partial x_j}\right] + P_K - \overline{\rho}.\varepsilon \tag{2.25}$$

The dissipation rate equation :

$$\frac{\partial\left(\overline{\rho}.\varepsilon\right)}{\partial t}\frac{\partial}{\partial x_j}(\overline{\rho}.u_j.\varepsilon)=\frac{\partial}{\partial x_j}\left[(\mu+\frac{\mu_T}{\sigma_\varepsilon})\frac{\partial\varepsilon}{\partial x_j}\right]+\frac{\varepsilon}{k}(C_{\varepsilon 1}.P_K.C_{\varepsilon 2}.\overline{\rho}.\varepsilon) \qquad (2.26)$$

With :

P_K : The production of turbulence due to viscous forces and buoyancy.

Table 2-1: *k* - *epsilon* model constants in ANSYS CFX.

C_μ	C_{S1}	$C_{\varepsilon 2}$	σ_k	σ_ε
0.09	1.44	1.92	1.0	1.3

The k-ω model:

This turbulence model uses two transport equations, a dissipation transport equation ε and the other equation proposed by Wilcox using the turbulence frequency ω .

The turbulent kinetic energy equation:

$$\frac{\partial\left(\overline{\rho}.k\right)}{\partial t}\frac{\partial}{\partial x_j}(\overline{\rho}.u_j.k)=\frac{\partial}{\partial x_j}\left[(\mu+\frac{\mu_T}{\sigma_{k1}})\frac{\partial k}{\partial x_j}\right]+P_K-\beta.\overline{\rho}.k.\omega \qquad (2.27)$$

The turbulent frequency equation:

$$\frac{\partial\left(\overline{\rho}.\omega\right)}{\partial t}\frac{\partial}{\partial x_j}(\overline{\rho}.u_j.\omega)=\frac{\partial}{\partial x_j}\left[(\mu+\frac{\mu_T}{\sigma_{\omega 1}})\frac{\partial\omega}{\partial x_j}\right]+\alpha_1.\frac{\omega}{k}.P_k-\beta_1.\overline{\rho}.\omega^2 \qquad (2.28)$$

Table 2-2: $k\omega$ model constants in ANSYS CFX.

β’	α_1	β_1	σ_k	σ_ω
0.09	5/9	0.075	2.0	2.0

The S.S.T model:

The Shear Stress Transport (SST) turbulence model, developed from the Baseline (BSL) model, was introduced by Menter in 1994. This hybrid model leverages the strengths of both the K-epsilon (K-ε) and k-omega (k-ω) models. The SST model enhances versatility by applying the K-omega formulation near walls and the K-epsilon formulation in regions of free

flow, away from the walls. The aim of the SST model is to utilize the K-omega model in the wake region and the K-epsilon model in the boundary layer and the remainder of the domain. This combined approach of the SST model can be represented by the transition function as follows:

$$S.S.T = F(k-\omega) + (1-F)(k-\varepsilon) \tag{2.29}$$

Both turbulence models, Baseline (BSL) and SST, share the same structure, yet the SST model introduces a novel formulation for turbulent kinematic viscosity aimed at improving separation prediction.

- The equation for turbulent kinetic energy transport :

$$\frac{\partial(\overline{\rho}.\omega)}{\partial t}\frac{\partial}{\partial x_j}(\overline{\rho}.u_j.\omega) = \frac{\partial}{\partial x_j}\left[(\mu+\frac{\mu_T}{\sigma_{\omega 2}})\frac{\partial \omega}{\partial x_j}\right] + (1-F_1).2.\overline{\rho}.\frac{\partial k}{\sigma_{\omega 2}.\omega.\partial x_j}.\frac{\partial \omega}{\partial x_j} + \alpha_3.\frac{\omega}{k}.P_k - \beta_3.\overline{\rho}.\omega^2 \tag{2.30}$$

The frequency transport equation:

$$\frac{\partial(\overline{\rho}.k)}{\partial t}\frac{\partial}{\partial x_j}(\overline{\rho}.u_j.k) = \frac{\partial}{\partial x_j}\left[(\mu+\frac{\mu_T}{\sigma_{k2}})\frac{\partial k}{\partial x_j}\right] + P_K - \beta'.\overline{\rho}.k.\omega \tag{2.31}$$

The constants used by the S.S.T model are determined in the same way as the constants in the BSL model.

-For k-ω model

Table 2-3: k-ω model constants in ANSYS CFX.

α_1	β_1	β’	$\sigma_{\omega 1}$	σ_{k1}
0.5	0.075	0.09	2	2

-For k - $epsilon$ model

Table 2-4: k - $epsilon$ model constants in ANSYS CFX.

α_2	β_2	β’	$\sigma_{\omega 2}$	σ_{k2}
0.44	0.0828	0.09	1/0.856	1

2.6. Boundary Layer

Within the boundary layer, the parameters used to determine the sign and magnitude of the stability effect are the Richardson numbers R_{i-C} and $R_{i-\Omega}$:

$$R_{i-C} = \frac{U / R_0}{(\partial U / \partial y)} \tag{2.32}$$

$$R_{i-\Omega} = \frac{-2\Omega}{(\partial U / \partial y)} \tag{2.33}$$

The Richardson number R_{i-c} determines the stability of the boundary layer on a convex or concave surface.

- For$R_{i-c} > 0$: A low turbulent exchange with the free stream leads to the stabilization of the boundary layer.
- For$R_{i-c} < 0$: Increased turbulent mixing results in the instability of the boundary layer.

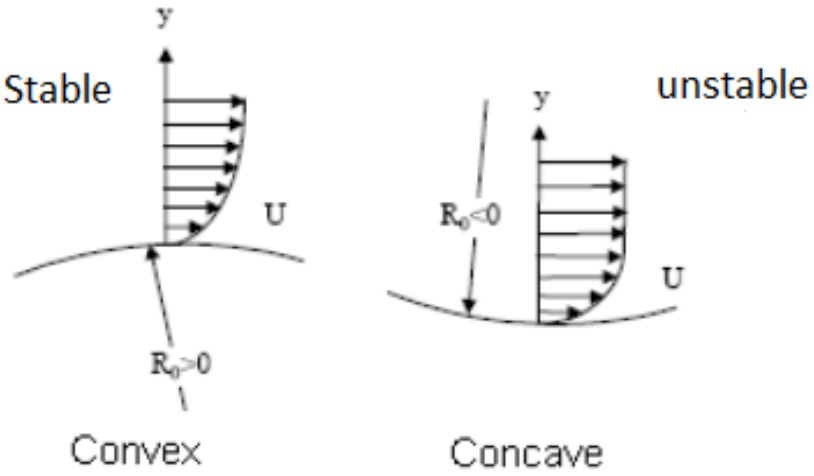

Figure 2.2: The curvature effect.

herefore, we can conclude that the boundary layer on a rotating plate will behave as follows:

- $R_{i-\Omega} > 0$: The boundary layer is stable.
- $R_{i-\Omega} < 0$: The boundary layer is unstable.

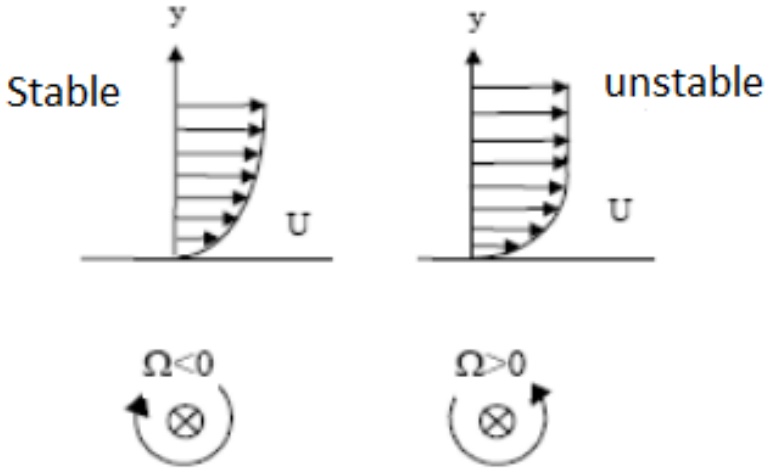

Figure 2.3: The rotation effect.

2.7. Wall Treatment

Effective wall treatment is crucial for the numerical simulation of turbulent flow. Two common approaches are used to model the flow in this region:

1. **Near-Wall Approach**: This method involves solving the equations right up to the solid wall, where the boundary condition is applied.
2. **Wall Function Approach**: This method stops the computation at a certain distance from the wall and uses a wall function to connect the computed region with the wall. In this case, the wall function does not solve the flow directly but calculates the appropriate boundary conditions to be applied at the first node.

The wall function approach in ANSYS CFX 23 is an extension of the LAUNDER and Spalding method. In the logarithmic region, the tangential velocity near the wall is related to the wall shear stress τ_ω by a logarithmic relation:

$$u^+ = \frac{u_t}{u_T} = \frac{1}{K}\ln(y^+) + \mathrm{C} \tag{2.34}$$

- ✓ $y^+ = \frac{yu_T}{v}$
- ✓ $T_\omega = \rho u_T^2$
- ✓ u^+ is the velocity near the wall
- ✓ u_T is the friction velocity,

- ✓ u_t is the known tangential velocity at a distance Δy from the wall,
- ✓ y^+ is the dimensionless wall distance,
- ✓ T_ω is the wall shear stress,
- ✓ k is the von Karman constant,
- ✓ C is a logarithmic constant dependent on wall roughness.

Regarding mesh considerations, the two approaches dictate different choices for y^+:

- **Near-Wall Approach**: Solves the equations down to the viscous sublayer. The first node should be very close to the wall, typically at $y^+ \approx 1$ This approach is suitable for turbulence models like Spalart-Allmaras, K-ω and SST, which are designed to resolve the flow up to the wall.
- **Wall Function Approach**: Places the first node beyond the buffer layer, typically at $y^+ \geq 30$. This method is used by the K-ε turbulence model, reducing the number of computational cells in the boundary layer.

CHAPTER 3: SIMULATION STEPS

3.1. Introduction

With the advancement of numerical simulation tools and the increasing power of computing resources, numerous software programs have been developed to tackle complex three-dimensional problems, especially in fluid mechanics and turbomachinery. Some of the most well-known simulation software includes ANSYS CFX, GAMBIT, FLUENT, STAR-CD, and NUMECA. In this work, ANSYS CFX was used to numerically model the compressible flow in a centrifugal compressor.

3.2. Software Presentation CFX-23:

ANSYS CFX is a comprehensive computational fluid dynamics (CFD) software suite designed to simulate and analyze various fluid flow phenomena. It is widely used in the field of turbomachinery, particularly for the design and optimization of pumps, fans, compressors, and turbines.

This software provides numerous multiphase models and numerical schemes, enabling users to model a wide range of fluid mechanics problems. Similar to many other software packages, ANSYS CFX includes a variety of tools and modules for:

1. Geometry creation
2. Mesh generation
3. Calculation

3.2.1. ANSYS CFX –Workbench

The first step involves defining the geometry of the impeller of the centrifugal compressor using CFX-Workbench This three-dimensional tool is designed for quick and efficient geometry creation and is specialized in the turbomachinery field, including compressors (centrifugal and axial), pumps, fans, turbines, and more.

For our study, we imported [.dat] files containing the coordinate points for the geometry of the impeller, hub, and compressor casing. These data files were exported from BladeGen and represent the precise geometry of the compressor under study.

3.2.2. ANSYS CFX - TurboGrid

TurboGrid is used to generate a structured mesh tailored to various types of turbomachinery applications. However, there is no definitive rule for achieving high mesh quality for complex geometries, such as the impeller of a centrifugal compressor. Structured meshing is more easily accomplished using a multi-block geometry approach, which involves dividing the computational domains into several compartments of simple geometric shapes and meshing them separately.

- **Advantages**: This method is economical in terms of the number of elements required, reduces the risk of numerical errors, and ensures relatively rapid convergence in calculations.
- **Disadvantages**: For complex geometries like the impeller of a centrifugal compressor, meshing with this technique is not only difficult to generate but also often results in poor quality.

In our case, the impeller geometry is relatively simple and does not require block meshing.

Machine Definition

Opening TurboGrid, this is the first page in the ANSYS TurboGrid interface.

In this window we first define the number of blades as well as the type of machine with its axis of rotation and the unit of distance and the direction of rotation of our centrifugal compressor. Here is the information to insert in the Machine Data section.

Figure 3.1: machine details.

Below are the factors we use to generate our mesh:

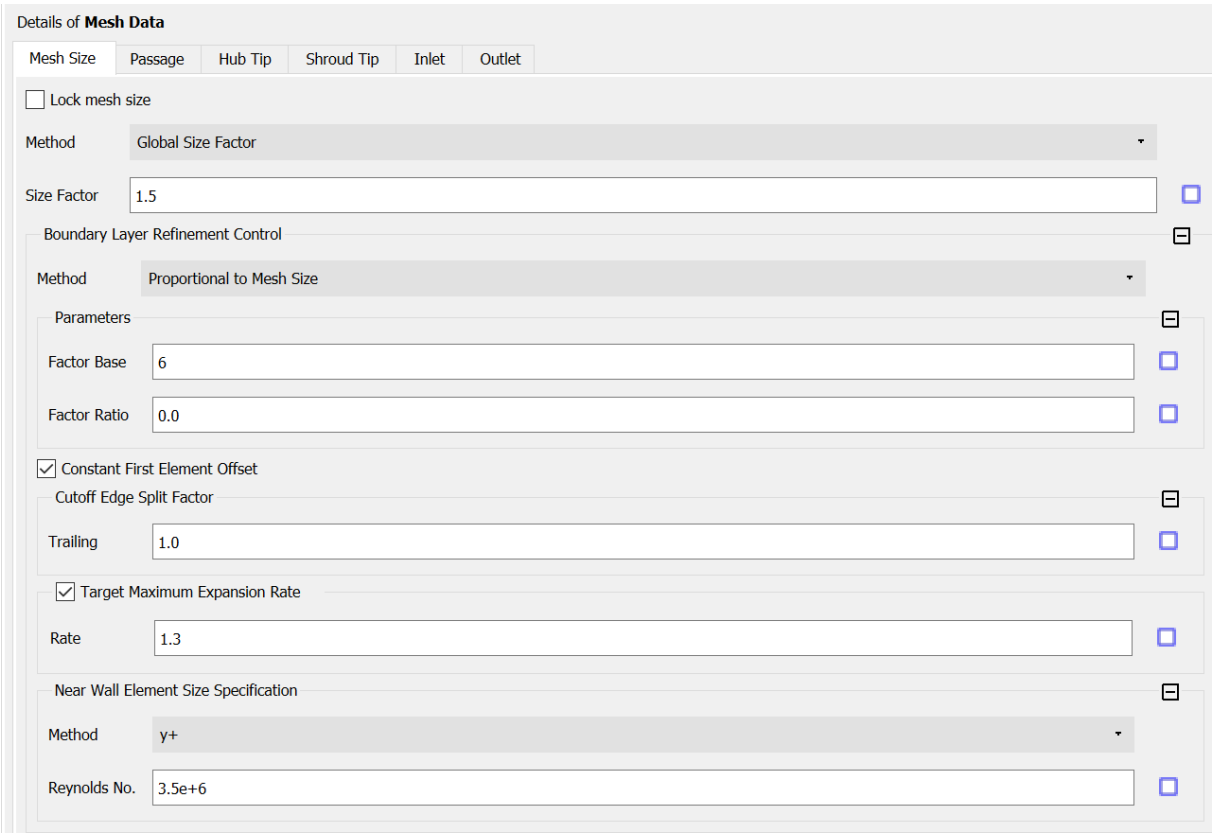

Figure 3.2: Mesh details.

Mesh Size

- The Global Size Factor method is used to define the overall size of the mesh. To achieve a higher mesh resolution, you can adjust the scale factor through the Scale Factor setting. It's important to note that this adjustment does not result in a linear change in the overall mesh size. When operating in this mode, any modifications to the spanwise mesh size, boundary layer refinement, or local edge refinements will not alter the Global Size Factor. Instead, these adjustments may lead to changes in the overall mesh size. This factor is particularly useful when combined with proportional refinement, as it allows for scaling the mesh size effectively during a mesh refinement study. [11]

- Proportional to Mesh Size

This option controls the number of elements across the boundary layer region in proportion to the values specified for Factor Base and Factor Ratio. This method maintains similar expansion rates when the Global Size Factor is changed. If the blade has a cut-off edge, Factor Ratio also controls the number of elements along the cut-off edge.

Increasing the value of Factor Base or Factor Ratio increases the number of elements across the boundary layer and along the cut-off edge (if applicable). Conversely, decreasing the value of Factor Base or Factor Ratio decreases the number of elements. The number of elements across the boundary layer is calculated as Base Count * Global Size Factor * (Factor Base + Factor Ratio * Global Size Factor). The default values of Factor Base and Factor Ratio are 3 and 0 respectively. [11]

- Constant First Element Offset

When Constant First Element Offset is selected, TurboGrid uses a double-sided node distribution (a non-constant expansion rate) for the boundary layer. In this case, the near-wall expansion rates that are reported in the Boundary Layer Control object indicate the approximate minimum and maximum values based on a sample of the layer values.
When Constant First Element Offset is not selected, TurboGrid uses a single sided node distribution for the boundary layer; at any given position around the blade (in the blade-to-blade view), there is a constant expansion rate across the boundary layer. In this case, the user-specified first element offset is applied approximately as an average offset.

- Near Wall Element Size Specification

The Near Wall Element Size Specification setting controls the method by which the near-wall node spacing is specified on the Passage and Shroud Tip tabs. The near-wall node spacing is the distance between a wall (for example, hub, shroud, or blade) and the first layer of nodes from the wall. [11]

- **Y Plus**

Y^+ is a non-dimensional distance used to characterize the coarseness or fineness of a mesh in a particular flow model. It is a critical parameter in turbulence modeling to determine the appropriate cell size near the domain walls. The turbulence model's wall laws impose restrictions on the Y^+ value at the wall. Specifically, the SST (Shear Stress Transport) model requires a Y^+ value between approximately 0 and 5. Higher flow speeds near the wall result in higher Y^+ values, necessitating a finer grid size near the wall.

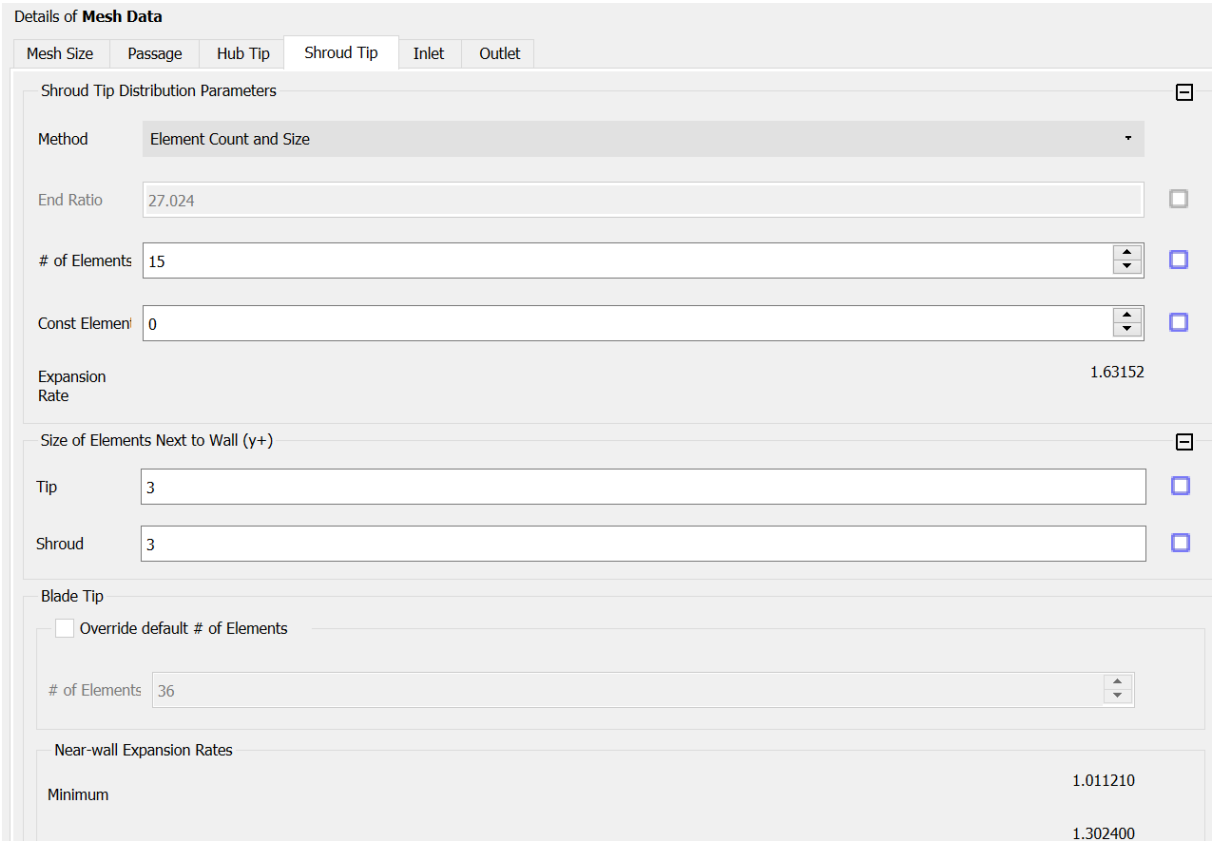

Figure 3.3: Shroud Tip clearance.

The 'Match Expansion at Blade Tip' parameter is used to refine the mesh in the vicinity of the compressor shroud.

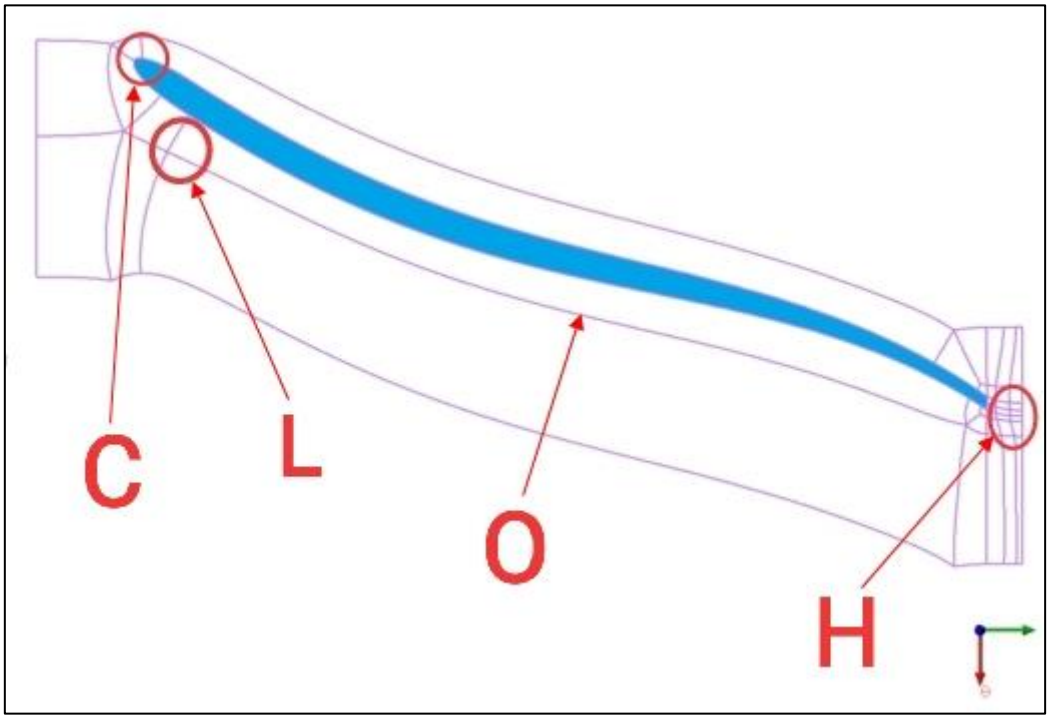

Figure 3.4: Mesh types.

Modelling the moving part (impeler) and taking into account the various interactions involved (between the impeller and Shroud) requires the use of an unstructured mesh, as the intersection zone of the two interfaces (the moving parts and the fixed part) is inside the calculation domain. For mesh creation, there is a special topology of the type H / J /C/ L and of the type ‘ O ’ around the interface.

L and of type ‘ O ’ around the vane and the walls, see figure 3.4.

Here's the refinement we do in the trailing edge area of the blade to reduce the value of Y+. This refinement is performed as follows: zoom into the trailing edge area, right-click on the mesh boundary, select the Edge split control parameter, use the factors shown in the figure below for each area, bearing in mind that the default value of this factor is 1.

Here is the result obtained from this operation.

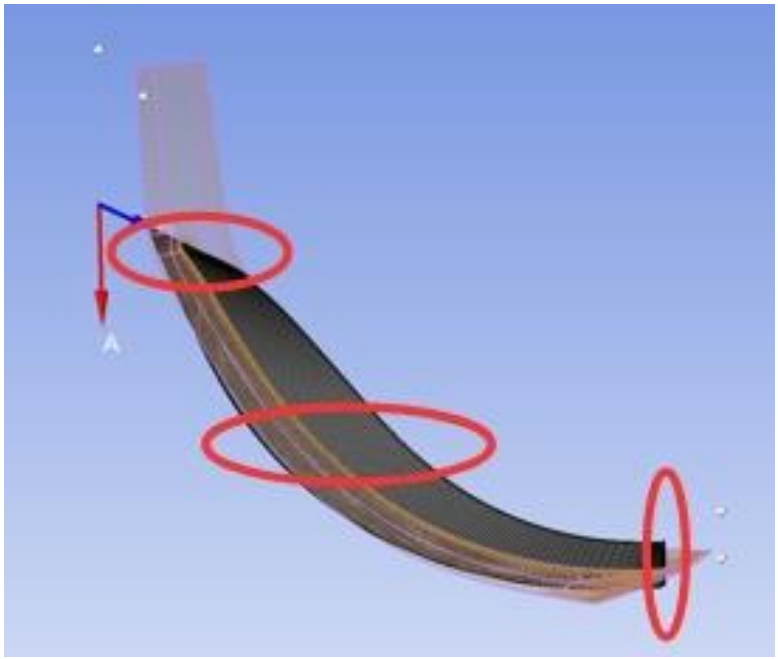

Figure 3.5: Mesh of the blade.

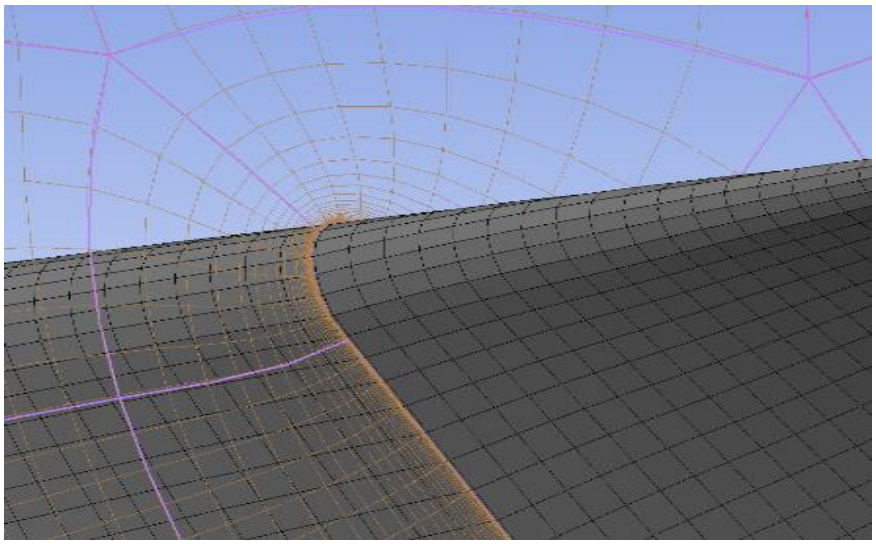

Figure 3.6: Mesh at the Leading edge.

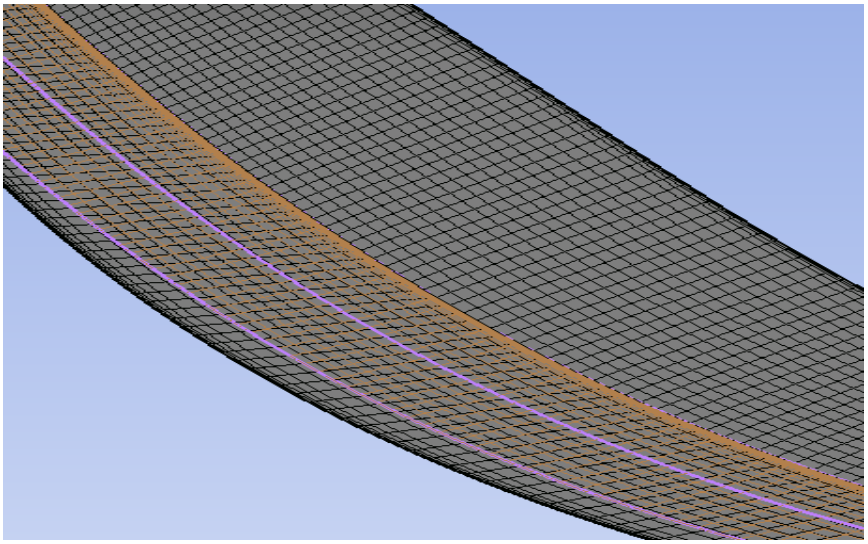

Figure 3.7: Mesh at the Medium.

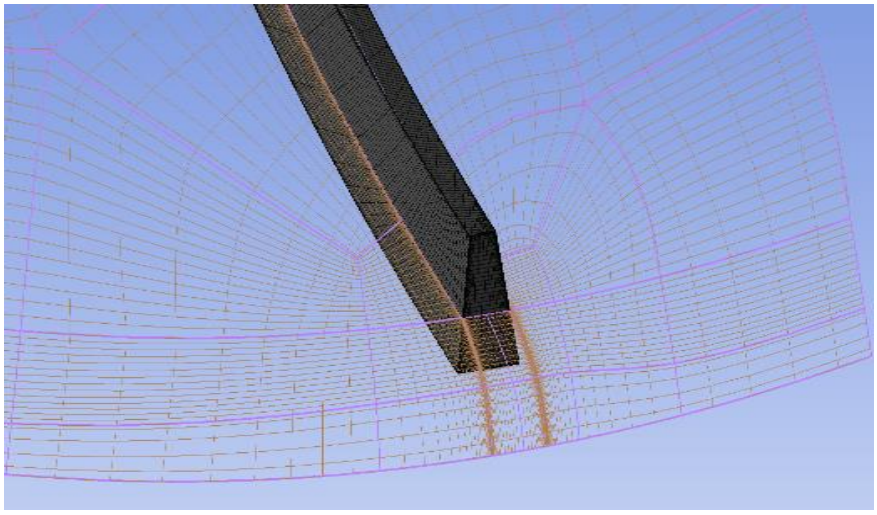

Figure 3.8: Mesh at the trailing edge.

Meshing Statistics

Ensuring high-quality mesh in a turbomachine involves adhering to specific criteria:

- ✓ **Maximum Face Angle**: This represents the largest angle of all the faces touching a node and measures distortion. For our mesh, this angle is 156.5 degrees.
- ✓ **Minimum Face Angle**: This is the smallest angle between two edges touching a node, valued at 23 degrees.
- ✓ **Connectivity Number**: This indicates the number of elements connected to a node, with a maximum value of 12 and a minimum value of 0.
- ✓ **Volume Element Ratio**: This is the ratio of the largest volume to the smallest volume associated with a node, and this ratio must be positive.
- ✓ **Edge Length Ratio**: This ratio compares the longest edge to the shortest edge on the same face, with a maximum value of 10.
- ✓ **Minimum Volume**: This ensures that all mesh volumes are positive, preventing any negative volumes in the fluid flow.

For a very high-quality mesh, all six conditions must be satisfied. Although one of these conditions is not fully met, the error margin is only 1%, which is acceptable. This slight deviation will not compromise the accuracy or reliability of our calculations, allowing us to proceed without risk of divergence or false values.

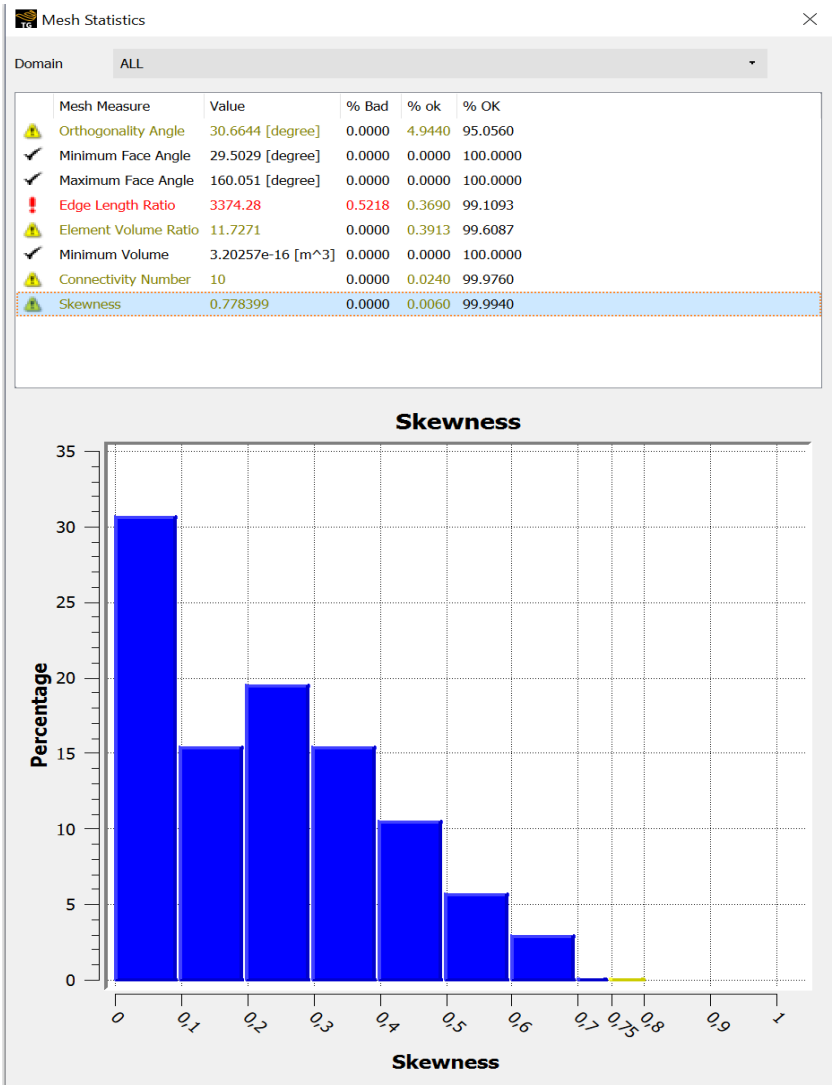

Figure 3.9: Mable of requirements.

Mesh Quality Considerations

In areas of high geometric complexity mesh elements can become distorted. Poor quality elements can lead to poor quality results or, in some cases, no results at all! There are a number of methods for measuring mesh element quality (mesh metrics*). For example, one important metric is the element 'Skewness'. Skewness is a measure of the relative distortion of an element compared to its ideal shape and is scaled from 0 (Excellent) to 1 (Unacceptable).

Skewness mesh metrics spectrum

Excellent	Very good	Good	Acceptable	Bad	Unacceptable
0-0.25	0.25-0.50	0.50-0.80	0.80-0.94	0.95-0.97	0.98-1.00

Figure 3.10: Mesh Quality.

3.3. ANSYS CFX

This module of the CFX software allows for the simulation of flows in intricate geometries, such as those found in centrifugal compressor impellers and radial diffuser assemblies. It offers designers a reliable and precise tool for analyzing internal flows, which can vary from compressible to incompressible, stationary to non-stationary, laminar to turbulent, and from subsonic to supersonic.

The initial set of equations is derived from the principles of mass, momentum, and energy conservation to formulate the Navier-Stokes equations.

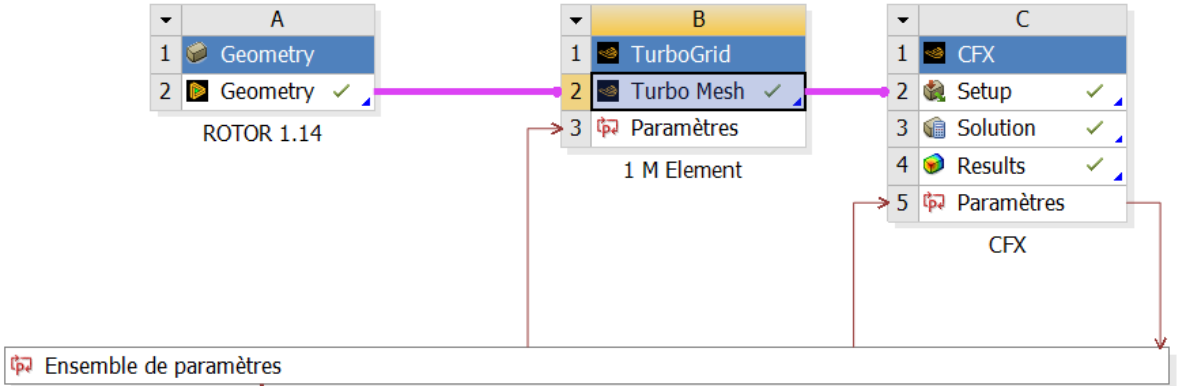

Figure 3.11: simulation schematic.

The CFX software consists of three modules:

- ✓ The Pre-Processing module (ANSYS CFX .23 Pre-Processor)
- ✓ The Solver module.
- ✓ Post-Processing module (ANSYS CFX .23 -Post-Processor)

3.3.1. The Pre-Processing Module (CFX Pre-Processor)

In this module, the boundary and initial conditions for the flow regimes are defined. The numerical scheme is selected, and the number of iterations, convergence criteria, and the fluid properties are set. The computational domain consists of two meshes: one for the impeller and one for the diffuser. The interface between the impeller and diffuser is simulated by a smooth diffuser attached to the impeller.

ANSYS CFX-TASCflow offers three different types of interfaces:

1. **Frozen Rotor Type**: This interface models the flow at a specific relative position between the impeller and the diffuser. It is used in quasi-stationary calculations and is suitable when the flow velocity is relatively high compared to the machine speed.

2. **Blade-to-Blade Type (Stage)**: This calculation is performed for two rows of blades simultaneously. The transition from the relative to the absolute frame of reference is achieved by computing the circumferential average of the flow. This type is also employed when a stationary solution is needed in each frame of reference.
3. **Periodic Type**: This interface is used for the unsteady calculation of a sliding interface, allowing the flow to be calculated at different positions of the interface.

Work carried out in the Pre-Processing module section

First, open the "Turbo Mode" tool and make the following changes:

1. Click on the Ansys Setup module on the ANSYS home screen.
2. In this section, redefine the type of machine and its axis of rotation, and specify whether the flow is steady or transient.

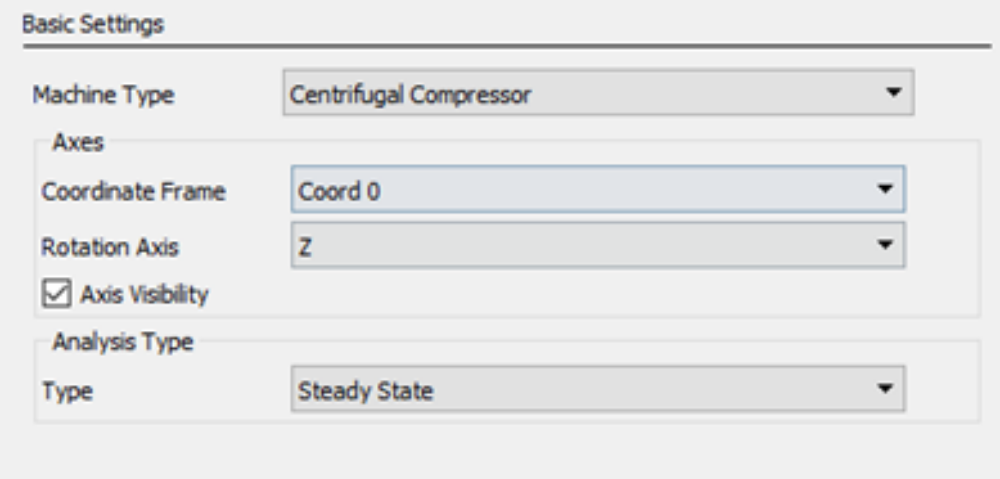

Figure 3.12: turbo mode parameter.

In the final part of the post-processing Turbo mode, select the type of gas (Air as a perfect gas with gamma = 1.4) and set the reference pressure (1 atm = 1.013e5 [Pa]). Choose the type of heat transfer (Total Energy with the SST turbulence model) and the resolution method as shown in the image. Additionally, specify the discretization type: High resolution (central scheme) or Upwind with an accuracy of 10E-05.

3.3.2. The Module (Solver)

The Solver module carries out the fundamental calculations to solve the equations of the specified problem. The configuration for the Solver module is as follows:

- **Solver Parameter**: Choose (MPI Local Parallel) to define the number of processors and the distribution of calculations, which can be either parallel or serial, depending on the type and performance of the computation station.

- **Calculation Method**: Choose 'Initial conditions' to ensure that each calculation runs independently.

Ansys CFX-Solver Manager utilizes parameters such as RMS P-Mass, RMS U-mom, RMS W-mom, and RMS H-energy to monitor the convergence of the simulation solution. These parameters represent the root mean square (RMS) residuals for pressure, as well as the U, V, and W components of momentum and H-energy, respectively. RMS residuals quantify the disparity between calculated values and converged values of the corresponding variable. Ensuring convergence of these parameters is crucial for maintaining the accuracy and reliability of the simulation results. Ansys CFX-Solver Manager offers plots displaying the RMS/maximum residuals for pressure and the U, V, and W components of momentum, aiding in the assessment of simulation solution convergence.

Here is what we see when we run the solution:

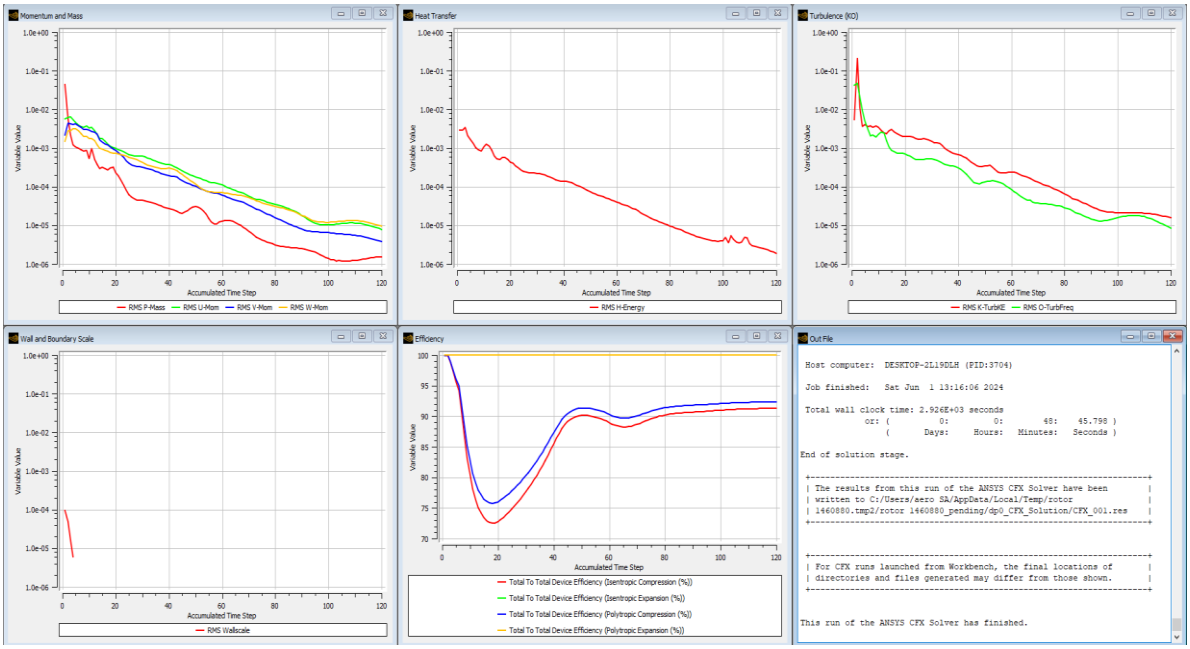

Figure 3.13: Graphs of computational residuals.

As shown in the figure above, the condition for simulation convergence is when all the values of the residuals RMS P-Mass, RMS U-mom, RMS V-mom, RMS W-mom are to the order of 10-5 the calculations are said to be convergent.

3.3.3. The Post-Processing Module

The post-processing module in Ansys CFX is where engineers and analysts examine and analyze simulation results after the completion of the computational fluid dynamics (CFD)

simulations. This module offers a range of tools and functionalities to visualize, interpret, and extract insights from the simulated data.

3.4. Presentation Geometry of the centrifugal compressor impeller

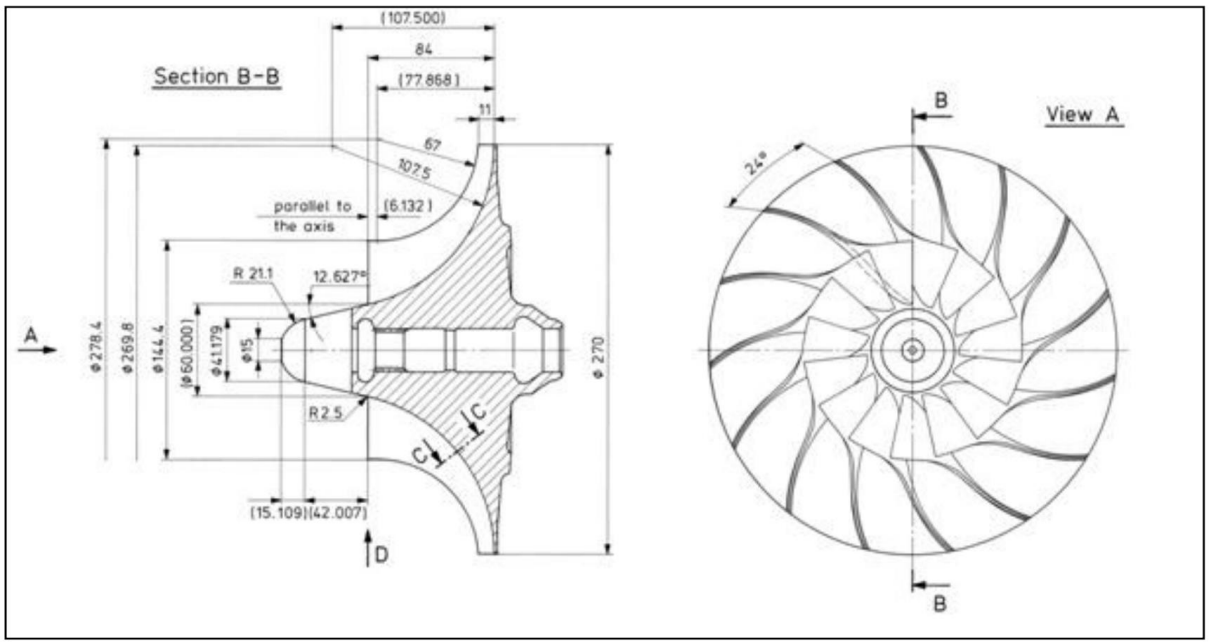

Figure 3.14: Impeller geometry. [12]

3.5. The boundary conditions

The general calculation conditions are summarized in the following table:

Table 3-1: boundary conditions [9].

Characteristic	ANSYS CFX .23
simulation domain	a channel between the impeller flanges (periodicity condition)
simulation regime	stationary
input condition	total pressure , total temperature
output condition	static pressure
Impeller mesh size	structure
turbulence model	k-ω S.S.T
numerical schema	Second order (High resolution)
average residue	10^{-5}

CHAPTER 4: OPTIMIZATION

4.1. Introduction

Modern centrifugal compressors are engineered to achieve high-pressure ratios with relatively low mass flows. Recent advancements in design have led to compressors that surpass past solutions in terms of both pressure ratio and efficiency. However, there's a trade-off: compressors with the highest pressure ratios tend to have the lowest efficiency, and those with the highest efficiency generally have lower pressure ratios.

Designers often need to find an optimal balance between these two competing objectives. The quality of a new aerodynamic design is thus evaluated based on multiple criteria, making it an inherently multi-objective problem. In this context, evolutionary algorithms are particularly useful. They utilize a population of candidate solutions to aid in designing new aerodynamic models, helping to achieve the best possible compromise between pressure ratio and efficiency.

4.2. History and development of optimization

Optimization, the practice of making systems as efficient as possible, has a rich history. It began with ancient Greek mathematicians like Euclid and Archimedes, who laid the groundwork with their geometric explorations. The Islamic Golden Age saw further advancements with algebra, particularly through Al-Khwarizmi.

The 17th century marked a significant leap with the development of calculus by Newton and Leibniz, which introduced methods for finding maxima and minima. In the 18th century, Euler and Lagrange furthered the field with the calculus of variations.

The 19th century brought innovations like Lagrange multipliers for constrained optimization. In the early 20th century, mathematicians like Hilbert and von Neumann formalized optimization theories, contributing to linear programming and game theory.

The mid-20th century saw George Dantzig's simplex method revolutionize linear programming, and nonlinear programming algorithms emerged. The 1980s introduced interior-point methods and evolutionary algorithms, broadening the scope of optimization.

In the 21st century, optimization has integrated with machine learning and high-performance computing, enabling advancements in various industries. Metaheuristic algorithms and big data

analytics have further refined optimization techniques, driving innovation in engineering, economics, logistics, and beyond.

4.3. Types of optimization

Optimization can be categorized into several types based on various factors such as the problem structure, solution approach, and application domain. Here are some common types of optimization:

- Continuous Optimization: This type deals with optimizing functions with continuous variables. It includes techniques like gradient descent, Newton's method, and conjugate gradient methods.
- Discrete Optimization: Discrete optimization involves finding the best solution from a finite or countably infinite set of feasible solutions. Examples include combinatorial optimization problems like the traveling salesman problem (TSP) and the knapsack problem.
- Linear Programming: Linear programming (LP) involves optimizing a linear objective function subject to linear equality and inequality constraints. LP has applications in resource allocation, production planning, and transportation.
- Nonlinear Optimization: Nonlinear optimization deals with optimizing nonlinear objective functions subject to nonlinear constraints. Techniques like the simplex method, gradient-based methods, and genetic algorithms are commonly used for nonlinear optimization.
- Integer Programming: Integer programming (IP) involves optimizing a linear or nonlinear objective function subject to integer constraints on the decision variables. It includes techniques like branch and bound, cutting plane methods, and branch and cut.
- Mixed-Integer Programming: Mixed-integer programming (MIP) extends integer programming by allowing some decision variables to be continuous while others are integer. MIP problems are common in production scheduling, facility location, and network design.
- Multi-Objective Optimization: Multi-objective optimization deals with optimizing multiple conflicting objectives simultaneously. It aims to find a set of Pareto-optimal solutions representing trade-offs between the objectives.
- Stochastic Optimization: Stochastic optimization considers optimization problems with uncertain or probabilistic parameters. It involves techniques like stochastic gradient descent, simulated annealing, and evolutionary algorithms.

- Global Optimization: Global optimization aims to find the global optimum of a function over its entire feasible region. It often requires exploring a large search space and is used in fields like engineering design, machine learning, and finance.

4.4. Optimization problem statement

Formulation of an optimization problem involves defining the objective function and constraints. It usually entails minimizing or maximizing a function $f(x)$ subjected to specific constraints. Mathematically, it can be represented as follows:

Find $\boldsymbol{X} = \{ 1, x2 , xn \}$ That minimizes $f(\boldsymbol{X})$

Subject to constraints

$$\begin{cases} g_j(\boldsymbol{X}) \leq 0, j = 1,2, \dots \text{ m} \\ l_j(\boldsymbol{X}) = 0, j = 1,2, \dots , \text{p} \end{cases}$$

With :

In optimization, X represents a vector comprising n variables, known as the design vector, which encapsulates the variables involved in the design process.

$f(X)$denotes the objective function, serving as a benchmark to evaluate and select a desirable design from various alternatives generated during the optimization process. The nature of the objective function varies depending on the problem at hand.

Constraints, both inequality (X) and equality (X), are imposed on the design vector. These constraints, whether related to physical limitations like manufacturability or system performance, must be met to ensure the acceptability of the design. Geometric constraints pertain to physical limitations, while functional constraints restrict system performance.

By way of illustration, the optimization problem is described in the following figure

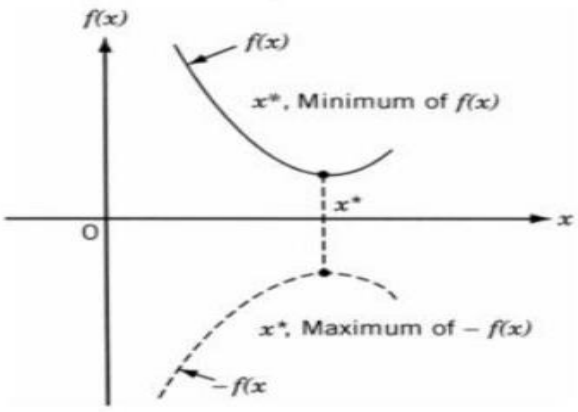

Figure 4.1: Illustration of an optimization problem.

4.5. Classification of Optimization Problems

Optimization problems can be categorized based on various characteristics such as constraints, objective functions, problem structure, equations or variables, and the separability of objectives. Here are the main classifications:

1. Based on Constraints:
    - Constrained Optimization: Problems with specific constraints.
    - Unconstrained Optimization: Problems without constraints.
2. Based on Design Variables:
    - Parametric Optimization: Assigning values to design parameters to minimize an objective function within constraints.
    - Dynamic Optimization: Determining a set of parameters to minimize an objective function over time with constraints.
3. Based on Problem Structure:
    - Optimal Control Analysis: Sequential steps to determine control variables that minimize the objective function under constraints.
    - Non-Optimal Control Analysis: Problems that do not fit the criteria of optimal control.
4. Based on Nature of Equations:
    - Linear Programming (LP): Both constraints and objective function are linear.
    - Non-Linear Programming (NLP): Involves at least one non-linear function.
    - Geometric Programming: Constraints and objective functions are posynomials (sum of power terms).
    - Quadratic Programming: Objective function is quadratic, and constraints are linear.
5. Based on Function Separability:
    - Separable Optimization: The objective function can be separated into simpler functions.
    - Non-Separable Optimization: The objective function cannot be separated.
6. Based on Number of Objective Functions:
    - Single-Objective Optimization: Involves one objective function.
    - Multi-Objective Optimization: Involves multiple objective functions.

Modern engineering often focuses on multi-objective and parametric optimization, which will be the primary focus of this study.

4.6. Optimization in ANSYS CFX

Finite element-based design optimization is a prominent and highly regarded practice in engineering design. This technique involves several key steps, including geometric modeling, mesh generation, the application of the finite element method (FEM), numerical optimization techniques, and various post-processing activities.

Recent advancements in software have made the design process more flexible and dependable. ANSYS 23, the chosen finite element software for this study, is among the leading multi-objective optimization packages in engineering. Its upgraded user interface facilitates seamless interaction between the user and the system, ensuring clarity in conveying the engineer's intent, understanding data relationships, and monitoring analysis status.

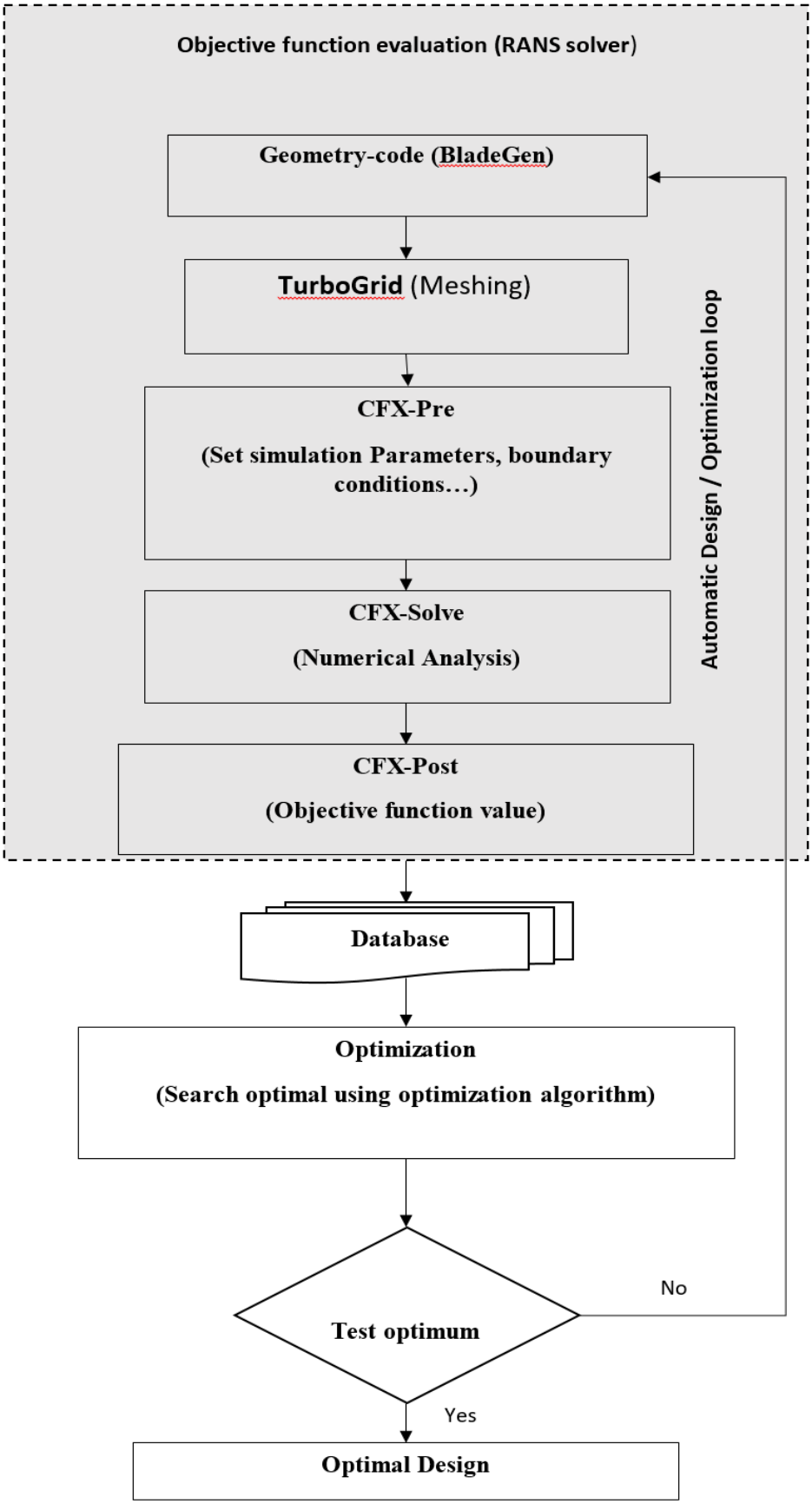

Figure 4.2: Diagram represents the optimization procedure.

ANSYS 23 offers two primary types of optimization, which will be explored in this study:

1. **Parametric Optimization:**
    - **DesignXplorer™ Module:** This module enables parametric optimization, where design parameters are fine-tuned to achieve the best performance within specified constraints.
2. **Topological Optimization:**
    - **Layout Optimization:** Also known as, shape enhancement, this technique optimizes the material layout within a design space to enhance overall performance. It is integrated into a global study module in ANSYS.

By utilizing these optimization methods, ANSYS 23 helps engineers improve and refine their designs, ensuring they meet performance requirements and adhere to constraints, thus making it an essential tool in the engineering design process.

4.6.1. DesignXplorer™ Module

The primary aim of the DesignXplorer™ module is to establish the relationship between design variables and the desired performance outcomes of a model. By analyzing these relationships, analysts can adjust and optimize the design to meet specific performance goals. DesignXplorer™ offers robust tools to perform parametric optimization in both single and multiphysics analyses, making it a powerful solution for exploring, understanding, and optimizing engineering challenges.

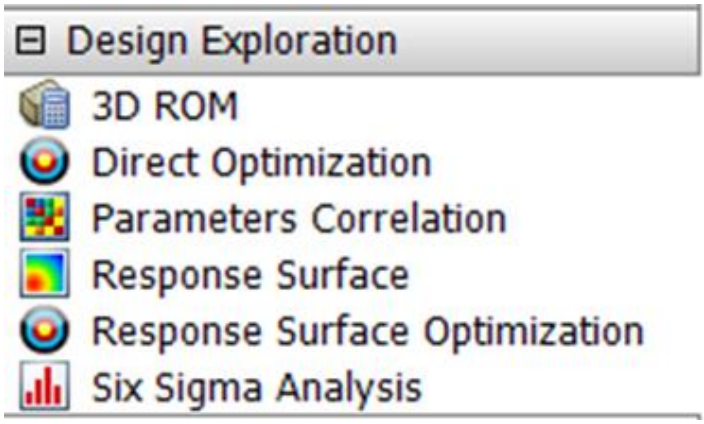

Figure 4.3: the tools used in design Xplorer.

4.6.1.1. Key Features and Workflow of Design Xplorer

1. Design of Experiments (DoE):
    - Parameter Specification: The DoE phase involves defining the type and range of each parameter.

- Efficient Exploration: Design points are automatically selected to efficiently explore the parametric design space.

2. Response Surface Model:
    - Approximate Output Values: A response surface model can be used to quickly estimate output parameters without running full simulations, facilitating rapid evaluation of design variations.
3. Optimization Phase:
    - Objective and Constraint Definition: During this phase, the objectives, constraints, and input parameters are specified.
    - Rapid Configuration Exploration: If a response surface is used, thousands of configurations can be explored within seconds, depending on the study type.
    - Direct Solver Option: Alternatively, if a direct solver is preferred, convergence algorithms are employed to find optimal solutions.
4. Design Robustness Analysis:
    - Performance Understanding: After the optimization phase, a robustness analysis can be conducted to evaluate system performance and understand the trade-offs between different variables.

4.6.1.2. Applications and Benefits

Design Xplorer is recognized as one of the most advanced optimization tools available, extensively used in the engineering industry and various research fields. It empowers engineers to:

- Efficiently explore a wide range of design variables.
- Quickly approximate and evaluate design performance.
- Optimize designs to achieve the best possible performance outcomes.
- Conduct thorough analyses to ensure design robustness and reliability.

By integrating these capabilities, DesignXplorer™ significantly enhances the engineering design process, making it more effective and efficient.

4.7. Optimization Techniques in ANSYS 23 R2

In ANSYS 23 R2, both parametric and topological optimization solvers use a range of specific techniques and algorithms based on the model and output requirements. Once the model constraints and requirements are defined, and the simulation responses are characterized, DesignXplorer™ offers several optimization algorithms, including:

1. Hammersley Shifted Sampling:
    - Purpose: Used for sample generation in analysis.
    - Description: The Shifted Hammersley algorithm is a quasi-random number generator typically employed in Quasi-Monte Carlo analyses. It provides sequences (samples) with low discrepancy, which is useful for integration simulations.
2. Multi-Objective Genetic Algorithm (MOGA):
    - Development: An enhancement of the NSGAII (Non-dominated Sorted Genetic Algorithm), which is a type of evolutionary algorithm.
    - Objective: To increase the adaptive fit of a population of potential solutions to a constrained Pareto front.
    - Procedure: MOGA incorporates evolutionary procedures involving selection, genetic crossover, and mutation operators. The typical steps in a MOGA analysis include:
        - Initial Population: Creation of an initial population from defined parameters.
        - Evolution: Generation of a new population through crossover and mutation, followed by updating the design points of the new population.
        - Convergence Check: If optimization converges, the analysis is completed, and results are generated. If not, the stopping criteria are validated. Depending on whether the maximum number of iterations has been reached, the analysis either terminates or continues with a new population generation.

4.8. Applications and Advancements

ANSYS® continually advances its optimization capabilities, making it a powerful tool for solving complex engineering problems. The flexibility to specify optimization techniques or integrate external tools allows users to tailor the optimization process to their specific needs, ensuring efficient and effective design solutions.

4.9. The work carried out in the Multi-objective Optimization section

In the optimization section, we first use the reponse surface optimization module to define our problem, the parameter to be optimised, the number of points to be calculated and the optimisation method used, as shown below.

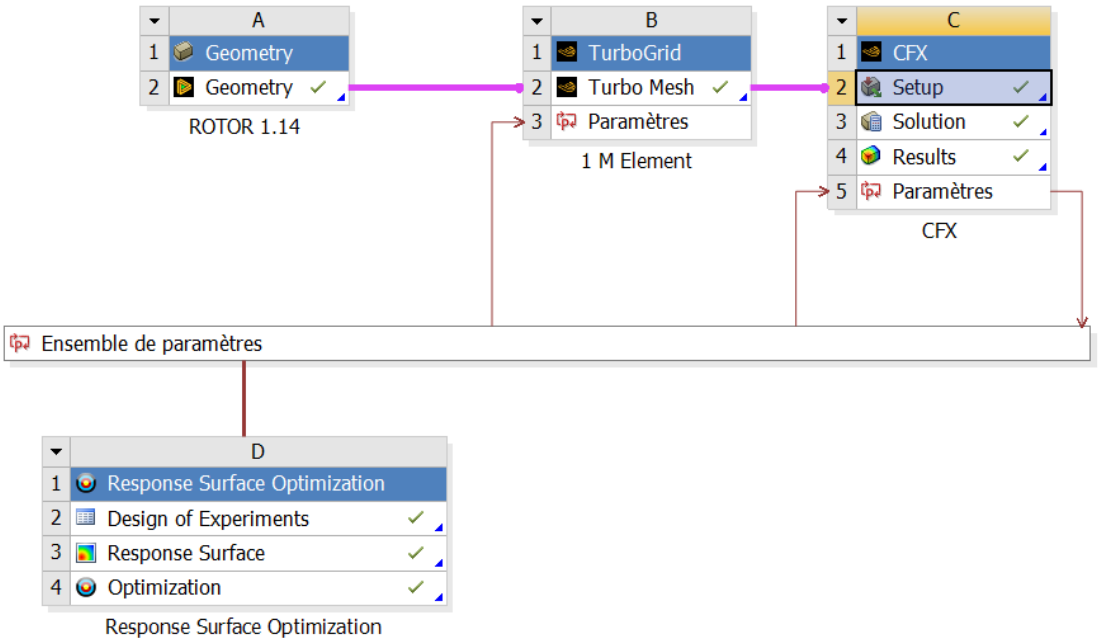

Figure 4.4: optimization diagram.

This is its interface. We define the input parameters and the output parameters as follows:

Input parameters:

- The clearance between impeller and the shroud (P1-Shroud Tip Clearance at leading edge),(P2-Shroud Tip Clearance at Trailing edge)

These are the variables of our objective function and represent our design parameters.

Output parameters:

- Pressure ratio
- Temperature ratio
- Isentropic Efficiency
- Corrected Flow

Table 4-1: Optimization parameter.

	A	B
1		Activé(e)
2	Design of Experiments	
3	Paramètres d'entrée	
4	1 M Element (B1)	
5	P1 - SHROUD TIP Tip Clearance At Leading Edge	☑
6	P2 - SHROUD TIP Tip Clearance At Trailing Edge	☑
7	CFX (C1)	
8	P3 - Flow Analysis 1 Maximum Number of Iterations	☑
9	Paramètres de sortie	
10	CFX (C1)	
11	P4 - PRimpeller 1	
12	P5 - TR 2	
13	P6 - efficiency 3	
14	P7 - mCorige 4	
15	Graphiques	
16	Paramètres en parallèle	
17	Points de calcul vs paramètres	

Formulas in CFX:

1-Pressure ratio impeller(PR)

massFlowAve(Total Pressure in Stn Frame)@P2M /massFlowAve(Total Pressure in Stn Frame)@R1 Inlet

2-Temperature ratio

massFlowAve(Total Temperature in Stn Frame)@P2M /massFlowAve(Total Temperature in Stn Frame)@R1 Inlet

3- isentropic Efficiency

$$\boldsymbol{\eta_{in}} = \frac{\mathrm{PR}_{\mathrm{in}}^{\frac{\gamma}{\gamma-1}} - 1}{\mathrm{TR} - 1}$$

((PRimpeller^0.2857)-1)/(TR-1)

Massin=massFlow()@R1 Inlet *15

4-Corrected Flow

$$\dot{m}_{\boldsymbol{c}} = \dot{m}_{\boldsymbol{in}} \frac{\sqrt{\frac{\boldsymbol{T_{t1}}}{\boldsymbol{T_{ref}}}}}{\frac{\boldsymbol{P_{t1}}}{\boldsymbol{P_{ref}}}}$$

T_{t1} =296 [K]

T_{ref} = 288.15[K]

P_{t1} =0.6[bar]

P_{ref} = 1.013[bar]

massin *1.711176

First, we choose the objective, either maximise or minimise (Maximise in our case).

After choosing the objective and the function, we keep the computational goal 0 so that we don't limit the optimisation to a certain value.

Finally, as we are only interested in maximising the compressor's performance, we are not subject to any type of constraint.

Table 4-2: optimization diagram.

Table of Schematic D4: Optimization

	A	B	C	D	E	F	G	H	I
1	Name	Parameter	Objective			Constraint			
2			Type	Target	Tolerance	Type	Lower Bound	Upper Bound	Tolerance
3	Maximize P4	P4 - PRimpeller	Maximize	0		No Constraint			
4	Maximize P6	P6 - efficiency	Maximize	0		No Constraint			

In this window as an introduction to the clearance interval

Table 4-3: to the clearance interval.

Table of Schematic D4: Optimization

	A	B	C	D
1	Input Parameters			
2	Name	Lower Bound	Upper Bound	
3	P1 - SHROUD TIP Tip Clearance At Leading Edge (mm)	0,24	0,7	
4	P2 - SHROUD TIP Tip Clearance At Trailing Edge (mm)	0,24	0,7	
5	P3 - Flow Analysis 1 Maximum Number of Iterations	800		
6	Parameter Relationships			
7	Name	Left Expression	Operator	Right Expression
*	*New Parameter Relationship*	*New Expression*	<=	*New Expression*

After defining the problem, the objective and the design variable, we start the calculations.

CHAPTER 5: RESULTS AND DISCUSSION

5.1. Introduction:

We present the results derived from numerical simulations and compare them with experimental data for the centrifugal compressor impeller. Additionally, we validate these findings against other studies in the same field.

Initially, we obtained simulation results using the ANSYS CFX software for the standalone compressor impeller. These results were then analyzed to assess the aerothermodynamics parameters at nominal flow rates. Furthermore, we investigated the impact of clearance on the performance of the centrifugal compressor impeller.

5.2. Mesh sensitivity and result validation

In order to compare the experimental results with the numerical results obtained for the variation of the following parameters: the pressure ratio, the static pressure and the iso-tropic efficiency, for the given mesh sizes:

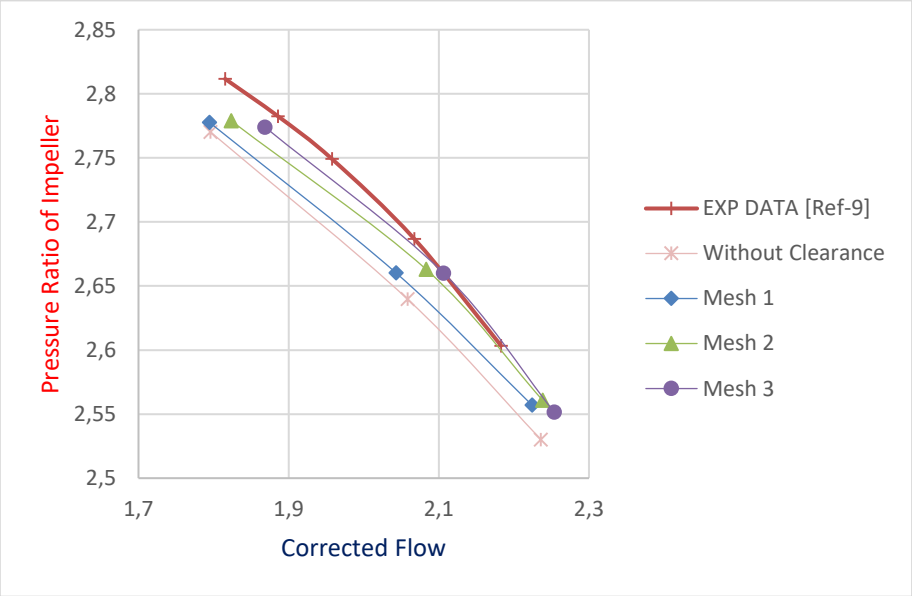

Figure 5.1: Mesh Effect.

numerical calculation	Number of elements
Mesh 1	0.7 M
Mesh 2	0.9 M
Mesh 3	01 M

5.3. Validation of Y^+

The Y^+ coefficient is vital in Computational Fluid Dynamics (CFD) for modeling fluid flow, especially turbulent flows. It significantly impacts the accuracy of numerical simulations. Choosing the correct Y^+ value is essential for precise and reliable results. The accompanying screenshots show Y^+ variations on the blade, hub, and casing surfaces.

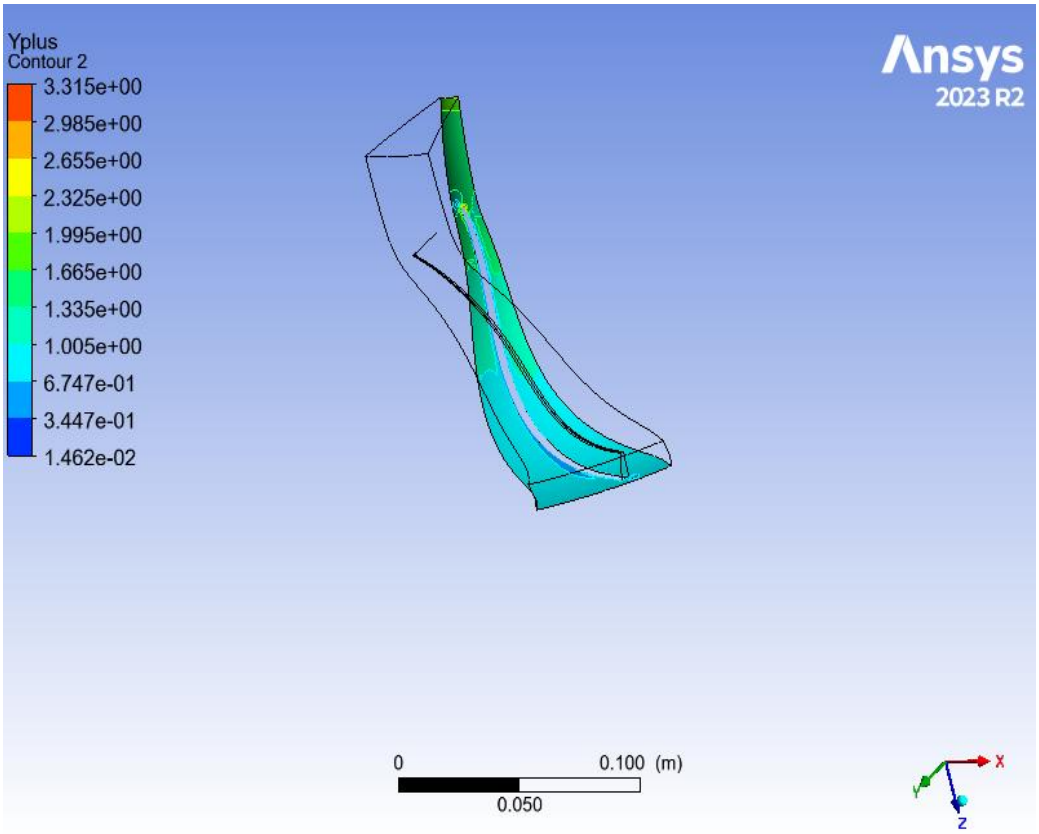

Figure 5.2: Y+ field distribution on the hub surface.

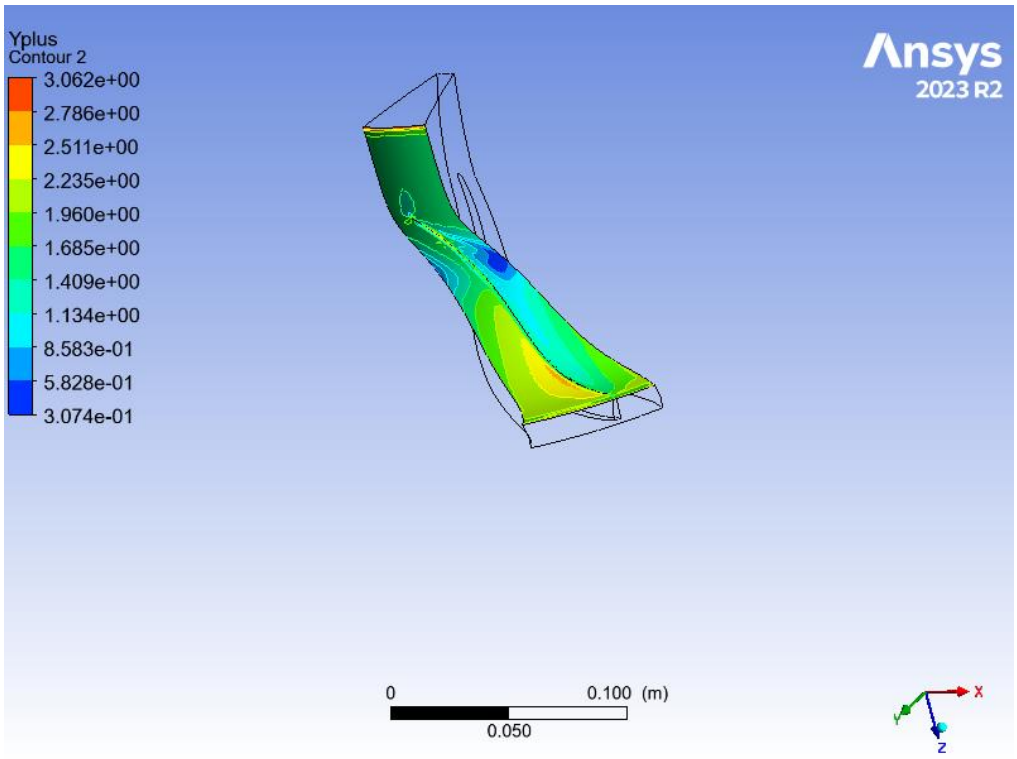

Figure 5.3: Distribution of Y+ over the Shroud surface.

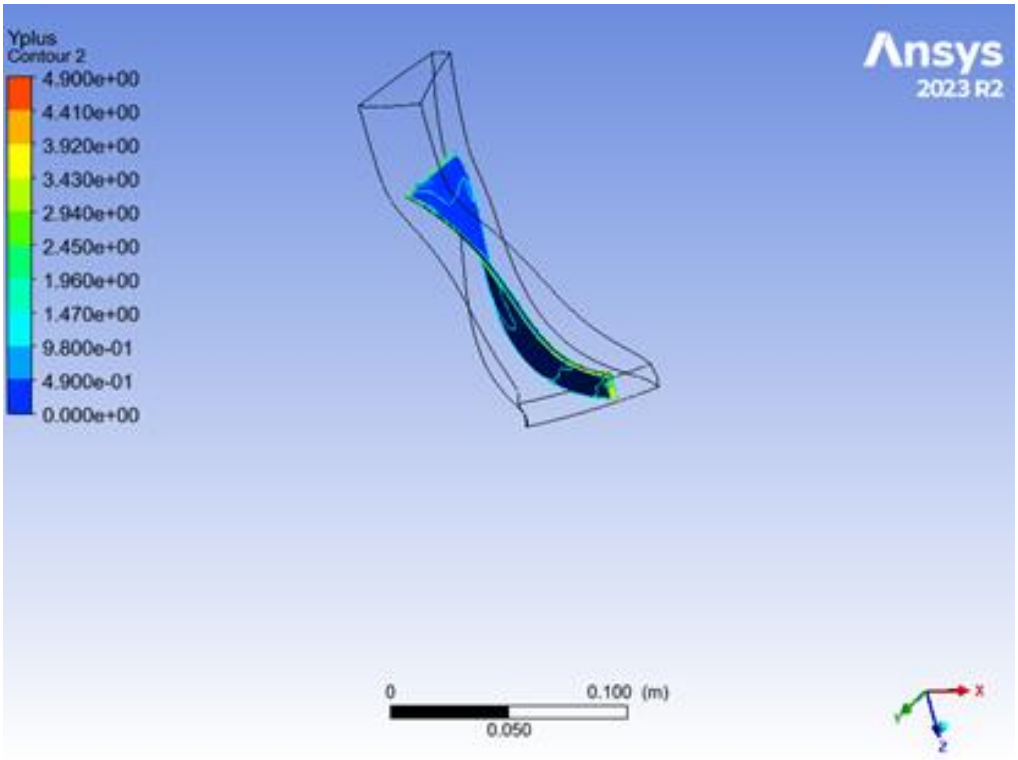

Figure 5.4: Y+ field distribution on compressor blades.

The aerothermodynamics parameters are distributed in three planes:

5.4. Meridian plane

Static pressure:

This figure shows the variation in static pressure in the rotor section in the meridian plane for a corrected flow of 2.1 kg/s and a velocity of 28541 rpm.

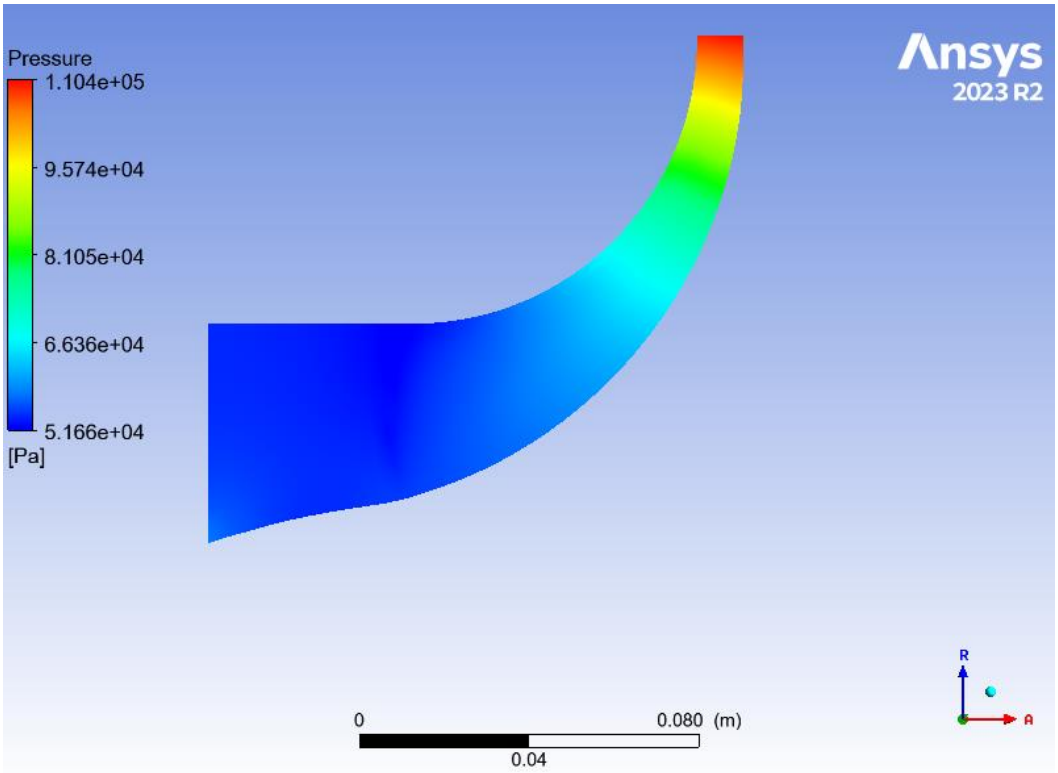

Figure 5.5: Static pressure distribution in the meridian plane.

Flow Dynamics at the Impeller Inlet and Exit

At the impeller inlet, where the radius is small, the mean radius of curvature tends towards infinity due to the axial flow, resulting in a significant centrifugal force. Consequently, the pressure gradient is positive from the hub to the casing. In the middle of the channel, despite strong curvature, the centrifugal force dominates and opposes the curvature-induced force, leading to a negative pressure gradient from the casing to the hub. By the time the flow reaches the wheel exit, the radius of curvature is nearly zero, making the curvature force negligible and the centrifugal force weak.

Total pressure:

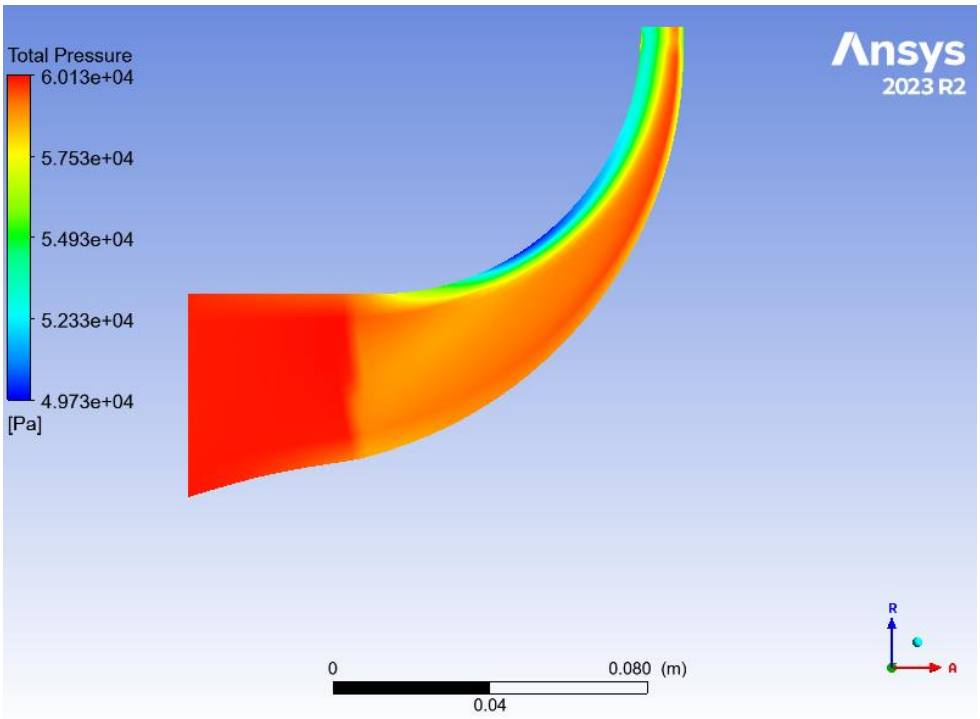

Figure 5.6: Total pressure distribution in the meridian plane.

There is minimal variation in the total pressure from the inlet to the outlet of the compressor impeller.

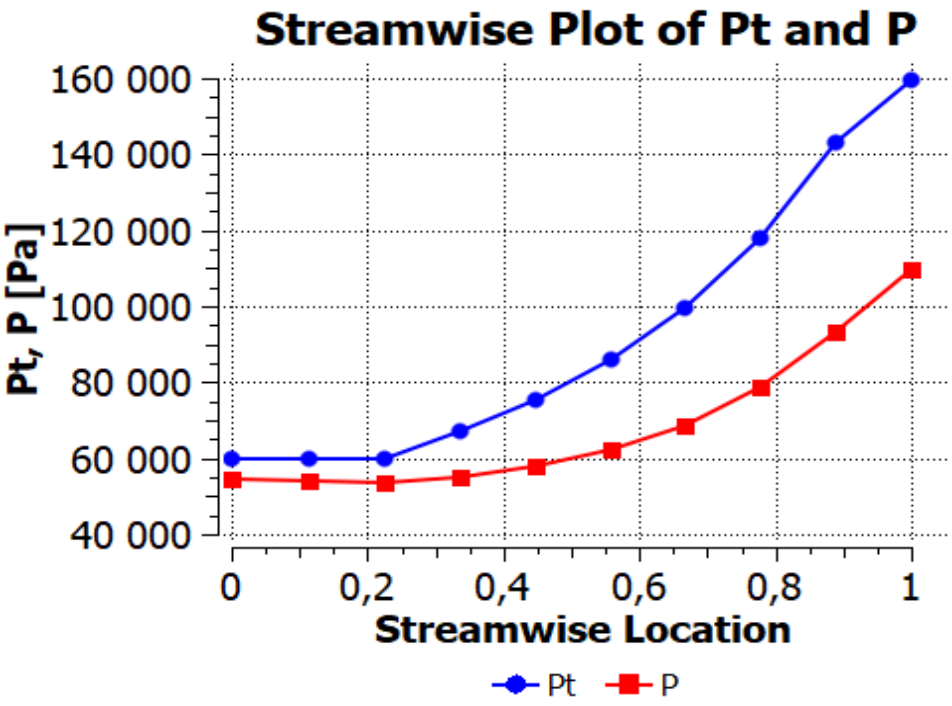

Figure 5.7: Total and static pressure variation curve in the compressor impeller.

Static temperature:

This figure shows the variation in static temperature on the compressor blade.

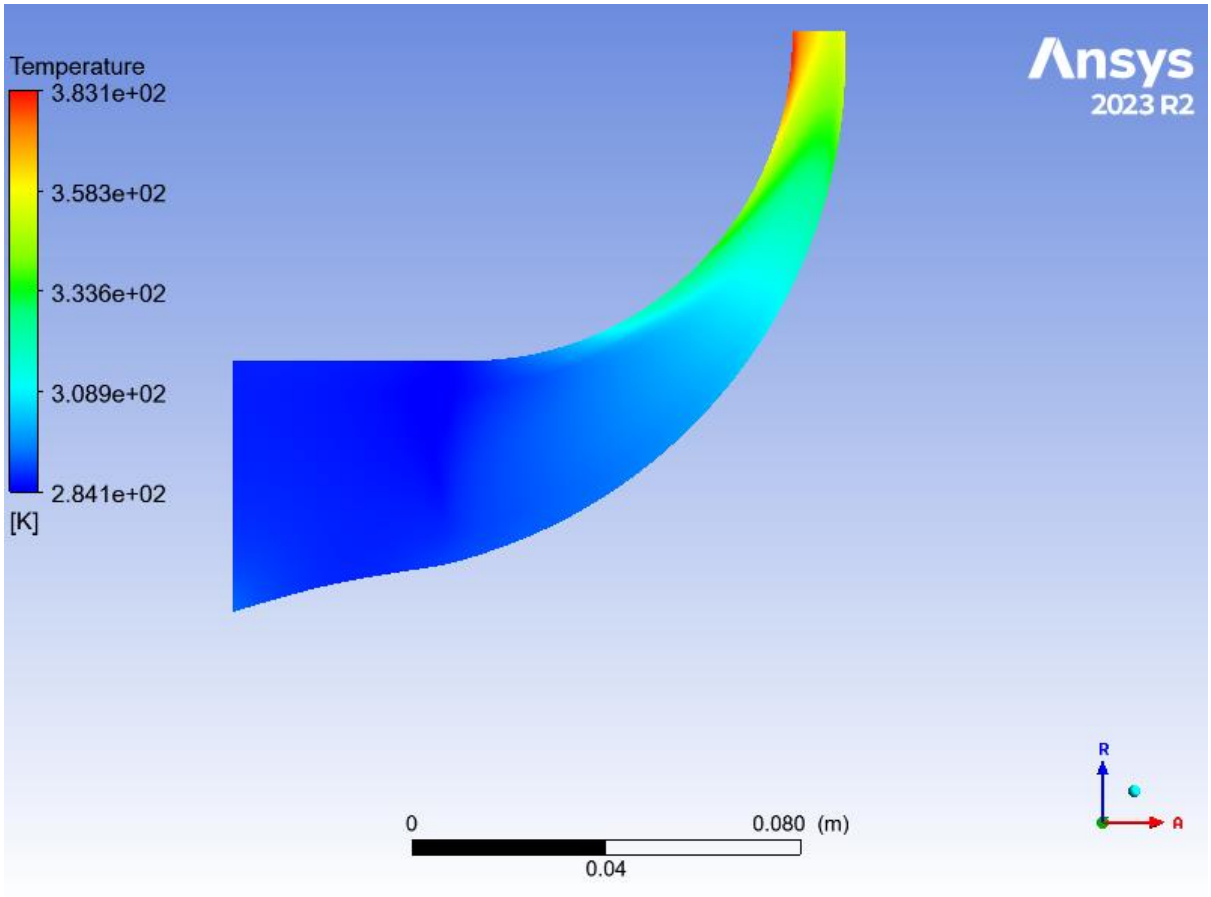

Figure 5.8: Static temperature distribution in the meridian plane.

Figure showing the variation in static temperature in the meridian plane for a corrected flow of 2.1 kg/s and a velocity of 28541 rpm.

Total temperature:

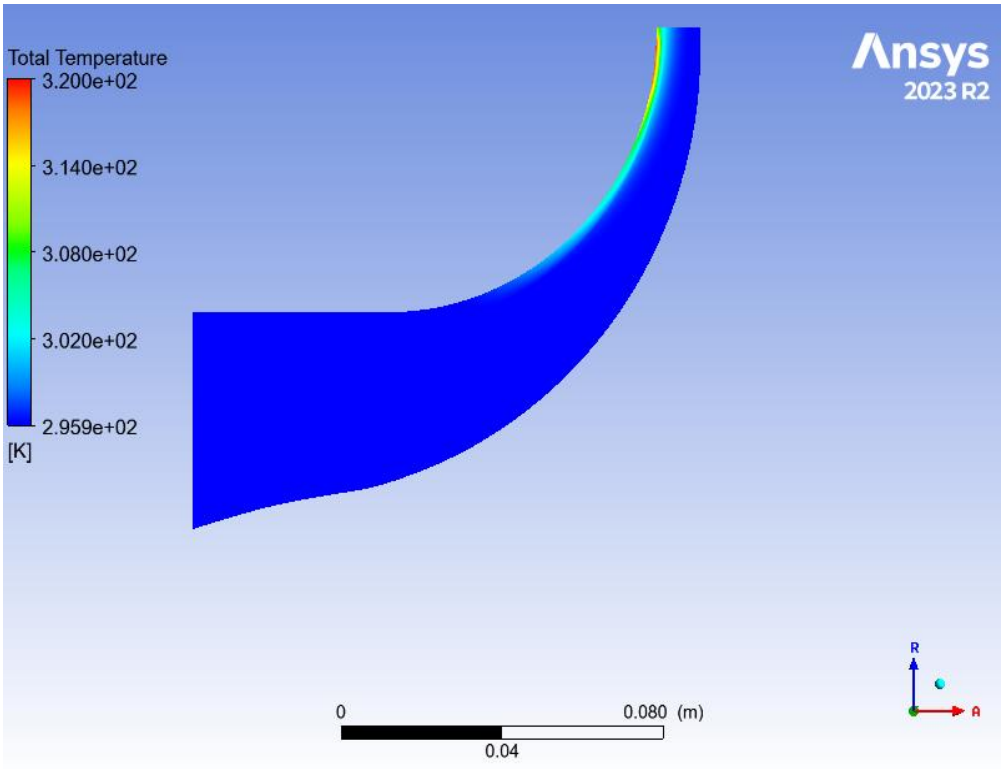

Figure 5.9: Total temperature distribution in the meridian plane.

Figure showing the variation in total temperature in the meridian plane for a corrected flow of 2.1 kg/s and a velocity of 28541 rpm.

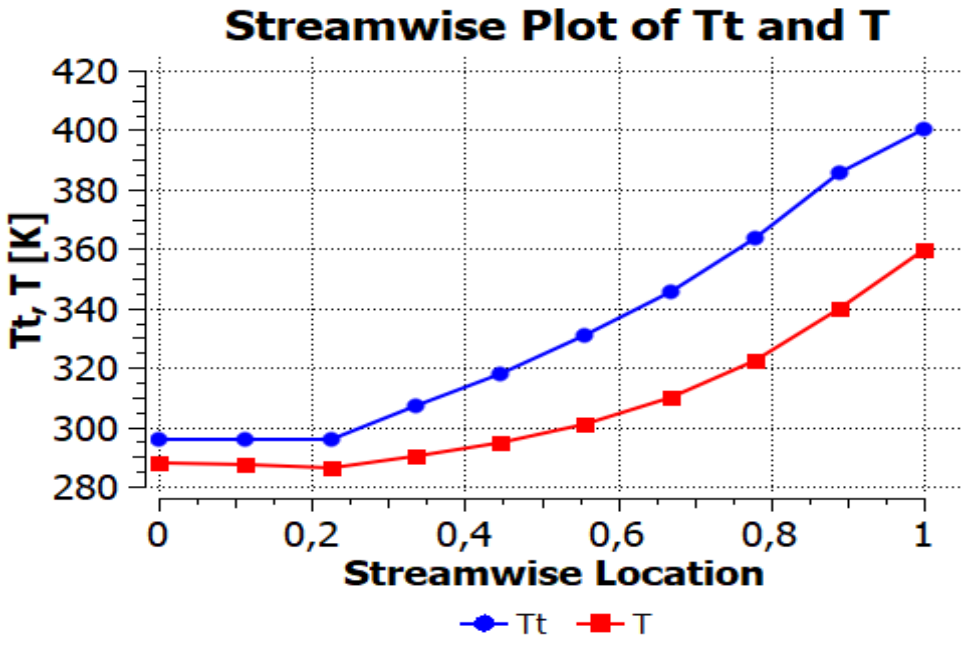

Figure 5.10: Total and static temperature variation curve In the compressor impeller.

Number of Mach:

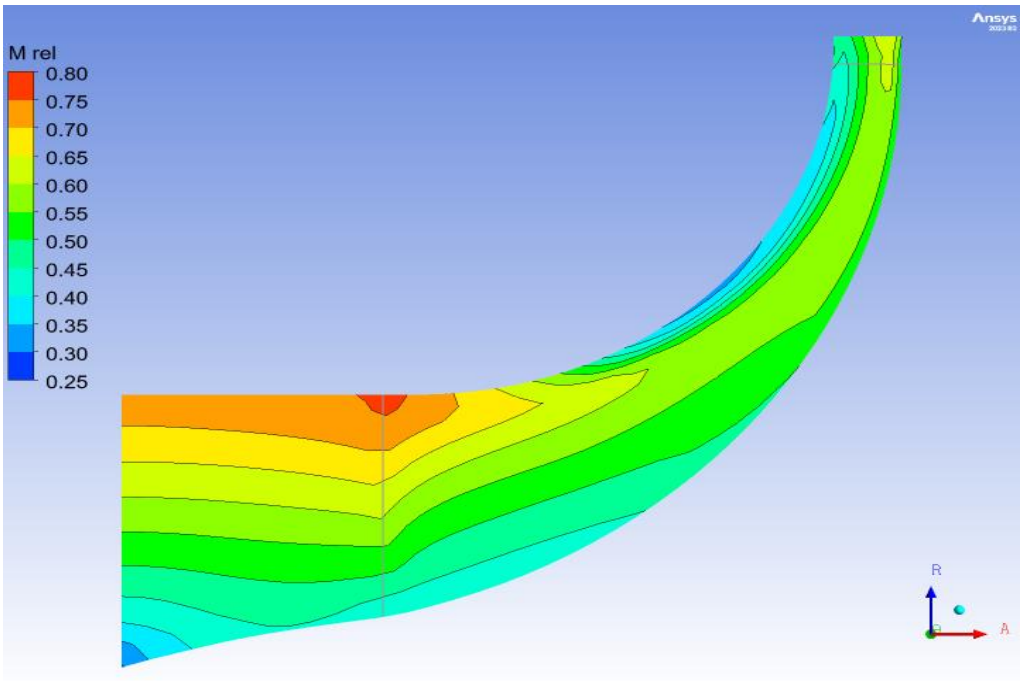

Figure 5.11: Distribution of Mach numbers in the meridian plane.

Figure showing the variation in Mach number in the meridian plane for a corrected flow of 2.1kg/s and a velocity of 28541 rpm.

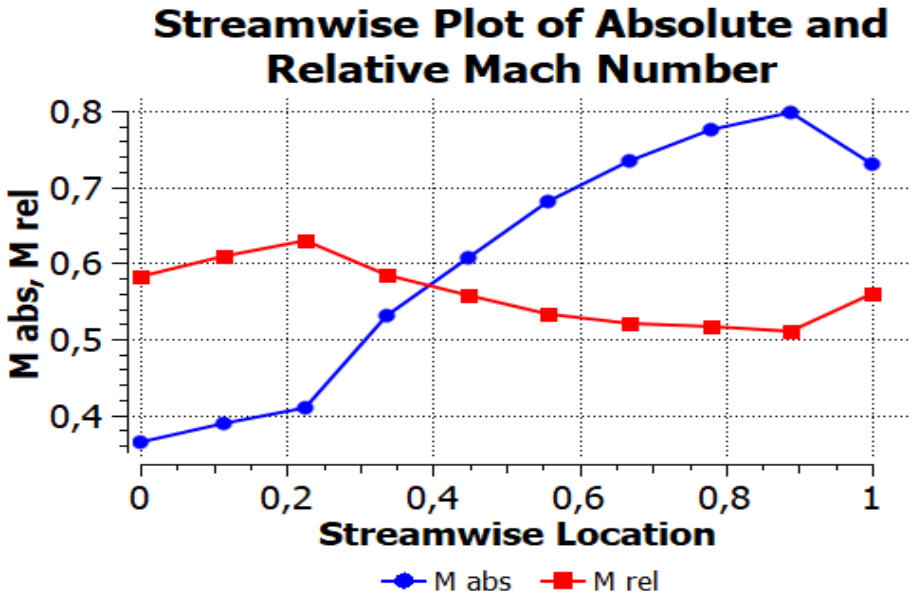

Figure 5.12: Curve of relative and absolute Mach number variation in the compressor impeller .

Velocity:

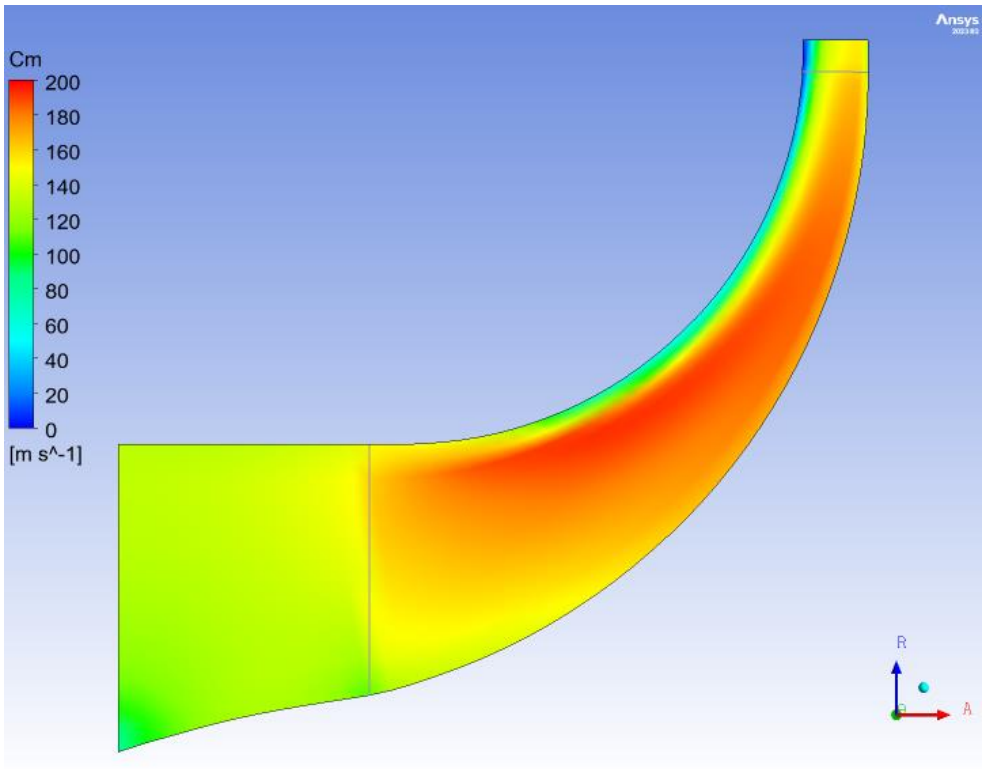

Figure 5.13: Velocity coefficient Cm distribution in the meridian plane.

Variation curve for Velocity coefficient Cm

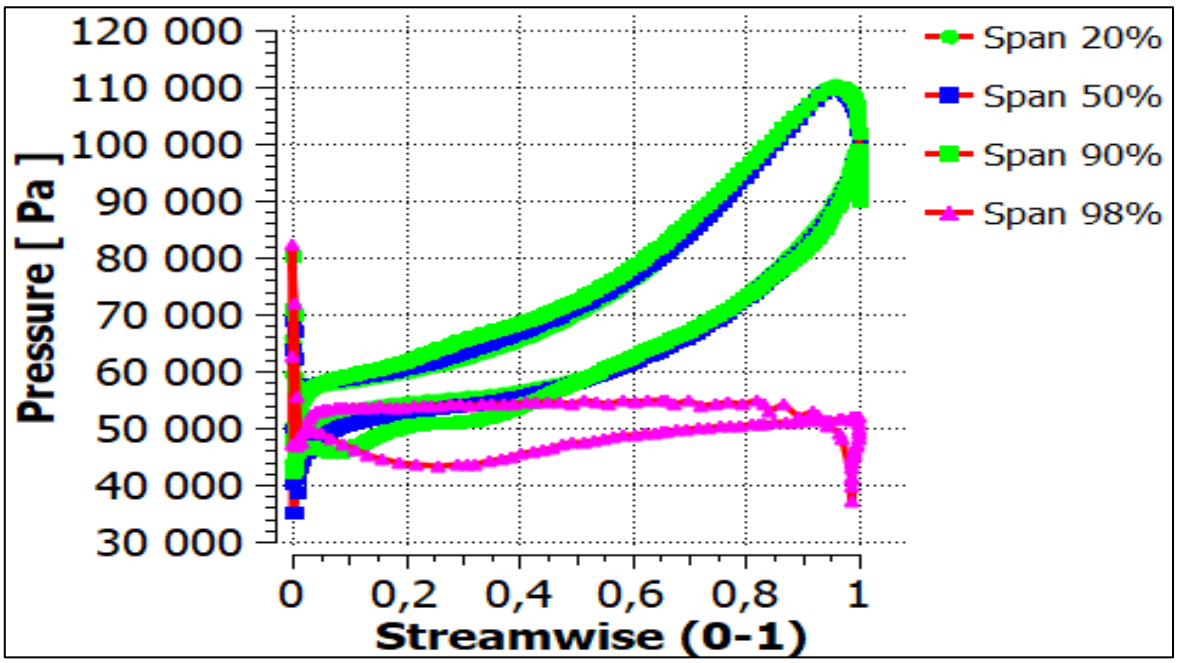

Figure 5.14: The load on the vane at 10%, 50%, 90% and 98% of Span.

Static entropy:

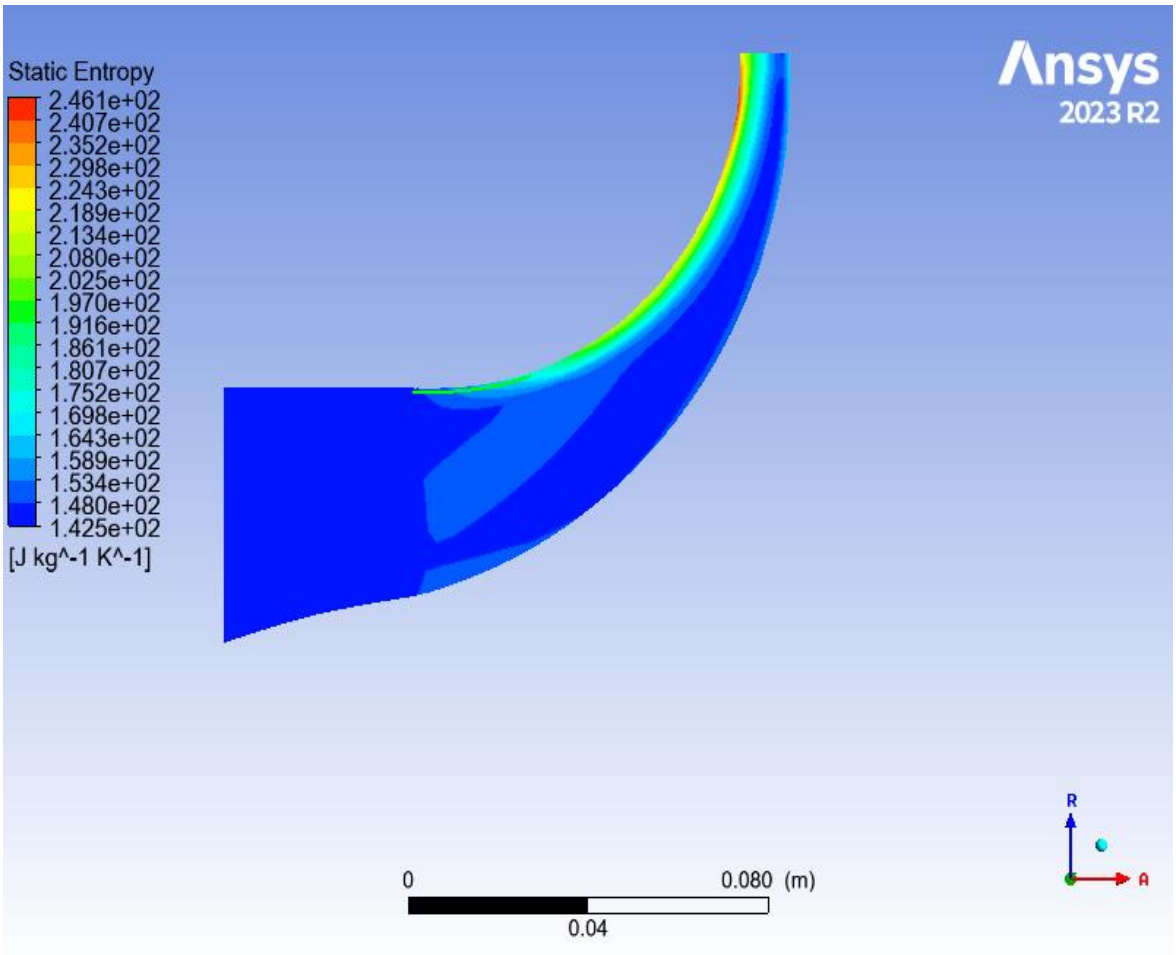

Figure 5.15: Static entropy distribution in the meridian plane.

Figure showing the variation in entropy in the meridian plane for a corrected flow of 2.1 kg/s and a velocity of 28541 rpm. Note the energy losses between the blades and the casing due to the secondary flow in the section where the clearance exists.

5.5. Plan blade to blade

Static pressure:

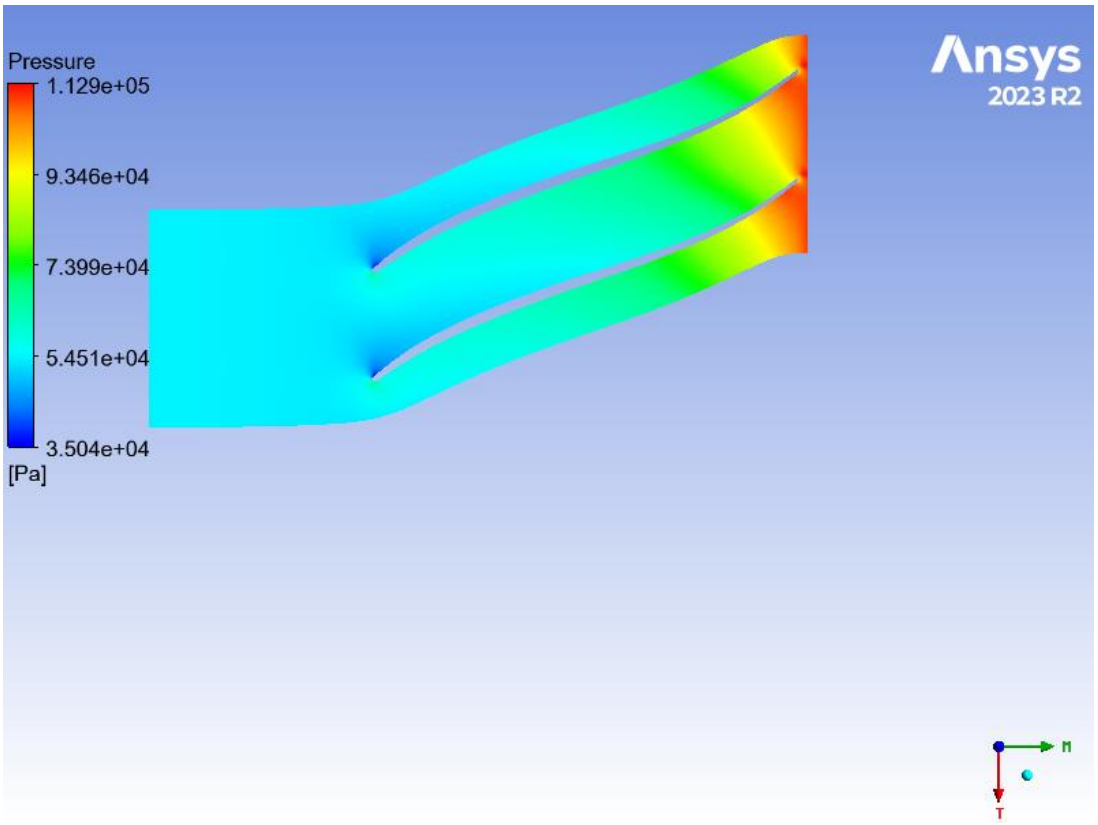

Figure 5.16: Static pressure distribution in the plan blade to blade.

The evolution of the isobars in the blade-to-blade plane reveals several phenomena:

1. **At the impeller inlet**: The Coriolis and centrifugal forces, which arise from the rotation of the impeller, are initially zero. The pressure gradient is consistently positive from the upper surface of one blade to the lower surface of the adjacent blade. This is primarily due to the effect of the centrifugal force resulting from the blade's curvature.

2. **At the impeller exit**: Three forces come into play: the inertial force of the particle, the centrifugal force due to the blade's curvature, and the Coriolis force. In this scenario, the centrifugal force due to the curvature is negligible because the radius is large. Consequently, the centrifugal force is always less than the Coriolis force. According to the simplified equilibrium equation in the blade-to-blade plane, the pressure gradient remains positive.

Total pressure

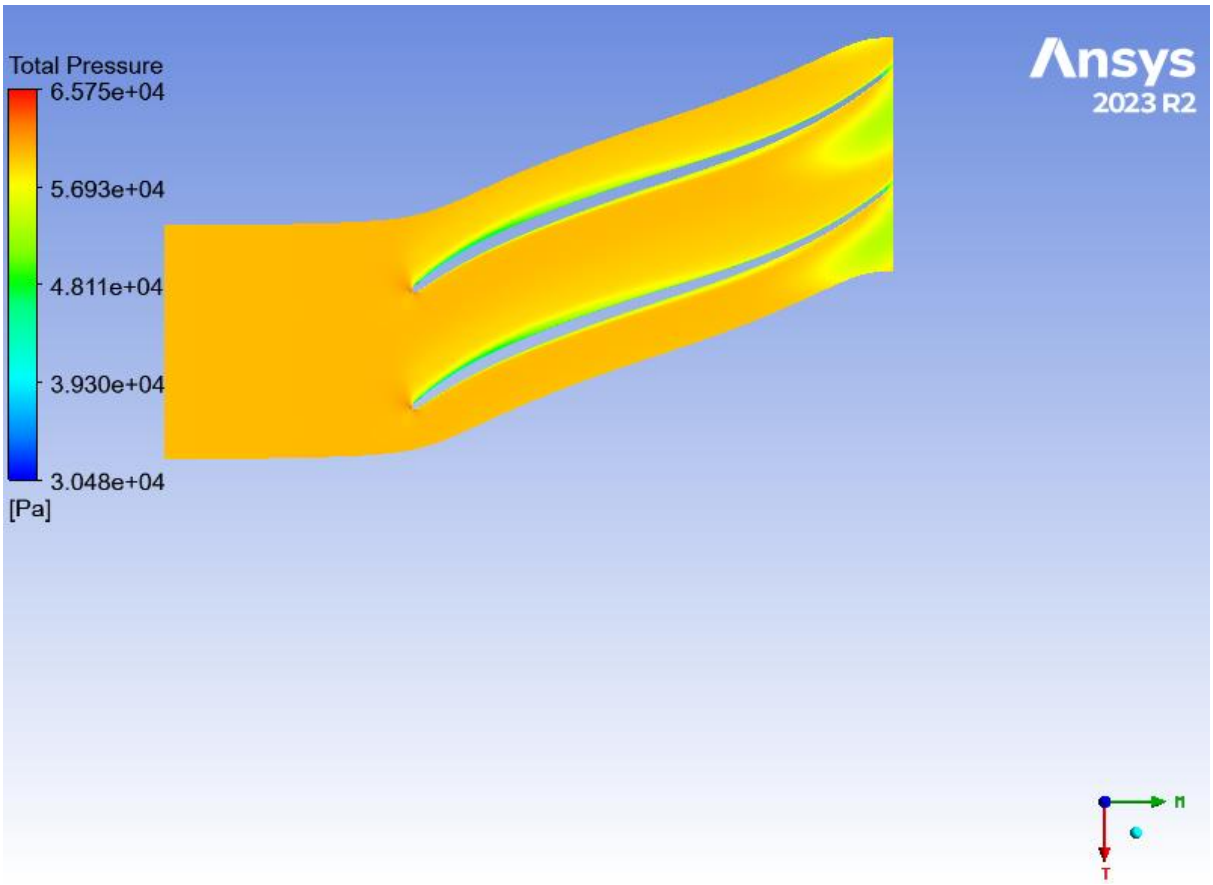

Figure 5.17: Total pressure distribution in the plan blade to blade.

At the impeller inlet, the gas undergoes compression and an increase in kinetic energy. As the gas moves through the impeller, the blades transfer rotational kinetic energy to it, which raises both its speed and pressure. The centrifugal force generated by the impeller's rotation results in a higher pressure at the impeller outlet compared to the inlet.

Velocity:

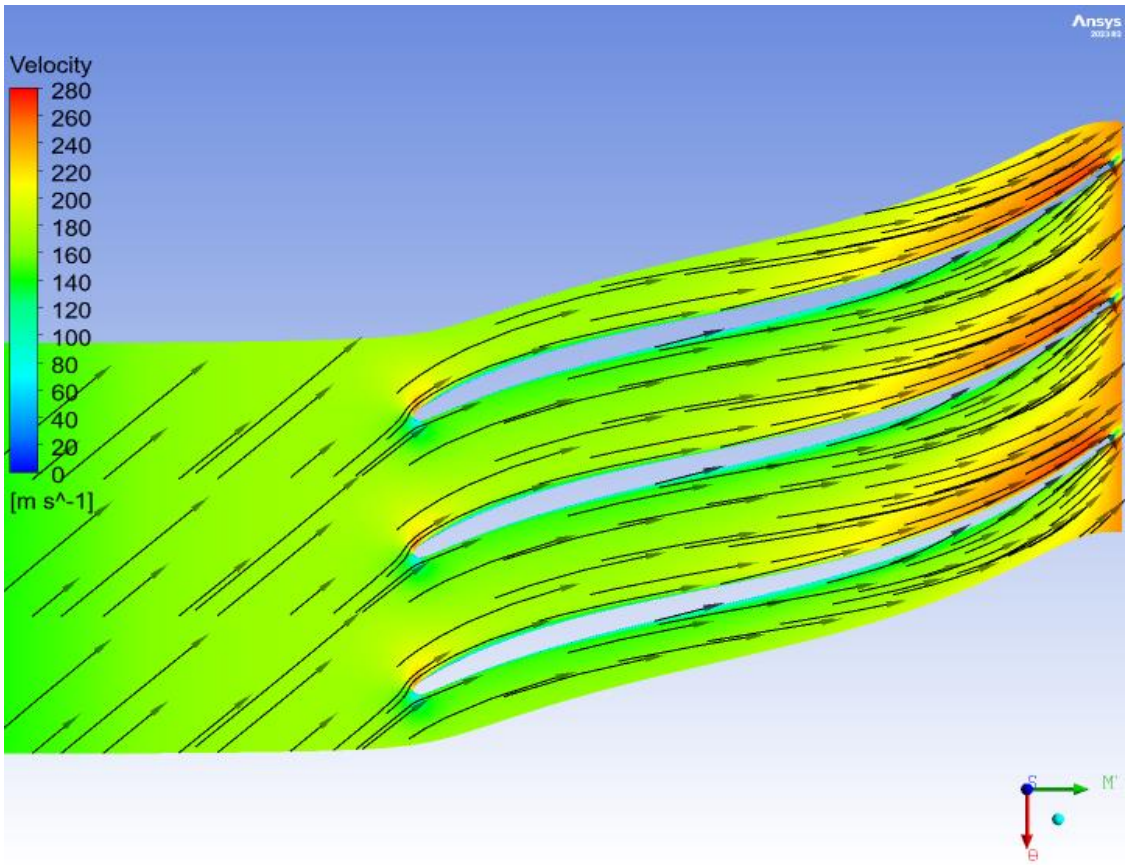

Figure 5.18: Velocity field distribution at 20% of blade height

In the blade-to-blade plane.

In general, the gas velocity increases from the inlet to the impeller due to the centrifugal force produced by the impeller's rotation. The impeller blades impart energy to the gas, boosting its speed and pressure. Consequently, the gas velocity at the impeller outlet is higher than at the inlet, owing to the centrifugal force generated by the rotating impeller.

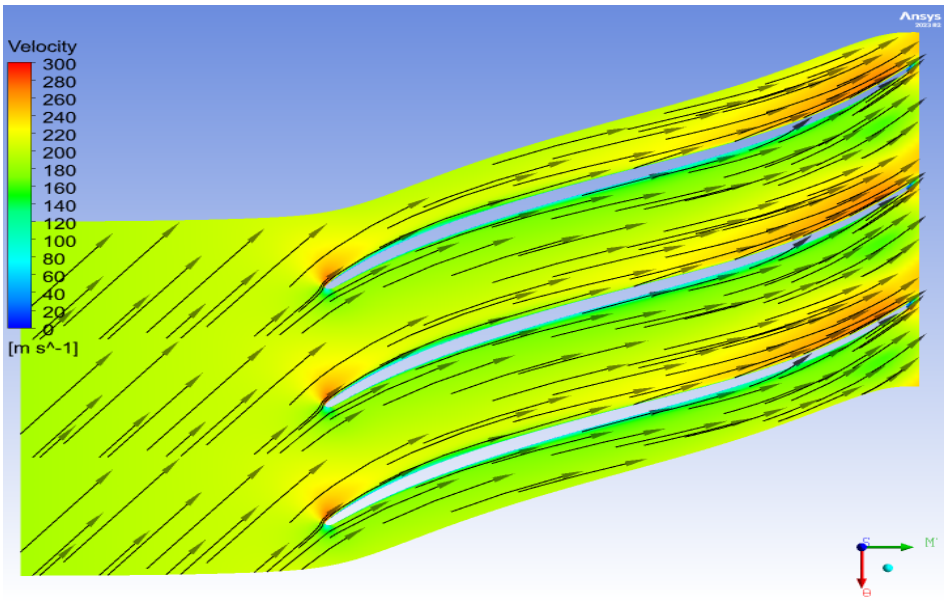

Figure 5.19: Velocity field distribution at 50% of blade height In the plan blade to blade.

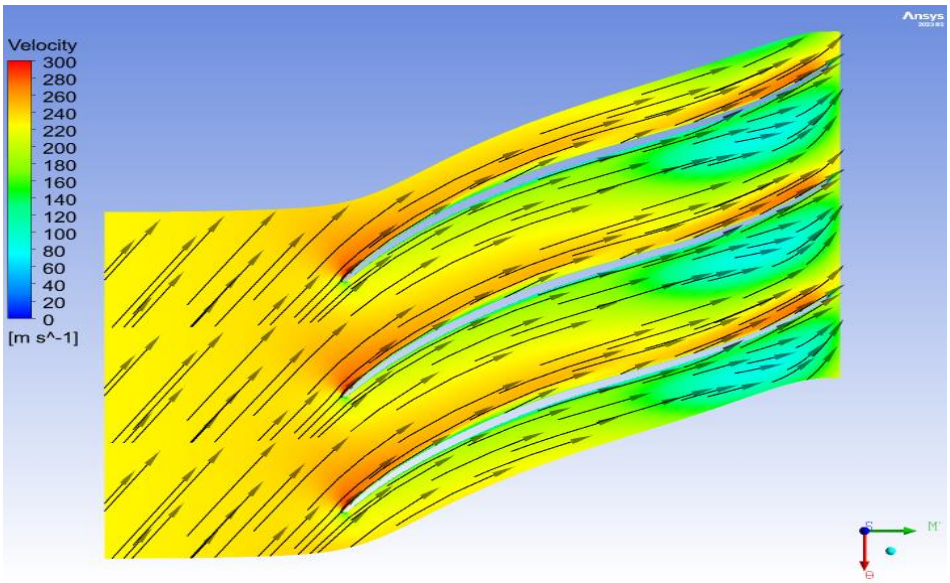

Figure 5.20: Velocity field distribution at 90% of blade height In the plan blade to blade.

The impact of blade clearance on airspeed is illustrated in this figure, highlighting how air leakage between the blade and the casing affects compressor stage performance. This air escape influences the overall efficiency and effectiveness of the compressor.

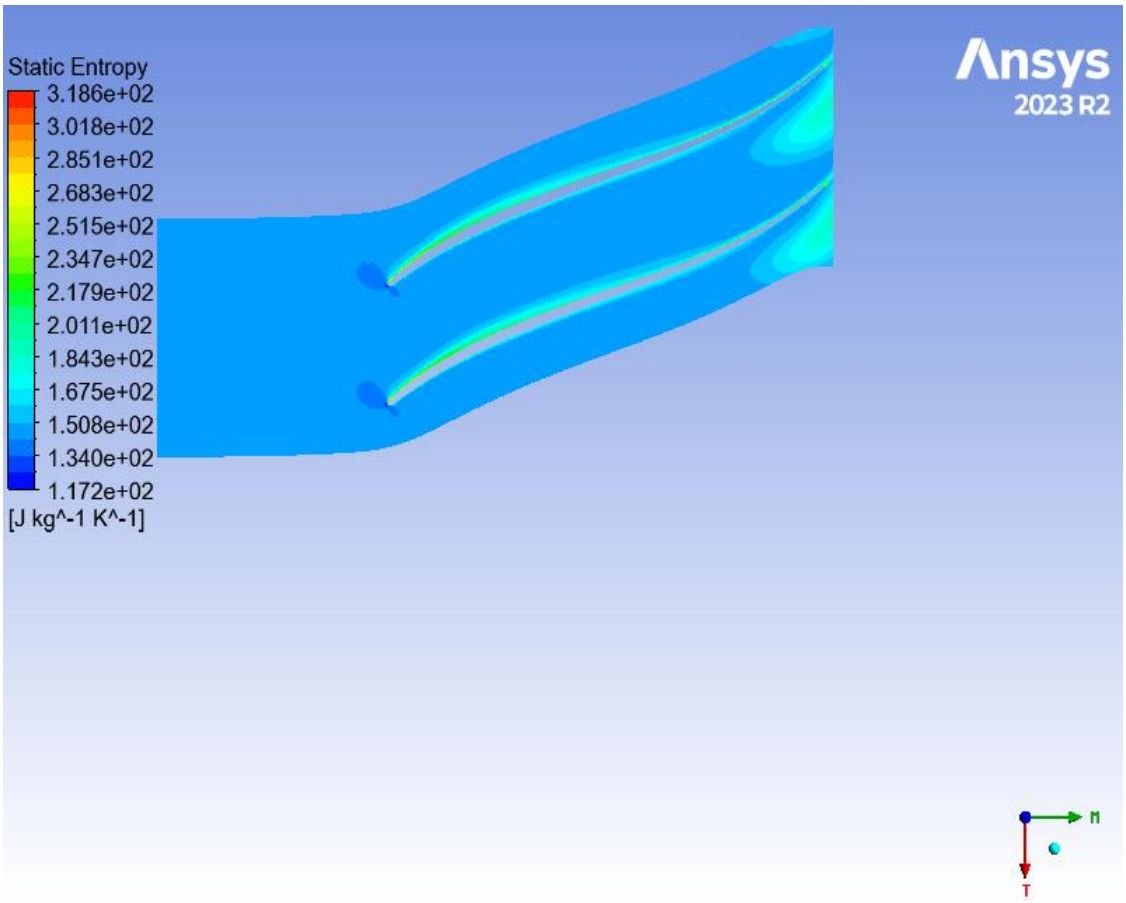

Figure 5.21: Static entropy distribution in the plan blade to blade.

5.6. Orthogonal plane :

Plans are established along the axis of the compressor blade to visualize the entropy variations, the development, and the point of wake formation behind the compressor blade. Additionally, these plans help observe the flow detachment on the surface perpendicular to the blade chord. These plans are organized as follows :

the positions of orthogonal planes:

plan	Positions according to the blade line
1	20%
2	45%
3	70%
4	98%

The Mach number variation fields according to the display plane are as follows:

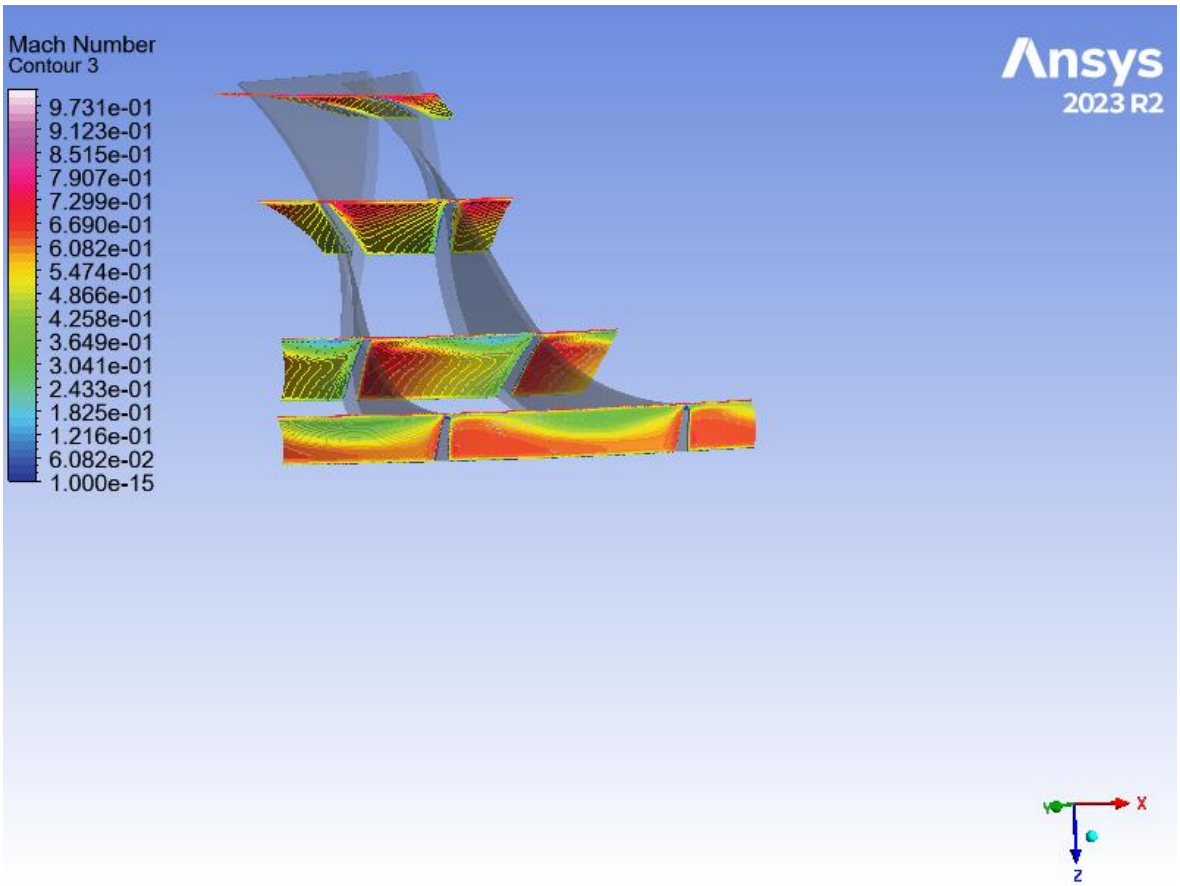

Figure 5.22: Mach number distribution in the orthogonal plane.

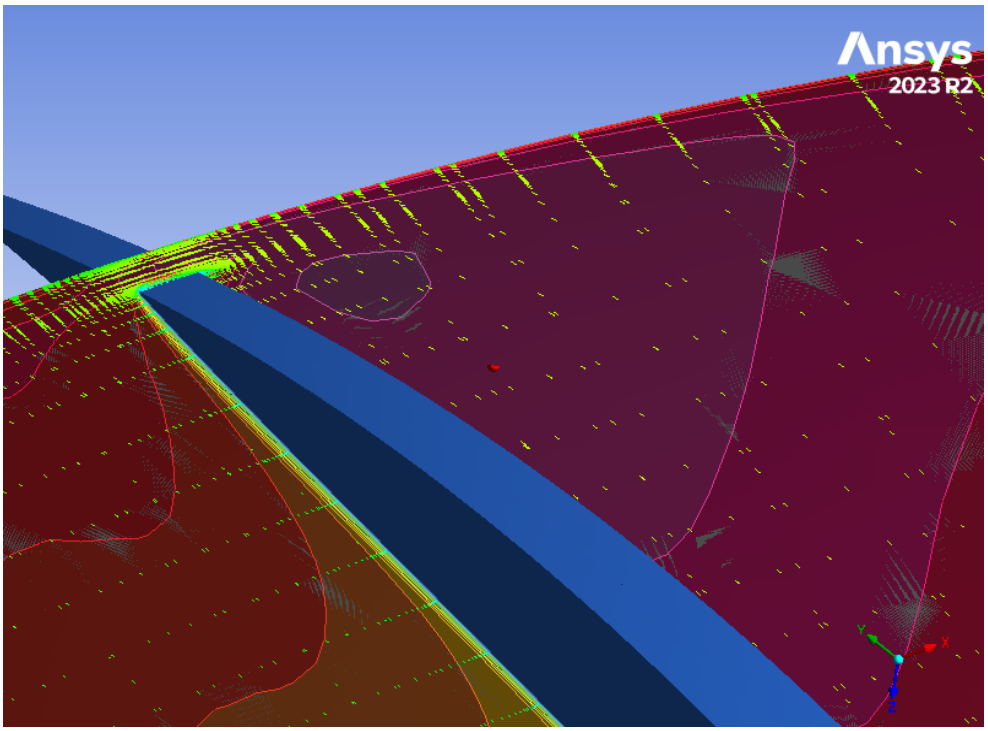

Figure 5.23: Mach number distribution at position 20% of the blade line in the orthogonal plane.

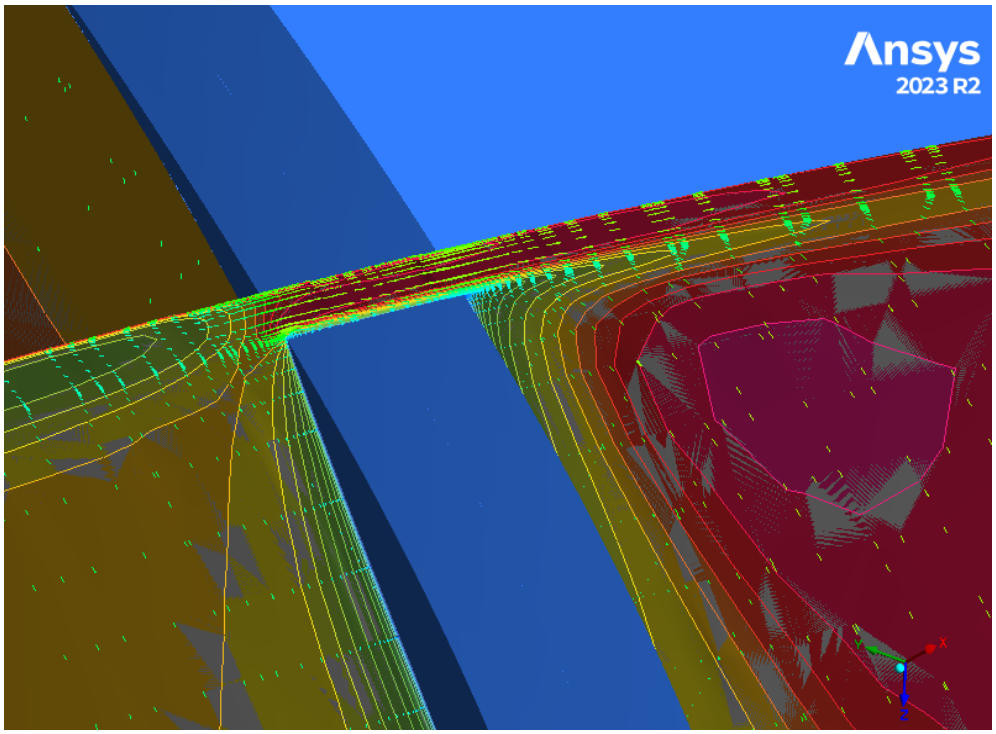

Figure 5.24: Mach number distribution at position 45% of the blade line in the orthogonal plane.

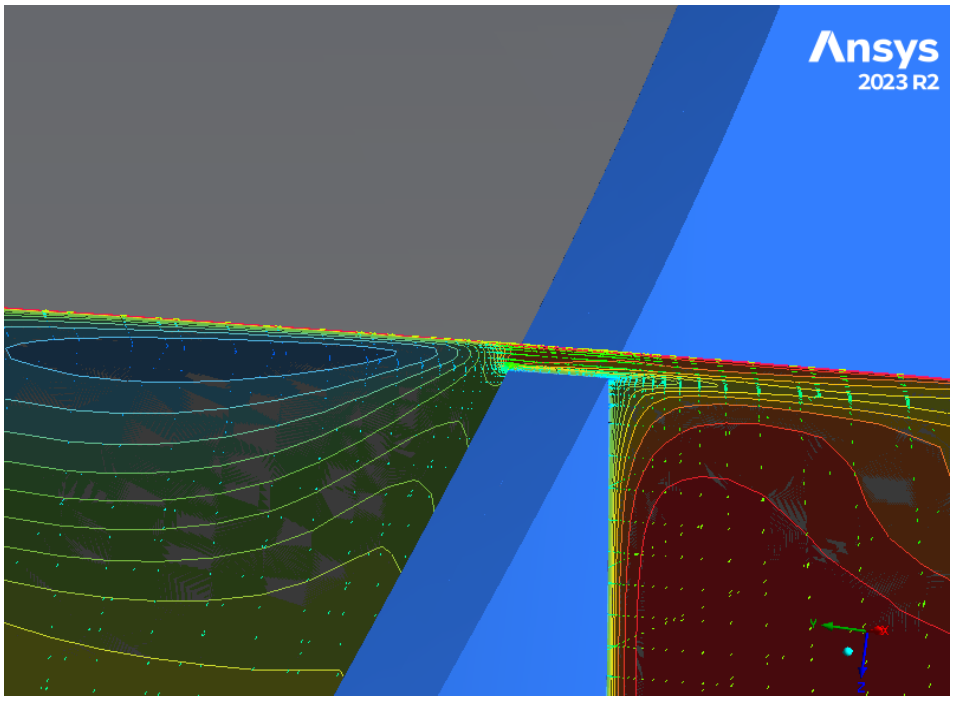

Figure 5.25: Mach number distribution at position 70% of the blade line in the orthogonal plane.

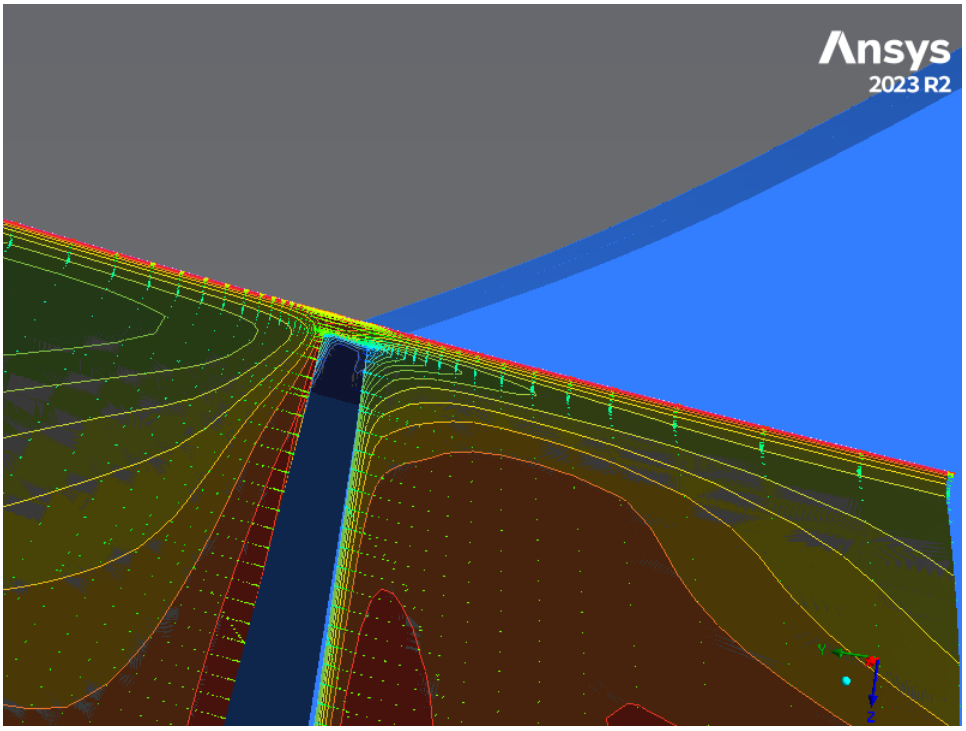

Figure 5.26: Mach number distribution at position 98% of the blade line in the orthogonal plane.

In these figures, it is evident that the size of the turbulence increases along the axis of the compressor blade. This can be explained by the airflow passing between the rotor blade and the

casing, causing the wake to become increasingly aggressive as we move further from the stage entrance. Additionally, the increase in centrifugal force due to the rotational speed plays a significant role in this behavior.

5.7. Results of multi-objective optimization

After many simulations and days of continuous calculations, we finally have to observe the results of the optimization performed as well as their results as shown in the following screenshots:

Table 5-1: The results of multi-objective.

Table of Outline A2: Design Points of Design of Experiments

	A	B	C	D	E	F	G	H
1	Name	P1 - SHROUD TIP Tip Clearance At Leading Edge (mm)	P2 - SHROUD TIP Tip Clearance At Trailing Edge (mm)	P3 - Flow Analysis 1 Maximum Number of Iterations	P4 - PRimpeller	P5 - TR	P6 - efficiency	P7 - mCorige (kg s^-1)
2	1 DP 5	0,47	0,47	800	2,655	1,3516	0,91525	2,0844
3	2 DP 2	0,24	0,47	800	2,6593	1,351	0,91856	2,1112
4	3 DP 8	0,7	0,47	800	2,651	1,3518	0,91295	2,0575
5	4 DP 4	0,47	0,24	800	2,6591	1,3521	0,91563	2,1486
6	5 DP 6	0,47	0,7	800	2,6453	1,3511	0,91263	2,0158
7	6 DP 1	0,24	0,24	800	2,6629	1,3512	0,91931	2,1799
8	7 DP 7	0,7	0,24	800	2,6555	1,3533	0,91085	2,1137
9	8 DP 3	0,24	0,7	800	2,6495	1,3501	0,91674	2,0467
10	9 DP 9	0,7	0,7	800	2,642	1,3527	0,90708	1,9825

Table 5-2:The results of multi-objective optimization.

Table of Schematic D4: Optimization

	A	B	C	D	E	F	G
1	Optimization Study						
2	Maximize P4	Goal, Maximize P4 (Default importance)					
3	Maximize P6	Goal, Maximize P6 (Default importance)					
4	Optimization Method						
5	MOGA	The MOGA method (Multi-Objective Genetic Algorithm) is a variant of the popular NSGA-II (Non-dominated Sorted Genetic Algorithm-II) based on controlled elitism concepts. It supports multiple objectives and constraints and aims at finding the global optimum.					
6	Configuration	Generate 100 samples initially, 100 samples per iteration and find 3 candidates in a maximum of 20 iterations.					
7	Status	Converged after 9 evaluations, because all permutations have been evaluated.					
8	Candidate Points						
9		Point candidat 1	Point candidat 1 (verified) DP 1	Point candidat 2	Point candidat 2 (verified) DP 10	Point candidat 3	Point candidat 3 (verified) DP 3
10	P1 - SHROUD TIP Tip Clearance At Leading Edge (mm)	0,24		0,24		0,24	
11	P2 - SHROUD TIP Tip Clearance At Trailing Edge (mm)	0,24		0,48		0,7	
12	P3 - Flow Analysis 1 Maximum Number of Iterations	800		800		800	
13	P4 - PRimpeller	2,6629	2,6629	2,659	2,6591	2,6495	2,6495
14	P6 - efficiency	0,9193	0,91931	0,91851	0,91861	0,91673	0,91674

In the context of multi-optimization, a trade-off diagram shows the trade-offs that need to be made between the different design variables to obtain the best overall solution. The screenshot

below shows the comprise diagram for our optimization in a 3D view (shroud tip clearance at leading edge, shroud tip clearance at trailing edge, Pressure ratio impeller)

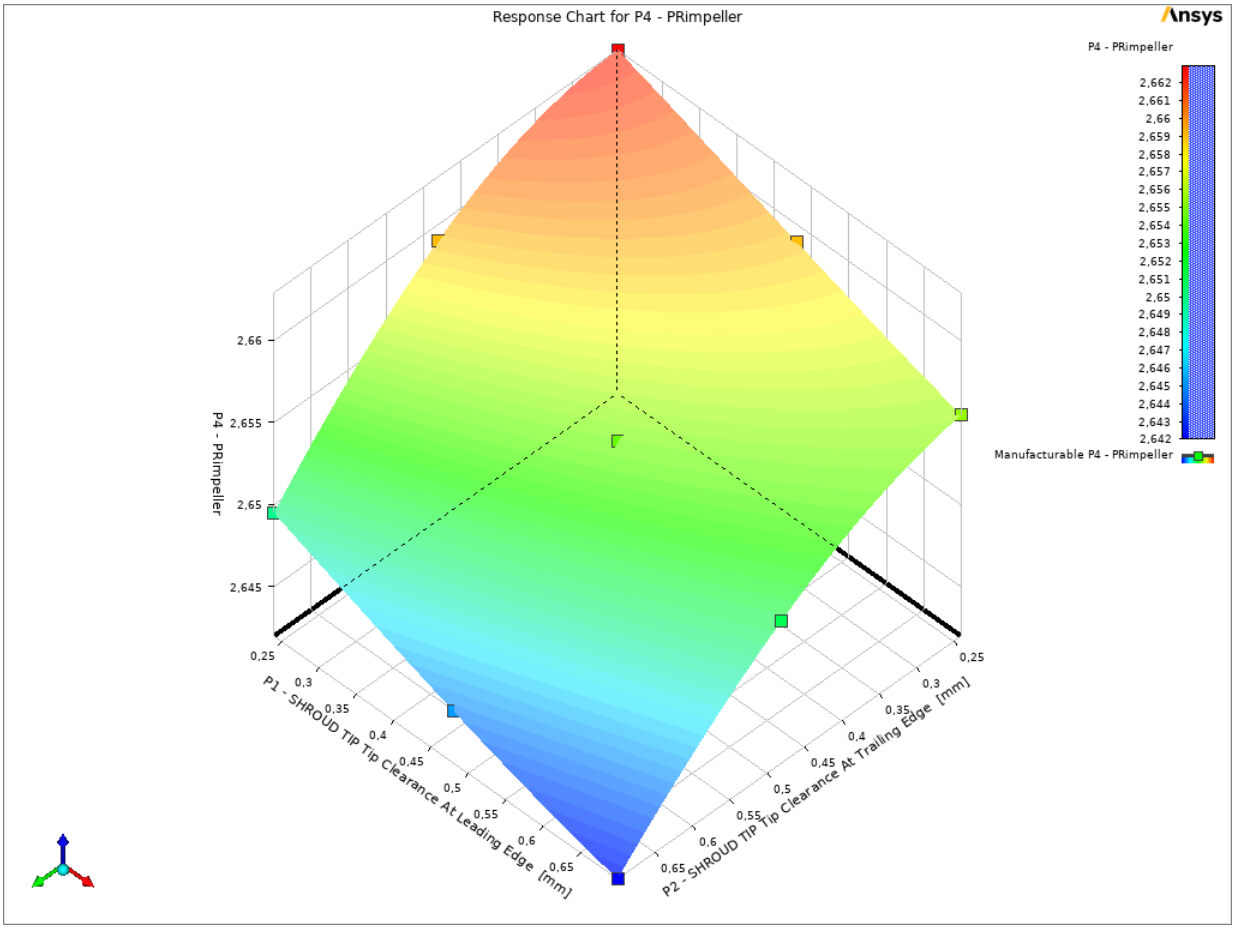

Figure 5.27:Diagram representing optimization in a view 3D(shroud tip clearance at leading edge, shroud tip clearance at trailing edge, Pressure ratio impeller).

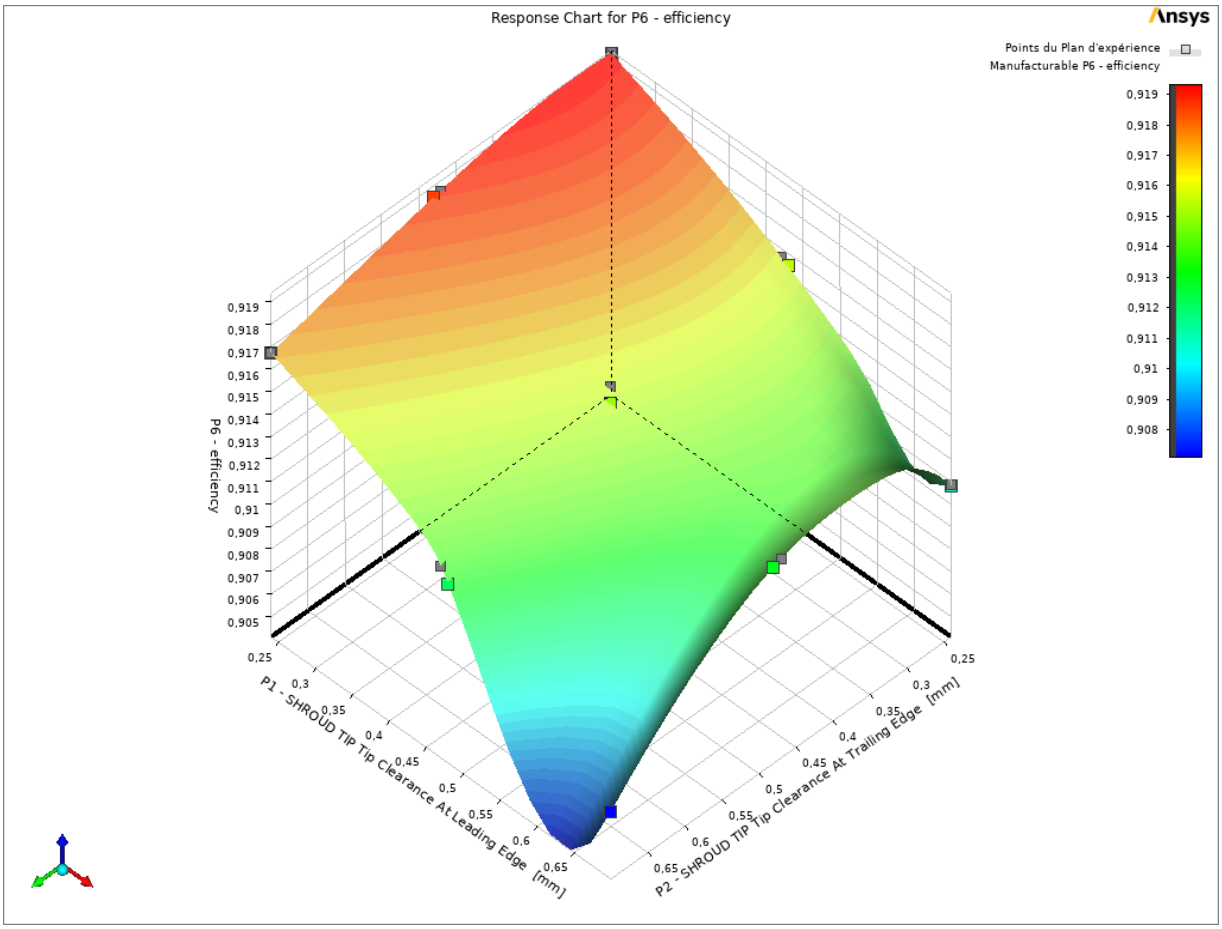

Figure 5.28: Diagram representing optimization in a view 3D(shroud tip clearance at leading edge, shroud tip clearance at trailing edge, Efficiency).

Having defined the optimum design point based on multi-objective optimization, we will use this value to run a simulation in CFX and evaluate the compressor's performance for the specified impeller clearance value of TE=LE=0.24. Here are the results obtained from this simulation.

Optimization multi-objectives

We analyze the results and performance of our compressor stage by varying the impeller-shroud clearance as part of a multi-objective optimization. The goal of this trial is to compare performance metrics to determine the optimal clearance position and understand the impact of clearance on the efficiency and compression ratio of the compressor. The results presented are

based on simulations conducted with consistent mass flow rate, rotation speed, and mesh parameters.

Table 5-3: Compressor performance results for the clearance LE=0.24 ; TE=0.24

Rotation Speed	2988.8100	[radian s^-1]
Mass Flow Rate	1.2739	[kg s^-1]
Inlet Volume Flow Rate	1.8041	[m^3 s^-1]
Input Power	133256.0000	[W]
Reference Radius	0.1348	[m]
Inlet Flow Coefficient	0.0617	
Exit Flow Coefficient	0.3412	
Head Coefficient	3.6603	
Work Input Coefficient	0.6449	
Total Pressure Ratio	2.6661	
Total Temperature Ratio	1.3518	
Total Isentropic Efficiency %	92.4064	
Total Polytropic Efficiency %	93.3656	

Table 5-4: Compressor performance results for the clearance LE=TE=0

Rotation Speed	2988.8100	[radian s^-1]
Mass Flow Rate	1.2028	[kg s^-1]
Inlet Volume Flow Rate	1.7035	[m^3 s^-1]
Input Power	125276.0000	[W]
Reference Radius	0.1348	[m]
Inlet Flow Coefficient	0.0582	
Exit Flow Coefficient	0.3236	
Head Coefficient	3.6233	
Work Input Coefficient	0.6421	
Total Pressure Ratio	2.6438	
Total Temperature Ratio	1.3503	
Total Isentropic Efficiency %	91.8874	
Total Polytropic Efficiency %	92.9258	

Table 5-5: Compressor performance results for the clearance LE=0,684 ;TE=0,358 (exp).

Rotation Speed	2988.8100	[radian s^-1]
Mass Flow Rate	1.2308	[kg s^-1]
Inlet Volume Flow Rate	1.7433	[m^3 s^-1]
Input Power	128828.0000	[W]
Reference Radius	0.1348	[m]
Inlet Flow Coefficient	0.0596	
Exit Flow Coefficient	0.3317	
Head Coefficient	3.6550	
Work Input Coefficient	0.6453	
Total Pressure Ratio	2.6634	
Total Temperature Ratio	1.3521	
Total Isentropic Efficiency %	92.3252	
Total Polytropic Efficiency %	93.3003	

To better understand these values, here is the static entropy variation field for the three cases, these figures represent the static entropy field at the position of 98% of the height of the blade in the blade-to-blade plane and in the meridian plane.

Display in the plan blade to blade :

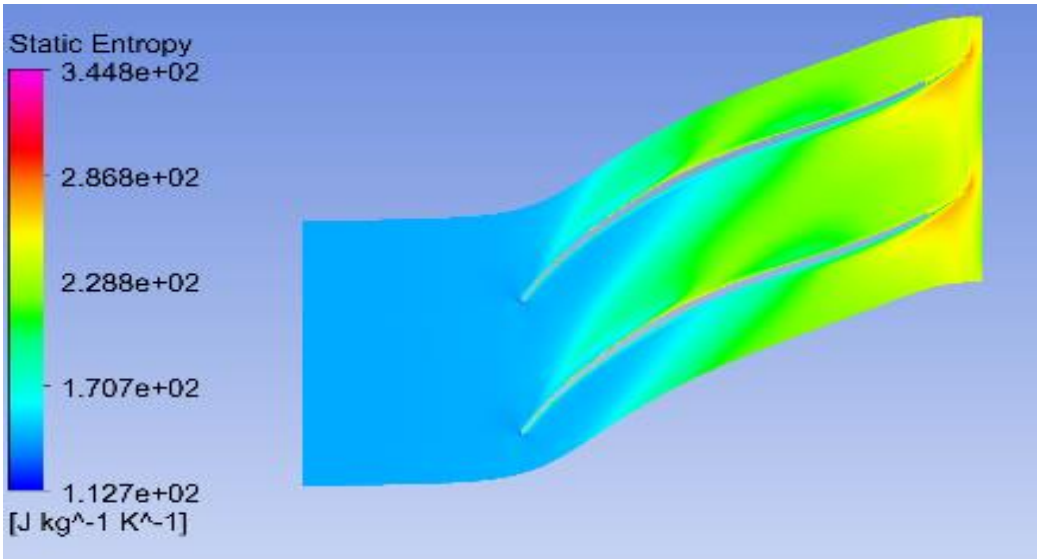

Figure 5.29: Field distribution of static entropy variation at clearances LE=TE=0.24 in the plan blade to blade.

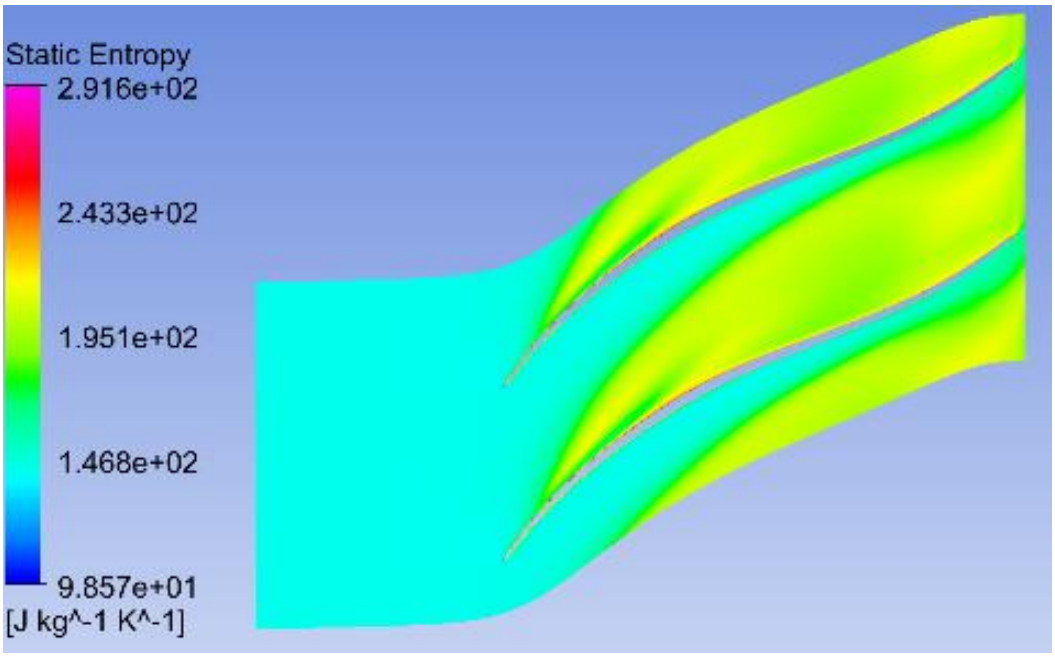

Figure 5.30: Field distribution of static entropy variation at clearances LE=TE=0 in the plan blade to blade.

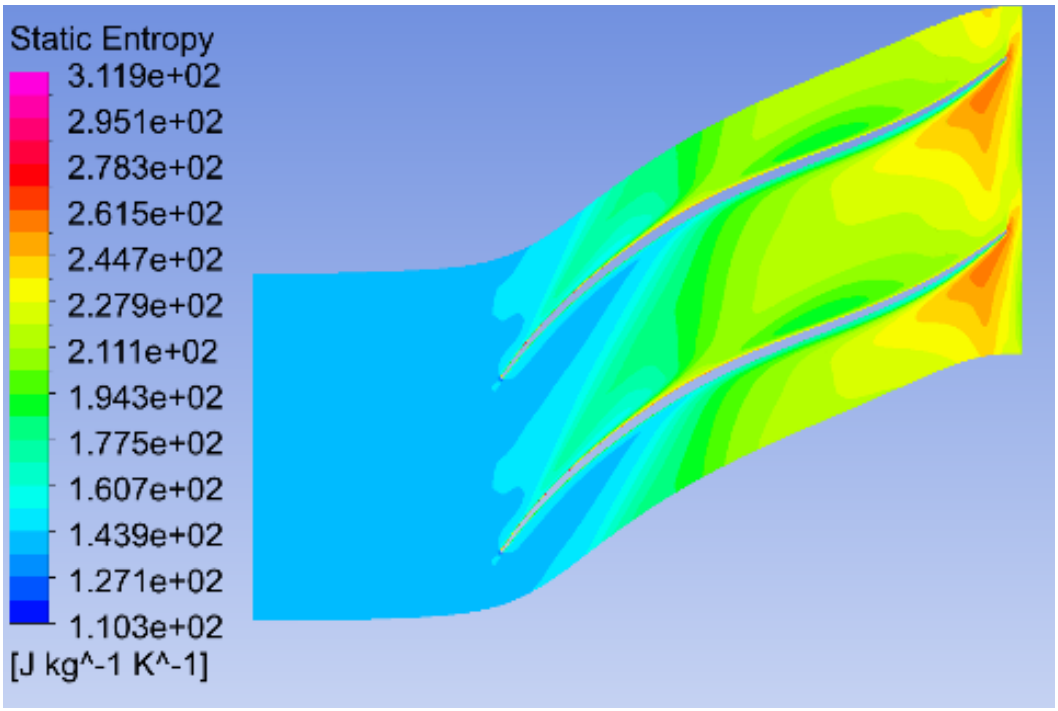

Figure 5.31: Field distribution of static entropy variation at clearances (LE=0,684; TE=0,358) (exp) in the plan blade to blade.

After the 3 figures the largest static entropy zone (the losses) in the case clearance LE=LT=0 Due to the creation of the recirculation and boundary layer decollement zones on the SS part and the circulation zones in the trailing edge.

Display in meridian plane:

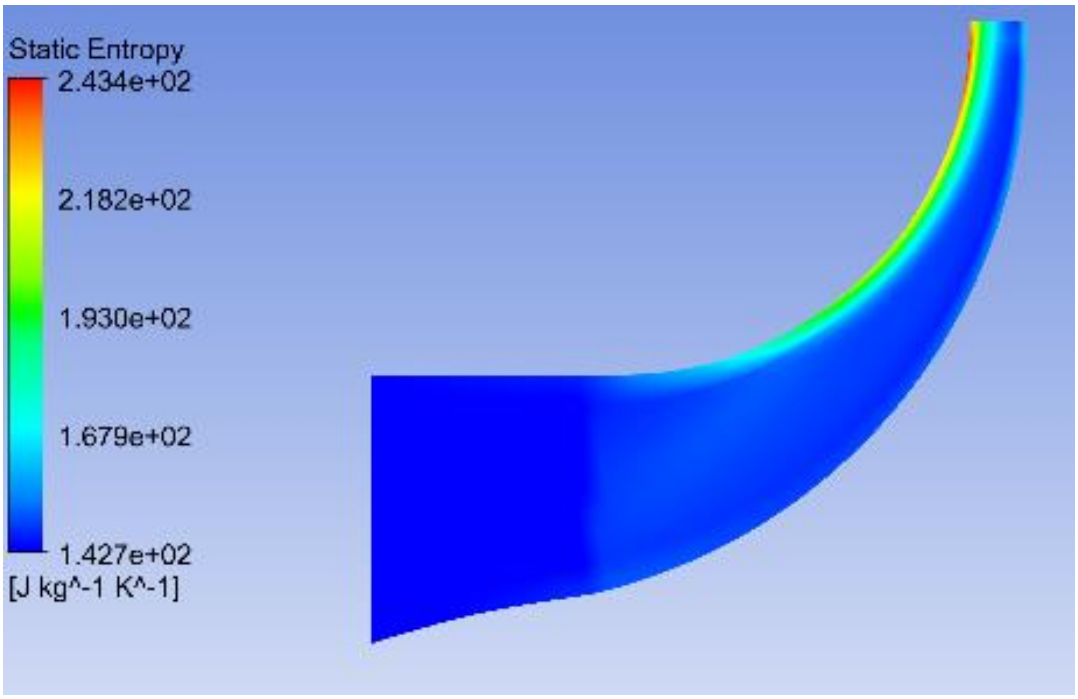

Figure 5.32: Field distribution of static entropy variation at clearances (LE=TE=0,24) in the plan meridian.

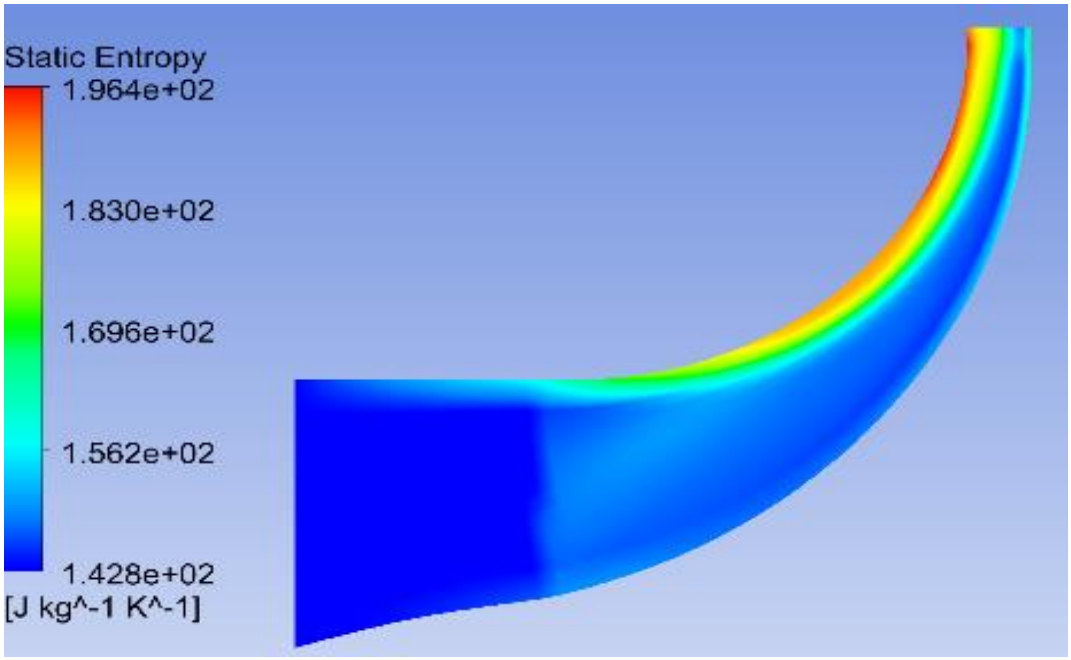

Figure 5.33: Field distribution of static entropy variation at clearances (LE=TE=0) in the plan meridian.

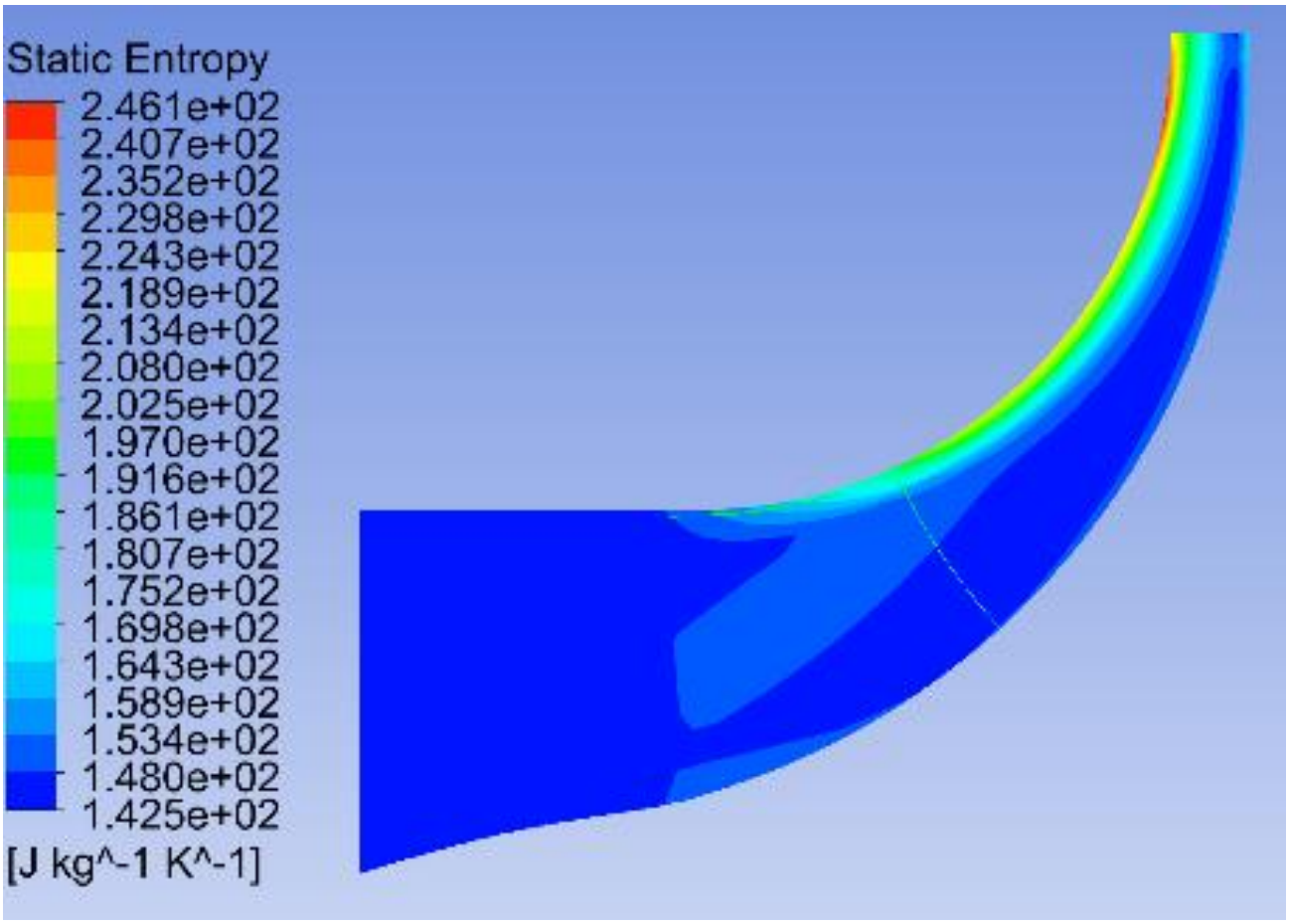

Figure 5.34: Field distribution of static entropy variation at clearances (LE=0,684; TE=0,358) (exp) in the plan meridian.

From these figures, we can see that the static entropy increases in parallel with the increase in tip clearance. This can be explained by the friction losses in the interaction between the main flow and the secondary flow, so for more clearance, there is more energy loss, and consequently lower performance.

5.8. The Impact of Clearance on Noise Generation

Aeroacoustics, which focuses on the study of aerodynamic noise in the air, is a branch of fluid mechanics. It examines how the characteristics of fluid flow produce acoustic radiation. This field is characterized by low amplitude, propagative compressible fluctuations, positioning aeroacoustics at the intersection of acoustics and fluid mechanics.

When an object moves slowly through a fluid, the fluid flows smoothly around it. However, rapid movement of the object causes a local displacement of the fluid, resulting in changes in density and pressure. For instance, a moving loudspeaker membrane compresses the adjacent air layer, creating an unstable situation where pressure forces act to restore equilibrium. This pressure difference causes the neighboring air layers to move and compress successively.

This process leads to wave propagation through a series of compressions and expansions. However, this description is incomplete without considering the movement of molecules from areas of higher concentration to areas of lower concentration to balance density differences.

For sound to propagate, the regions with altered pressure and density must be significantly larger than the mean free path of the molecules. This requirement leads to defining a fluid particle as a volume large enough to contain a vast number of molecules, yet small enough to ensure that acoustic variables such as displacement, speed, overpressure, and overdensity remain constant.

Noise sources can be classified into 3 types:

- Monopole Source:

- A monopole source radiates sound uniformly in all directions from a single point.
- It represents a simple oscillating source, such as a pulsating sphere, where the volume of the fluid increases and decreases uniformly.
- Monopole sources are characterized by their ability to create sound waves through volumetric changes without directional dependence.
- Example: A small loudspeaker emitting sound.

- **Dipole Source**:

- A dipole source consists of two closely spaced monopole sources of equal strength but opposite phase.
- It creates a figure-eight radiation pattern, with sound waves propagating more strongly in two opposite directions and weakly in the perpendicular directions.
- Dipole sources arise from oscillating forces, such as vibrating panels or wings flapping.
- Example: The noise produced by the blades of a fan or propeller.

- **Quadrupole Source**:

- A quadrupole source consists of two dipoles in close proximity, arranged such that their radiation patterns interact.
- It produces a more complex sound field with multiple lobes of radiation and is typically associated with fluctuating shear stresses and turbulent flows.
- Quadrupole sources are significant in high-speed aerodynamic flows where turbulence is prominent.
- Example: The noise generated by turbulent flow around an aircraft or a jet engine.

The figures below show the noise level generated for a corrected flow of 2.1 kg/s and for a rotation speed of 28541 rpm as a function of the clearance LE=TE=0 , at clearance LE=0,684,TE=0,358 and for the optimal clearance of LE=TE=0.24m.

5.8.1. Monopole Source:

For clearance (LE=TE=0,24)

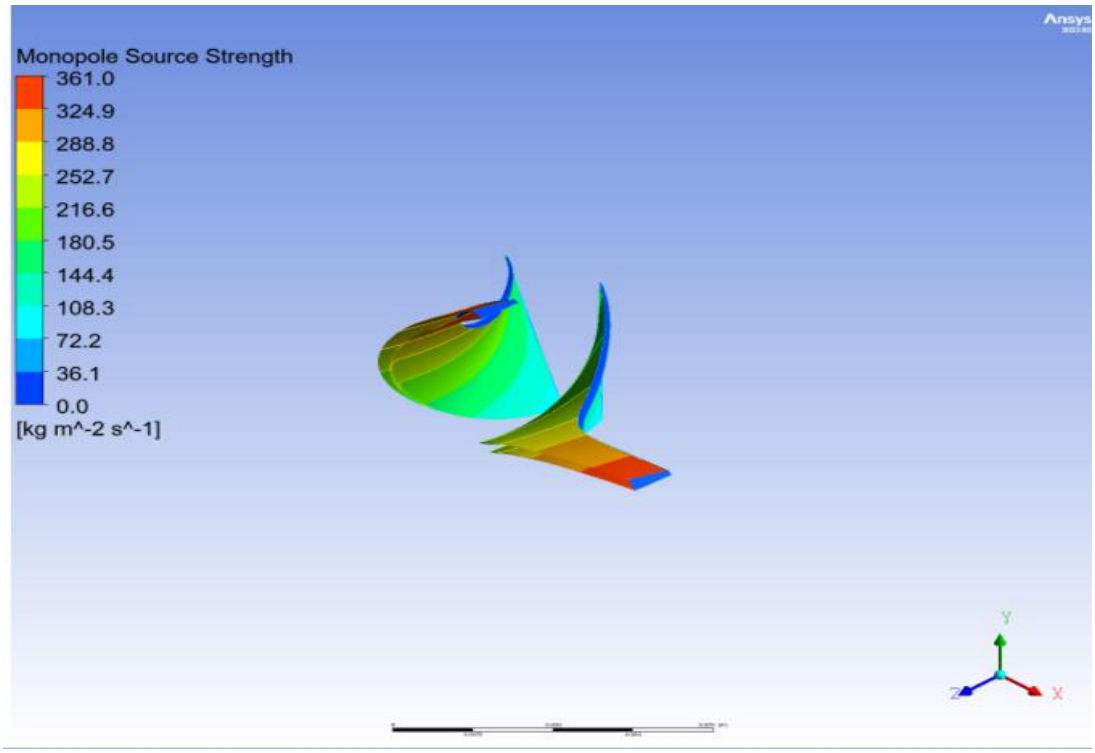

Figure 5.35: Monopole source contour for the clearance LE=TE=0.24

For clearance (LE=TE=0)

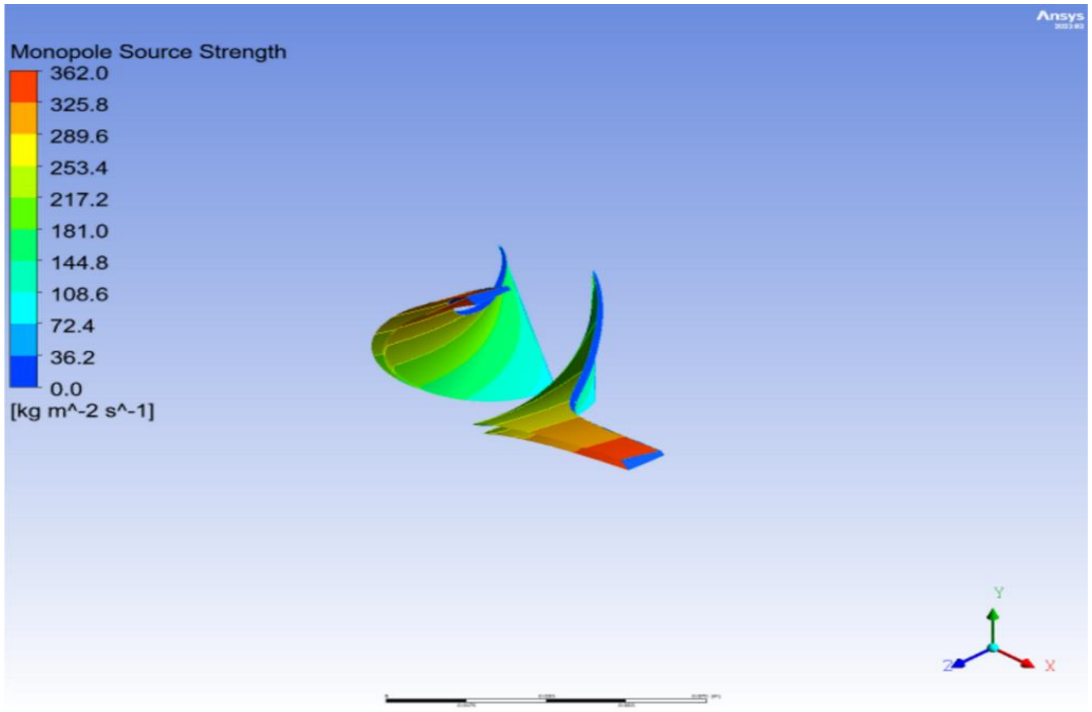

Figure 5.36: Monopoly source contour for the clearance LE=TE=0

For clearance (LE=0,684 ,TE=0,358)

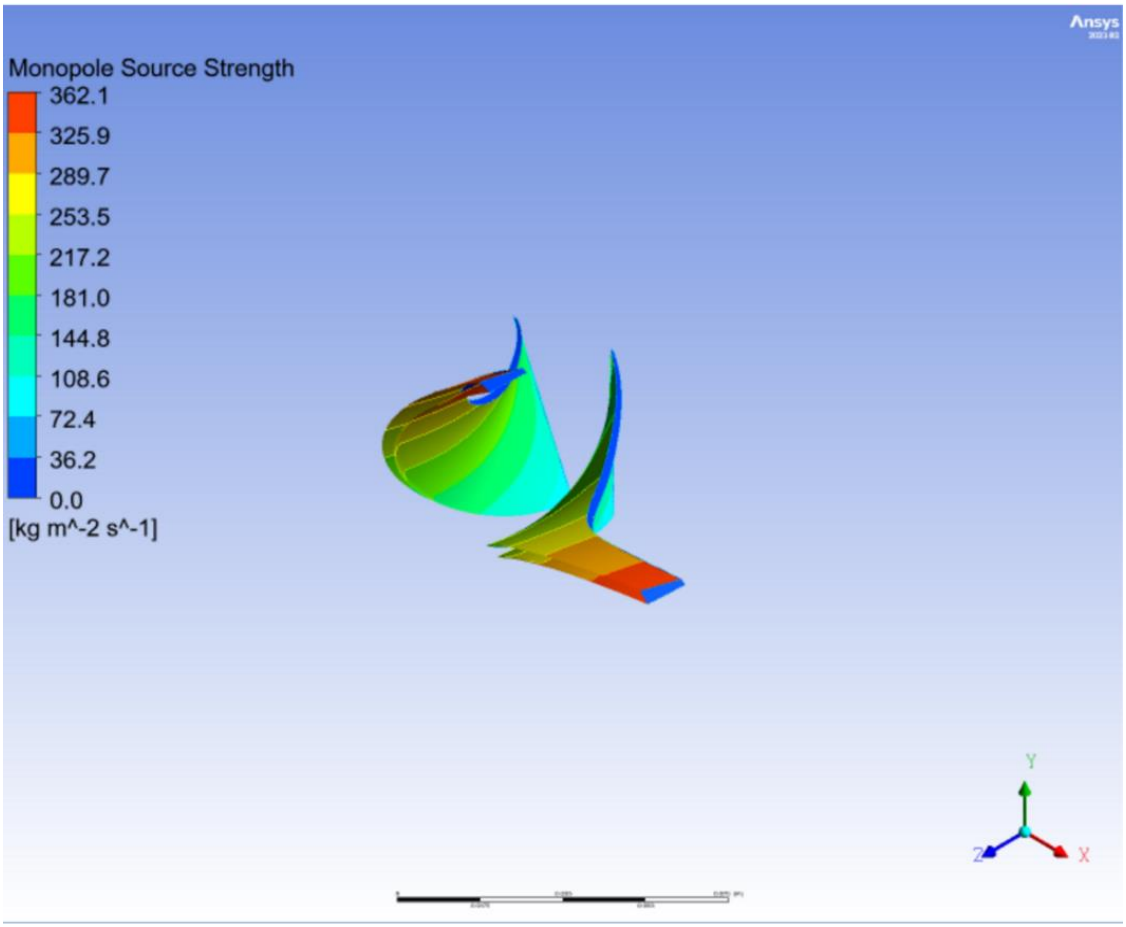

Figure 5.37: Monopoly source contour for the clearance LE=0,684, TE=0,358

The noise from the monopolar source reaches maximum values at the end of the blade, at 361 Kg/m²s , 362 Kg/m²s and 362.1 Kg/m²s for clearances of TE=LE=0.24 , LE=TE=0 and (LE=0,684 TE=0,358) respectively.

5.8.2. - Dipole Source:

For clearance (LE=TE=0,24)

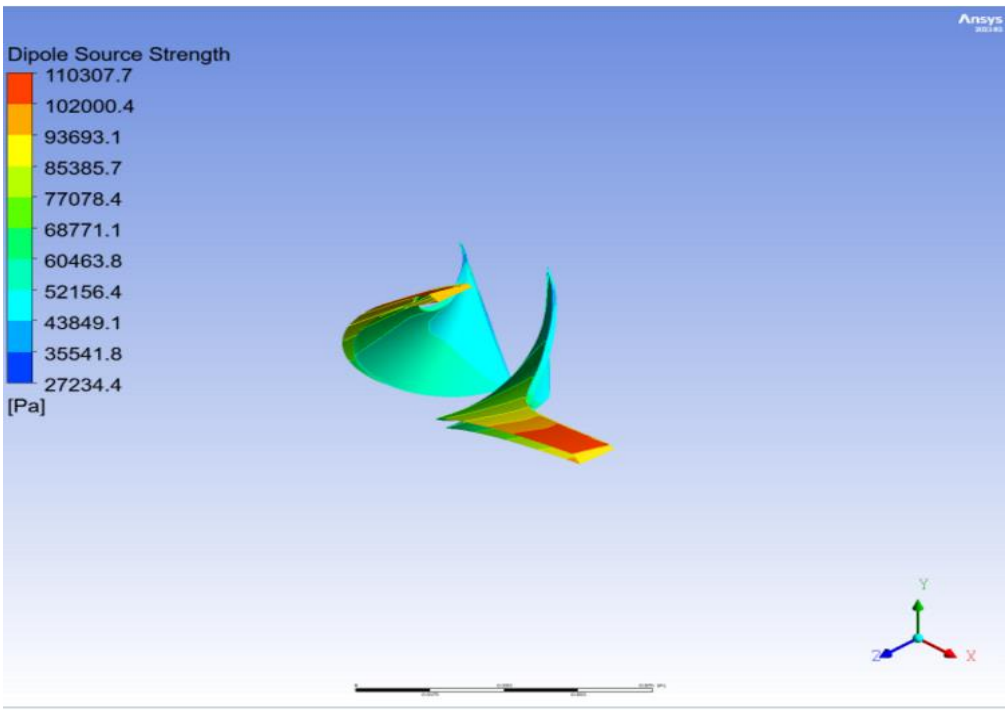

Figure 5.38: Dipole Source contour for the clearance LE=TE=0.24

For clearance (LE=TE=0)

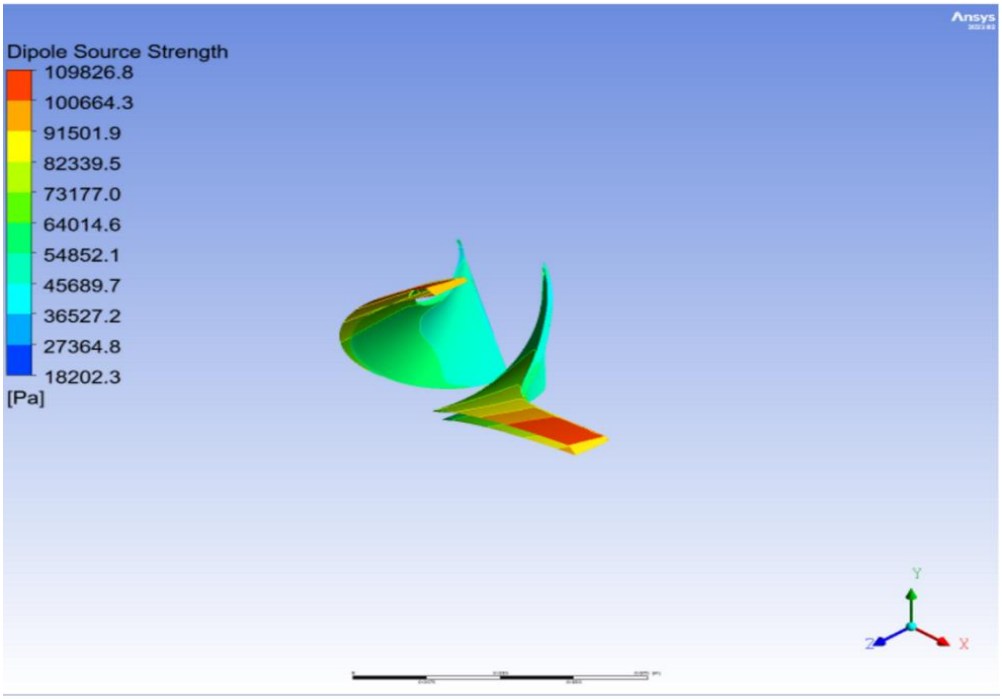

Figure 5.39: Dipole Source contour for the clearance LE=TE=0.24

For clearance (LE=0,684, TE=0,358)

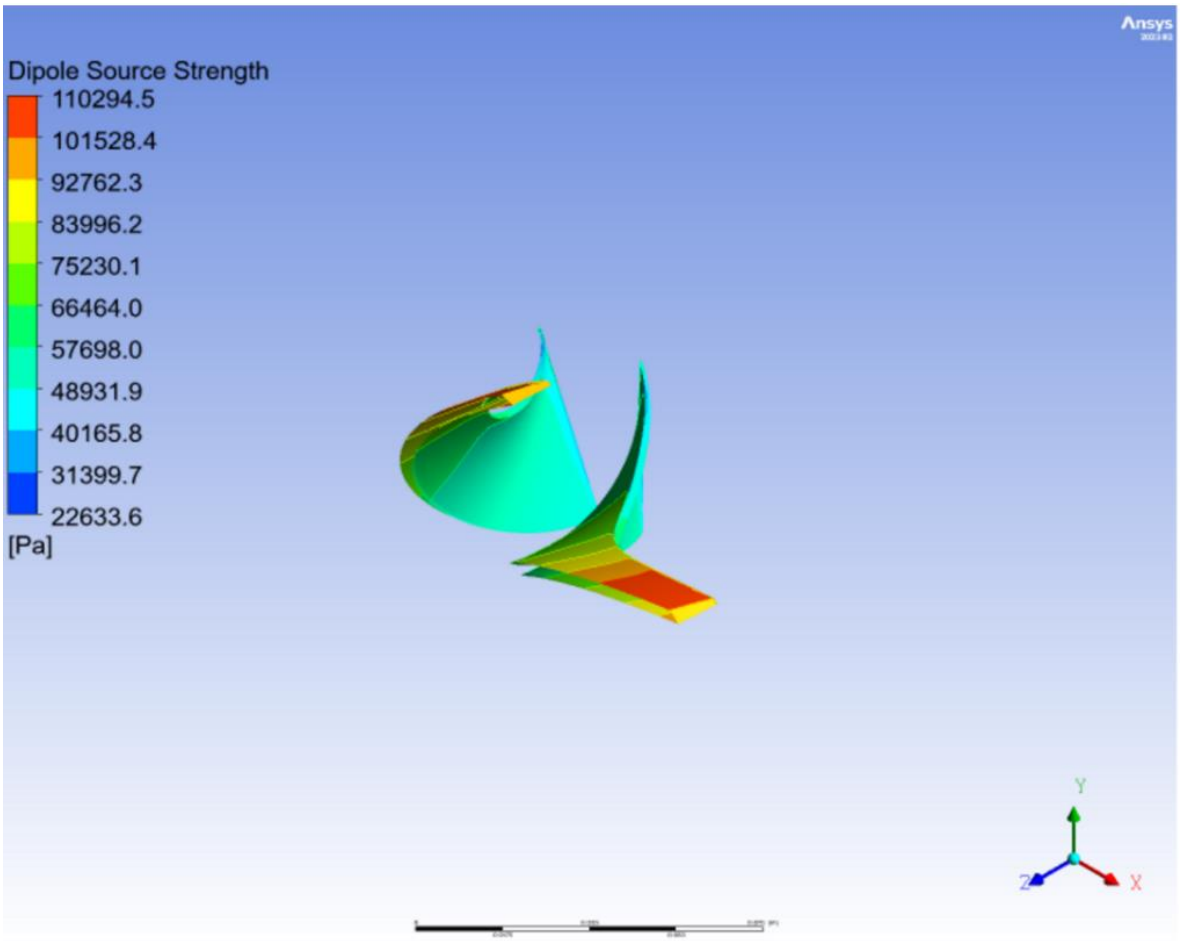

Figure 5.40: Dipole Source contour for the clearance LE=0,684, TE=0,358

The noise from the Dipole Source reaches maximum values at the end of the blade, at 110.307 KPa, 109.826 KPa and 110.294 KPa for clearances of TE=LE=0.24, LE=TE=0 and (LE=0,684 TE=0,358) respectively**.**

5.8.3. Quadrupole Source:

Table 5-6: the intensity of the Quadrupole source of the clearance TE=LE=0.24

	Quadrupole Source Strength	
Minimum	0.0	[Pa]
Maximum	55147.7	[Pa]
Average	12370.1	[Pa]

Table 5-7: the intensity of the Quadrupole source of the clearance TE=LE=0

	Quadrupole Source Strength	
Minimum	0.0	[Pa]
Maximum	39832.8	[Pa]
Average	10224.6	[Pa]

Table 5-8: the intensity of the Quadrupole source of the clearance (LE=0,684 TE=0,358)

	Quadrupole Source Strength	
Minimum	0.0	[Pa]
Maximum	56995.1	[Pa]
Average	12281.3	[Pa]

We can see that the intensity of the quadrupole source increases as the tip clearance increases. We find that the highest peak value of the quadrupole source intensity corresponds to the clearance of (LE=0,684 TE=0,358).

5.8.4. Sound power generated

➤ Sound pressure level:

For clearance LE=TE=0.24: 116.31dB

For clearance (LE=0,684, TE=0,358): 116.4 dB

➤ Sound power level:

For clearance LE=TE=0.24: 127.5574dB

For clearance (LE=0,684, TE=0,358) : 127.7 dB

With regard to the acoustic power levels measured and displayed in decibels above, it is clear that the greater the clearance between the blade and the shroud, the more powerful the noise generated. This is because the greater the clearance, the greater the secondary flow, thus generating more noise.

GENERAL CONCLUSION

The numerical simulation of the compressor stage has provided valuable insights into the airflow within the compressor, particularly highlighting the secondary flows that significantly reduce turbomachinery efficiency. Understanding these phenomena better allows for the design of more efficient machines.

The analysis was conducted using numerical modeling to simulate a three-dimensional, compressible, viscous, and turbulent steady-state flow in the impeller of the centrifugal compressor using the k-ω SST model. This was achieved with the ANSYS CFX 23 calculation code, under various operating conditions with different blade-to-shroud clearances, followed by optimization.

Numerical optimization tools facilitate the resolution of complex, multi-objective problems more quickly and efficiently through multi-criteria optimization methods and algorithms. The blade-to-shroud clearance, in particular, has a significant impact on compressor performance. Large relative end clearances can create an area of low momentum at the shroud, leading to a highly swirling bypass flow and increased losses. As the clearance increases, these losses become more pronounced.

We found the clearance of the party to be the best value is LE=TE= 0.24.

Reference

[1] Carsten WeiB, Daniel R.Grates, Hans Thermann, Reinhard Niehis. "Numerical Investigation of The Influence of The Tip Clearance on Wake Formation Inside A Radial Impeller", *International Communications in Heat and Mass Transfer, Vol. 71*. (2003), 164-171

[2] Yohan Jung, Minsuk Choi, Seonghwan Oh, and Jehyun Baek.“*Effects of a Non uniform Tip Clearance Profile on the Performance and Flow Field in a Centrifugal Compressor”. International Journal of Rotating Machinery*. (2012)

[3] Matteo Bardelli, Carlo Cravero, Martino Marini, Davide Marsano and Omar Milingi. "*Numerical investigation of impeller-vaned diffuser interaction in a centrifugal compressor”, applied sciences, Vol. 9.* (2019).

[4] Xinzi Tang, Nengwei Gu, Wenbin Wang, Zhe Wang and Ruitao Peng, *“Aerodynamic robustness optimization and design exploration of centrifugal compressor impeller under uncertainties”, International Communications in Heat and Mass Transfer, Vol. 180.* (2021)

[5] Xiaojian Li, Zhengxian Liu, Ming Zhao, Yijia Zhao, Ying He, "*Stability improvement without efficiency penalty of a transonic centrifugal compressor by casing treatment and impeller/diffuser coupling optimization”. Aerospace Science and Technology,Vol, 127,* (2022)

[6] Lianchao Xu, Zhengxian Liu, Xiaojian Li , Ming Zhao, Yijia Zhao, Tao Zhou."*Dynamic mode characteristics of flow instabilities in a centrifugal compressor impeller”. Aerospace Science and Technology. Vol 142.* (2023)

[7] ERIAN A. BASKHARONE, *“principles of turbomachinery in air-breathing engines”.* (2006)

[8] Seppo A. Korpela, *“ principles of turbomachinery”.* (2020)

[9] Ernesto Benini, *“fluid dynamics optimisation of a centrifugal compressor through design of experiments and cfd analysis”* magester memoir, university degli studi di padova. (2014).

[10] Herbert Harrison, *“development and validation of a new method to model slip and work input for centrifugal compressors the purdue university graduate school statement of committee approval”.* (2020)

[11] ANSYS Inc. Ansys cfx-solver theory guide, (2023).

[12] Aimé parois, "*Suralimentation des moteurs de véhiucules par turbocomresseur"Ed.Technique de l'ingénieur, traité de génie mécanique,* (1999).